

The Pennsylvania State University
The Graduate School
College of Earth and Mineral Sciences

**Toward the Repair of Components via Additive
Manufacturing: Process-Structure-Property
Relationships in Single Beads and Patches**

A Thesis in
Materials Science and Engineering

by
Nathan A. Kistler

© 2016 Nathan A. Kistler

Submitted in Partial Fulfillment
of the Requirements
for the Degree of

Master of Science

August 2016

The thesis of Nathan A. Kistler was reviewed and approved* by the following:

Allison M. Beese
McFarlane Assistant Professor of Materials Science and Engineering
Thesis Advisor

Edward W. Reutzel
Adjunct Professor of Engineering Science and Mechanics

R. Allen Kimel
Assistant Professor of Materials Science and Engineering

Abdalla R. Nassar
Research Associate, Pennsylvania State University Applied Research Lab

Susan B. Sinnott
Professor of Materials Science and Engineering
Head of the Department of Materials Science and Engineering

*Signatures are on file in the Graduate School.

Abstract

This thesis aims to generate an increased understanding of the directed energy deposition of two different materials: Inconel[®] 718 and Ti-6Al-4V. In order to complete a successful build using directed energy deposition, one must first completely understand the microstructure, mechanical properties, and dimensions of a single bead. Therefore, exhaustive studies were completed on Ti-6Al-4V and Inconel[®] 718 bead-on-plate deposits to study the impact processing parameters (i.e., laser power, processing speed, and working distance) had on the micro and macrostructure, microhardness in the deposit and underlying substrate, and the bead geometry (i.e., width, height, and angle of repose). The geometry of the Ti-6Al-4V single beads were used to complete Ti-6Al-4V patches to understand the effect different repair conditions had on the microstructure, microhardness, and porosity. Lastly, single bead-on-plate measurements were compared to full builds to elucidate the affect adjacently deposited beads had on the microstructure and microhardness.

Table of Contents

List of Figures	vi
List of Tables	x
Acknowledgments.....	xi
Chapter 1: Introduction.....	1
1.1 Additive Manufacturing	1
1.1.1 Optomec LENS® Process.....	3
1.1.2 Processing Parameters	6
1.2 Inconel® 718.....	9
1.2.1 Background	9
1.2.2 Mechanical and Microstructural Properties	13
1.2.2.1 Conventional Properties	13
1.2.2.2 AM Properties.....	15
1.3 Ti-6Al-4V.....	17
1.3.1 Background	17
1.3.2 Mechanical and Microstructural Properties	21
1.3.2.1 Conventional Properties	21
1.3.2.2 AM Properties.....	23
Chapter 2: Single Bead Experiments: Inconel® 718.....	25
2.1 Introduction	25
2.2 Coupled Parameters.....	27
2.3 Experimental	29
2.4 Results and Discussion.....	34
2.4.1 Effect of Processing Parameters on Fusion Zone Morphology	34
2.4.2 Effect of Processing Parameters on Bead Width and Fusion Zone Area ...	41
2.4.3 Effect of Processing Parameters on Microhardness.....	46
2.5 Summary and Conclusions.....	51
2.6 Acknowledgments.....	52
Chapter 3: Single Bead Experiments: Ti-6Al-4V	54
3.1 Introduction	54
3.2 Experimental	58
3.3 Results and Discussion.....	61
3.3.1 Internal Bead Characterization (Fusion Zone, Heat Affected Zone and Microhardness)	61
3.3.2 External Bead Characterization (Width, Height, and Angle of Repose)	69
3.4 Summary and Conclusions.....	73
3.5 Acknowledgments	74
Chapter 4: Ti-6Al-4V Patch Experiments	75
4.1 Introduction	75
4.2 Experimental	78
4.3 Results and Discussion.....	84
4.3.1 Microstructure and Heat Affected Zone	84
4.3.2 Porosity	88
4.3.3 Hardness.....	92
4.4 Summary and Conclusions.....	100

4.5 Acknowledgements	102
Chapter 5: Conclusions and Future Work	103
References	106

List of Figures

Figure 1.1. Optomec LENS® MR-7 DED Machine.....	4
Figure 1.2. Schematic of Optomec LENS® MR-7 processing head.	4
Figure 1.3. Gamma prime unit cell.	11
Figure 1.4. Gamma double prime unit cell.	12
Figure 1.5. Time temperature transformation diagram showing precipitation kinetics in IN718. Figure adapted from [21].	13
Figure 1.6. Percentage of titanium alloys used in industry. Data from [32].	18
Figure 1.7. Unit cells of primary two phases in Ti-6Al-4V. (A) HCP, α phase and (B) BCC, β phase.	19
Figure 1.8. Schematic of Ti-6Al and V binary phase diagram.	20
Figure 2.1. Schematic of bead-on-plate DED process with key features identified (not to scale).	30
Figure 2.2. Schematic of beam path and parameter variation for laser cladding in the present study.	32
Figure 2.3. Schematic showing powder flow and beam diameter change with increasing working distance (not to scale). Processing at (A) above powder focus (B) at powder focus (C) below powder focus.	33
Figure 2.4. Micrographs of deposited beads on substrate with varying processing speed and initial substrate temperature, but constant laser power of 350 W and working distance of 9.3 mm. Processing speed is: 8.5 mm/s in (A) and (E), 10.6 mm/s in (B) and (F), 12.7 mm/s in (C) and (G) and 16.9 mm/s in (D) and (H). (A)-(D) substrates are initially room temperature. (E)-(H) substrates are preheated to 350°C. All images are at the same magnification, with the scale bar in (A) equal to 100 μ m. The number in each figure corresponds to the normalized enthalpy (H^*) for each micrograph.	35
Figure 2.5. Micrographs of deposited beads on substrate with varying laser power and initial substrate temperature, but with laser scanning speed constant at 10.6 mm/s and working distance of 9.3 mm. Laser power is: 250 W in (A) and (E), 300 W in (B) and (F), 350 W in (C) and (G) and 400 W in (D) and (H). (A)-(D) substrates are initially room temperature. (E)-(H) substrates are preheated to 350°C. All images are at the same magnification, with the scale bar in (A) equal to 100 μ m. The number in each figure corresponds to the normalized enthalpy (H^*) for each micrograph.	36
Figure 2.6. Micrographs of deposited beads on substrate with varying beam diameter and initial substrate temperature, but constant laser power of 350 W and processing speed	

of 10.6 mm/s. Working distance is: 7.9 mm in (A) and (E), 9.3 mm in (B) and (F), 10.7 mm in (C) and (G) and 12.1 mm in (D) and (H). (A)-(D) substrates are initially room temperature. (E)-(H) substrates are preheated to 350°C. All images are at the same magnification, with the scale bar in (A) equal to 100 μm . The number in each figure corresponds to the normalized enthalpy (H^*) for each micrograph. 37

Figure 2.7. Schematic of surface tension and temperature curve for IN718. The red shaded region denotes a nominal melt pool temperature distribution for changing laser power and processing speed. (A) Low power and high speed, (B) Medium power and medium speed and (C) High power and low speed. Arrows in the melt pool schematics denote fluid flow direction. 40

Figure 2.8. Microstructure images of dendrites at (A) Laser Power: 350 W, Processing Speed: 8.5 mm/s, Working Distance: 9.3 mm and Initial Substrate Temperature: 25°C (B) Laser Power: 250 W, Processing Speed: 10.6 mm/s, Working Distance: 9.3 mm and Initial Substrate Temperature: 25°C (C) Laser Power: 350 W, Processing Speed: 8.5 mm/s, Working Distance: 9.3 mm and Initial Substrate Temperature: 350°C (D) Laser Power: 250 W, Processing Speed: 10.6 mm/s, Working Distance: 9.3 mm and Initial Substrate Temperature: 350°C. 41

Figure 2.9. Plot of bead width with changing normalized enthalpy. Power, speed and working distance are varied and represented by squares, circles, and triangles respectively. Solid markers are preheated while hollow markers are room temperature. 42

Figure 2.10. Plot of fusion zone area with normalized enthalpy. Power, speed and working distance are varied and represented by squares, circles, and triangles respectively. Solid markers are preheated while hollow markers are room temperature. Solid lines denote line of best fit for laser power and speed data. Dashed lines denote line of best fit for working distance variable data. 45

Figure 2.11. Hardness traverses along cross-sections of room temperature substrate deposits at different normalized enthalpies. Approximate fusion zone (FZ), heat affected zone (HAZ), and base metal regions are denoted. 47

Figure 2.12. Hardness traverses along cross-sections of preheated substrate deposits at different normalized enthalpies. Approximate fusion zone (FZ), heat affected zone (HAZ), and base metal regions are denoted. 48

Figure 2.13. Hardness in the fusion zone as a function of cooling rate. 50

Figure 2.14. Back scattered electron SEM images of (A) High hardness, Laser Power: 350 W, Processing Speed: 16.9 mm/s, Working Distance: 9.3 mm and Initial Substrate Temperature: 25°C, and (B) Low Hardness, Laser Power: 350 W, Processing Speed: 10.6 mm/s, Working distance: 12.1 mm and Initial Substrate Temperature: 350°C. 51

Figure 3.1. Schematic of tool path and variable variation. 59

Figure 3.2. Schematic of powder fed DED process with key measurement locations labeled.	60
Figure 3.3. Overlay of key microstructural areas and measurements.	62
Figure 3.4. Optical macrographs of variable laser power cases. (A) 225 W, (B) 300 W, (C) 375 W and (D) 450 W. Processing speed held constant at 10.6 mm/s.	63
Figure 3.5. Optical macrographs of variable processing speed cases. (A) 5.3 mm/s, (B) 7.9 mm/s, (C) 10.6 mm/s and (D) 15.9 mm/s. Laser power held constant at 450 W.	64
Figure 3.6. Fusion zone propagation area as a function of linear heat input.	66
Figure 3.7. Microhardness as a function of distance from the top of the bead. Closed circles and filled squares denote power and speed variable data respectively. Lines show the metallographic measured heat affected zone from the top of the bead.	67
Figure 3.8. Profilometer and metallographic bead height as a function of linear heat input.	69
Figure 3.9. Profilometer and metallographic measured bead width as a function of linear heat input.	70
Figure 3.10. Profilometer and metallographic measured angle of repose as a function of linear heat input.	72
Figure 4.1. Schematic of heating apparatus placement in the current study.	80
Figure 4.2. Hatch patterns used in the current study.	81
Figure 4.3. (A) Raw and (B) thresholded cross-sectional image to show lack-of-fusion porosity (black spots in deposit).	83
Figure 4.4. Macrostructure of 10-layer, 0s IDT, 25°C, 2.5 mm substrate thickness, parallel hatch pattern build (Run 15).	85
Figure 4.5. Cross-section of a single bead-on-plate using the same laser power and processing speed (300 W, 10.6 mm/s) as the patch deposits with key features labeled. ..	85
Figure 4.6. Maximum $(HAZ)_{\alpha+\beta}$ depth measured from the substrate surface for all room temperature patch builds. Dashed line denote the $(HAZ)_{\alpha+\beta}$ depth of the single bead-on-plate.	86
Figure 4.7. Maximum $(HAZ)_{\alpha+\beta}$ depth measured from the substrate surface for all preheated patch builds. Dashed line denote the $(HAZ)_{\alpha+\beta}$ depth of the single bead-on-plate.	87

Figure 4.8. Overall density measurements for room temperature substrate samples in the current study. Symbol shape denotes IDT, line style denotes hatch pattern used and symbol face denotes substrate thickness.	89
Figure 4.9. Overall density measurements for preheated substrate samples in the current study. Symbol shape denotes IDT, line style denotes hatch pattern used and symbol face denotes substrate thickness.	90
Figure 4.10. Histogram relating observed porosity in 0s IDT, room temperature initial substrate temperature, 12.7 mm substrate thickness, cross hatch pattern, and 3 deposited layers (Run 11) and 0s IDT, room temperature initial substrate temperature, 12.7 mm substrate thickness, cross hatch pattern, and 10 deposited layers (Run 25).	91
Figure 4.11. Horizontal hardness traverses in 3-layer deposit, 25°C, 40s IDT, thin substrate, parallel hatch pattern (Run 2) and 3-layer deposit, 400°C, 0s IDT, thin substrate, parallel hatch pattern (Run 3).	93
Figure 4.12. Vertical hardness traverses in runs 3-layer deposit, 25°C, 40s IDT, thin substrate, thin substrate, parallel hatch pattern (Run 2), 3-layer deposit, 400°C, 0s IDT, thin substrate, parallel hatch pattern (Run 3) and 10-layer deposit, 25°C, 40s IDT, thick substrate, parallel hatch pattern (Run 20). Dashed line denotes hardness of single bead.	94
Figure 4.13. Location of hardness indents in all patch samples in the current study overlaid on 10-layer deposit, 25°C, 0s IDT, thin substrate, and parallel hatch pattern deposit (Run 15).	95
Figure 4.14. Average deposit hardness of room temperature substrate cases. Black horizontal lines denote the hardness and standard deviation of a single bead while orange horizontal lines denote the hardness and standard deviation of the substrate material. ...	98
Figure 4.15. Average deposit hardness of preheated substrate cases. Black horizontal lines denote the hardness and standard deviation of a single bead while orange horizontal lines denote the hardness and standard deviation of the substrate material.	99

List of Tables

Table 1.1. Composition of IN718 [19].	10
Table 1.2. Values of IN718 under different heat treatment conditions.	14
Table 1.3. Mechanical properties of DED and wrought IN718 specimens under different heat treatments.	17
Table 1.4. Microstructure and mechanical properties in Ti-6Al-4V relation to cooling rate from above β transus.	22
Table 2.1. Material properties used in normalized enthalpy calculation.	28
Table 2.2. Processing parameters used in these experiments.	31
Table 3.1. Chemical composition (in weight percent) of substrate and powder used in these experiments. Substrate was only characterized for O, N, and C to determine discrepancies with powder.	59
Table 4.1. Substrate and powder chemical compositions in weight percent.	80
Table 4.2. Parameter sets used in the current study.	82
Table 4.3. Statistical results of relative influence of different variables on hardness variations in the FZ of current data from a two sample T-Test where a p-value less than 0.05 shows a statistically significant influence.	95

Acknowledgments

I would like to express my gratitude to my thesis advisor, Dr. Allison Beese of Materials Science and Engineering at Penn State for helping me to accomplish this goal. Her advice on the countless drafts always pointed me in the correct direction. Without her guidance and supervision over the past three years, this would not be possible. She has given me the tools to succeed in my professional career, for which I cannot be more thankful.

I would also like to thank Dr. Abdalla Nassar, Dr. Edward Reutzel, and Dr. Allen Kimel for their valuable comments and insights throughout project.

Furthermore, I am grateful for the assistance and training of everyone at Penn State's Center for Innovative Material Processing through Direct Digital Deposition (CIMP-3D). The incredible tutelage given by everyone helped me gain a better appreciation of the intricacies of laser-material processing and examination.

Lastly, I want to express my immeasurable gratitude to my parents, sisters, and fiancée for their amazing support and encouragement no matter what aspirations I am setting my mind towards. Words cannot express how thankful I am to have such an incredible support system. Thank You.

Chapter 1: Introduction

1.1 Additive Manufacturing

Metal based additive manufacturing (AM) is an emerging technology that creates 3-dimensional parts in a layer by layer fashion using a metal powder feed stock. The process utilizes a computer automated design (CAD) file, which, after conversion to a layered STereoLithography (STL), can be inputted into an AM machine for printing. This manufacturing technique has gained attention due to its ability to create complex geometries with little to no post processing necessary [1]. This is in contrast to other subtractive machining methods that result in generation of large amounts of waste material. Therefore, use of AM can result in savings in manufacturing cost and time. Furthermore, AM is advantageous because customized individual parts can be cost-effectively printed to fit a specific application [2]. This personalization is not possible in other manufacturing methods (i.e., casting) because of the high production cost of individual tooling and parts.

Recently, AM has shown promise for repair of high-value components that may wear over time due to contact with neighboring parts [3]. Instead of scrapping the part because of the wear, AM has the ability to replace the worn material allowing the part to be entered back into service quickly. Traditional methods to create a replacement part may have lead times on the order of weeks or months; AM promises to significantly reduce lead times by producing parts and repairs on-site resulting in cost and time savings.

Metal based AM necessitates the use of high powered energy sources to completely melt the added feedstock material and a portion of the previous layer to create

a metallurgical bond free from porosity and other defects. The energy input is noteworthy because the cooling and reheating cycles create residual stresses that lead to distortion [4]. Especially in repair applications, dimensional tolerances must be maintained if the part is to be reintroduced into service.

The most popular forms of metal based AM today are powder bed fusion (PBF) and directed energy deposition (DED) where similarities between these AM categories include an inert atmosphere (i.e., argon) to avoid oxidation during fabrication, as well as, use of high power energy sources (i.e., laser or electron beam) to melt feedstock and substrate material.

PBF, also known as selective laser melting (SLM), utilizes a laser (typically ~200W) to selectively melt specified regions of preplaced powder [2]. Following the completion of one layer, a new layer of powder is scraped over the previous and the process continues. PBF uses a powder feedstock and has resolution capable of 100 μm and layer size down to 20 μm , creating an excellent surface finish. The thin size of each layer leads to significantly lower build rates relative to other metal based AM techniques. This technique has been shown to produce near-full density materials that exhibit properties approaching that of conventionally processed material [5].

DED is an AM approach that utilizes a laser or electron beam source to generate high thermal energies and build rates several times that of PBF [2]. In this process, powder or wire feedstock is added to a melt pool created by the heat source to build a single bead. Multiple beads are placed adjacent to one another to produce a layer and multiple layers are generated to build a component. This technique is of lower resolution

compared to PBF and parts must be machined after deposition if tight dimensional tolerances are required.

1.1.1 Optomec LENS[®] Process

Developing an understanding of the intricacies of the DED process termed the laser engineered net shape (LENS[®]) process, especially as applied to repair, is the focus of this thesis. A picture of the commercial Optomec LENS[®] MR-7 machine used in the studies presented here is shown in Figure 1.1. A schematic of the system's processing head is shown in Figure 1.2. A high powered neodymium-doped yttrium aluminum garnet (Nd: YAG) laser is applied perpendicular to a substrate creating a melt pool. Four copper nozzles direct argon blown powder into the melt pool, the powder melts and solidifies after mixing with remelted material from the previous layer. The substrate moves in the x-y plane specified by an inputted tool path program to produce a single bead of material. After one bead, the substrate moves in the x-y plane to produce an adjacent, joining bead. After the completion of one layer, the processing head moves in the z-direction to maintain a proper working distance with the previously deposited layer and the process continues.

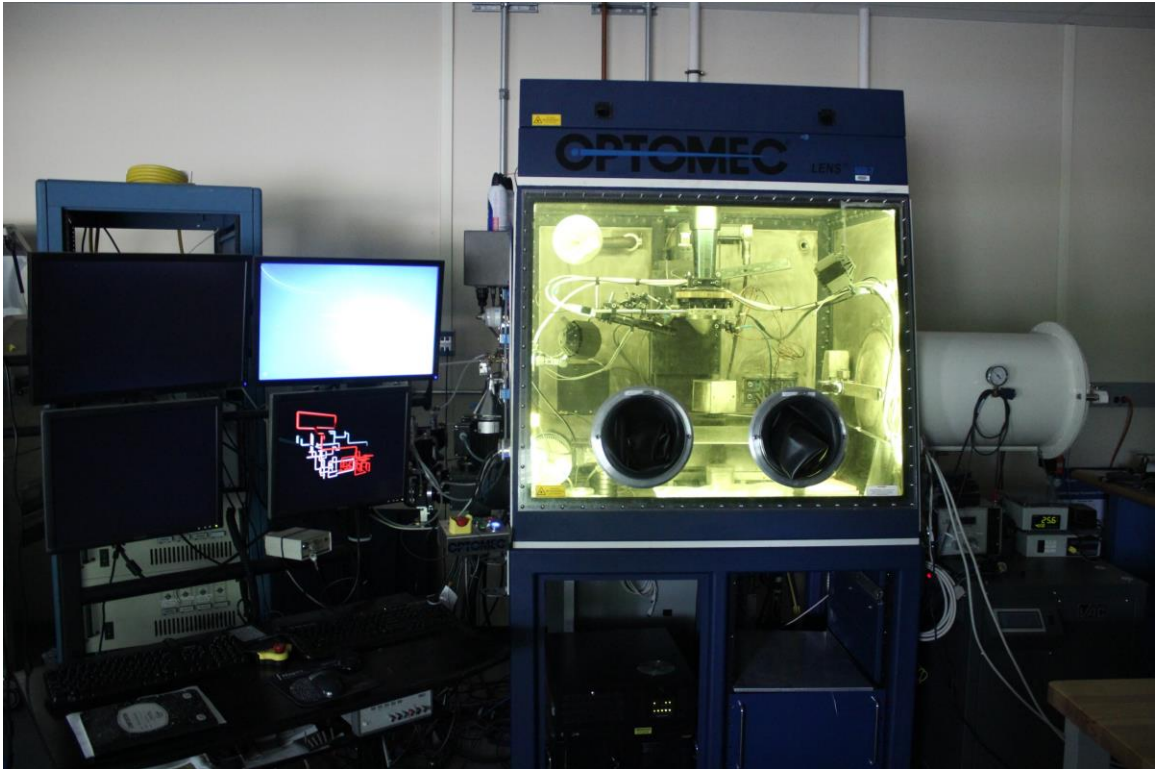


Figure 1.1. Optomec LENS® MR-7 DED Machine.

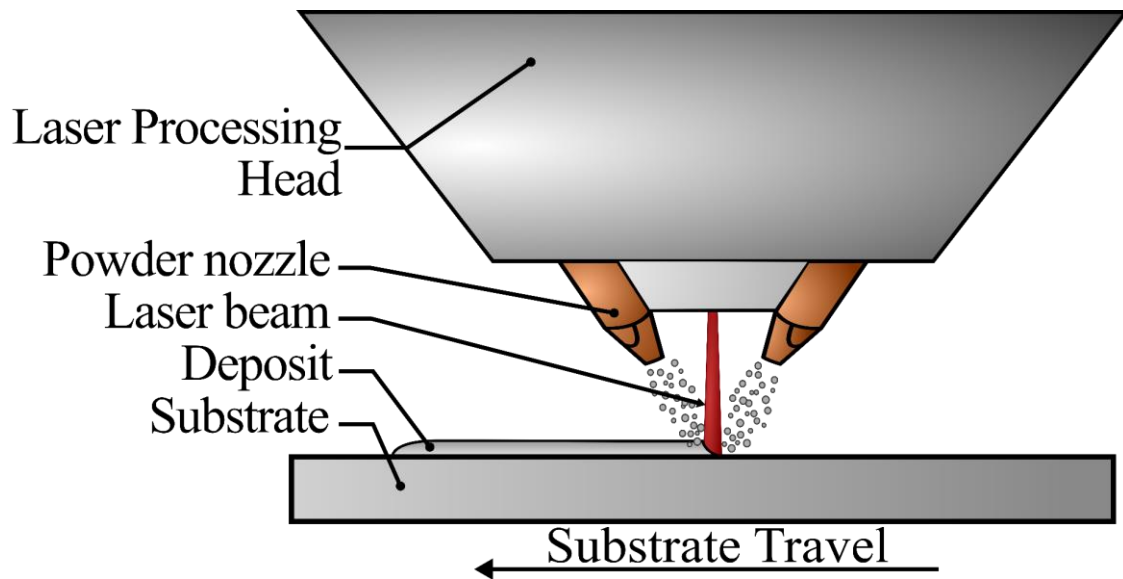


Figure 1.2. Schematic of Optomec LENS® MR-7 processing head.

The powder is typically 50-150 μm in diameter and uses a range of material systems including: aluminum alloys, multiple grades of stainless steel, tool steels,

refractory alloys, nickel-based superalloys, titanium alloys, and cobalt-chrome alloys. The substrate may be the same material as that deposited, or can be different as in the case of laser cladding applications where the purpose is to produce a layer of hardfacing material for wear resistance [6]. In-depth powder characterization systems have been shown to provide valuable data about the powder feedstock.

Conventional powder analysis techniques that are popular in powder metallurgy (i.e., apparent density, tap density, flow rate, etc.) are inadequate to characterize powder feedstock used in AM processes because of incapability to detect surface roughness, particle chemistry, and particle size distribution [7]. Emerging powder characterization technologies (e.g., Malvern Morphologi 3D ID [8]) are capable of characterizing powder morphology, size, and chemical composition through Raman spectroscopy. This is applicable to AM as consistency of the feedstock material is necessary to ensure repeatability between builds. A shortcoming of traditional powder characterization is the lack of knowledge on powder flow that is critical in AM because interactions between powder particles is a quintessential part of all AM techniques. Recent work by Strondl and co-workers [9] suggest that changes in powder rheology and particle size distribution affected the amount of porosity in the deposited material. Commercial instruments (e.g., FT4 Powder Rheometer [10]) measure flowability by reporting powder resistance to flow. This data is linked to powder particle cohesiveness through moisture content, electrostatic interactions, surface roughness, density, morphology and size.

The laser is a key component to all AM techniques as it creates the melt pool. Deviations in laser size, shape, and intensity distribution cause significant changes to the underlying additive process. Therefore, the laser beam must be sufficiently characterized

to gain an understanding of the laser-material interactions. Laser beam diagnostic equipment exist to characterize the focal position of the laser beam (e.g., Beamwatch [11]) as well as tools to measure laser beam intensity and spot size geometry (e.g., NanoScan [12]). Consistent calibration of the laser beam is necessary to be confident in the output power and process stability.

The LENS[®] process introduces a variety of methods that provide convective cooling of the molten material. First, argon is used as a means to carry the powder for delivery from the powder hopper to the melt pool. The argon flow continuously cools the deposited material throughout the process. Furthermore, a coaxial flow of gas is provided to protect the laser focusing lens from the plasma plume induced from the laser deposition process. Contaminants on the focusing lens result in alterations to the laser beam focus and spot size. The coaxially blown gas also acts as a source of convective cooling during the deposition.

Different processing conditions will change the geometry and quality of a deposition. Since the LENS[®] process depends on proper joining of adjacent beads and layers, one must understand the geometry of a single bead in order to prepare for an entire build. This mitigates unwanted lack of fusion porosity and helps to define optimal processing conditions for a full build.

1.1.2 Processing Parameters

Previous literature on DED has shown the plethora of machine parameters that can be changed and have an impact on the microstructure, and thus mechanical properties. Although there exist many combinations of variables, some have shown to

influence the deposit more than others. Examples of processing parameters that have an impact are: laser power, processing speed, hatch pattern, and powder production method.

Certainly, this is not an all-encompassing list of variable parameters in the DED AM process and one defining aspect of AM is the amount of “knobs” that can be turned in order to achieve desired properties. Many aspects of the laser beam (e.g., laser pulsing, spot size, etc.) and powder feedstock (e.g., powder particle size, size distribution, powder distribution during processing, powder chemistry, etc.) among countless others have significant effect on the deposition. The purpose of the discussion below is to introduce the parameters that have received the most amount of interest in the AM community and discuss the changes these have on microstructure and deposited material.

Parimi and co-workers [13] studied the effect of laser power on the grain morphology and dendritic structure in DED of a nickel-based superalloy. They found that the direction of dendritic growth is commensurate with the direction of heat source movement, and that dendrites did not grow between deposited layers in the lowest laser power (390 W) case. A laser power increase to 910 W resulted in a larger grain length, dendrite growth at a less acute angle (relative to lower laser power) to the previously deposited layer, and nucleation of dendrites from the previous layer. The authors showed a change in precipitates with changing laser power and that the microstructure was significantly affected by laser power.

An additional variable in the DED process is processing speed. Kobryn and co-workers [14] studied the effect processing speed had on the microstructure, porosity, and geometry of Ti-6Al-4V DED samples. In this study the authors varied processing speed from 6.8 to 10.2 mm/s while keeping laser power constant at three levels (200 W, 250 W,

and 300 W). The authors note that microstructure consistently exhibited columnar grains growing epitaxial up the build direction independent to process parameter combinations and the grain width consistently decreased with increasing processing speed which was attributed to faster cooling rates at increased processing speeds. Porosity is shown to decrease with increasing speed which the authors suggest is from less powder added to the melt pool at higher speeds. Lastly, build height decreased with increased travel speed, however, a justification for this was not presented. The authors sufficiently showed the outcomes processing speed had on the microstructure and properties in AM builds.

Hatch pattern is defined as the tool path inputted into the AM system to define the x-y direction of the heat source during deposition. As previously noted by Parimi and co-workers [13] dendrites grew toward the direction of the heat source (maximum thermal gradient). Dinda and co-workers [15] expanded on those results and showed the effect of different hatch patterns on the growth of grains in nickel-based superalloy thin-walls produced by DED. In one strategy (bidirectional) the laser traveled in one direction, then rotated 180° and deposited in the opposite direction of the previous pass; while the second strategy (unidirectional) always deposited in the same direction. The authors found a coarser microstructure in the upper regions of the deposition in bidirectional cases relative to the unidirectional strategy. Moreover, in the bidirectional strategy grains retained their crystallographic direction across layer boundaries, pointing toward nucleation of grains from the layer below, however, this phenomenon is not seen in the unidirectional strategy. Nucleation of grains was affected by the angle of grain growth in the previous layer where nucleation was easier in the bidirectional case because of a more

compatible growth mechanism allowing for preferential grain growth and coarsening of the microstructure in the top of the build. Although two hatch patterns are mentioned here, countless variations are possible and may have dramatic effects on the microstructure.

Qi and co-workers [16] attempted to optimize the DED process to create depositions with porosity less than 0.03 vol. % by changing powder type. Two types of powder were studied: plasma rotating electrode processed (PREP) and gas-atomized (GA) powder. PREP powder is typically spherical, dense, and free from satellites while GA powder is spherical, filled with gas pores, and speckled with satellites. Qi and co-workers found using PREP powder coupled with a high linear heat input (80 J/mm) minimized porosity to below 0.03 vol. %. It was suggested porosity present in the GA powder samples originated from the gas entrapment in powder particles. Therefore, in order to obtain a fully dense build after deposition, it is imperative to characterize the powder to ensure it is pore-free.

1.2 Inconel[®] 718

1.2.1 Background

Inconel[®] 718 (IN718) is a popular nickel-iron based superalloy used in critical applications that require high strength and material reliability at high temperatures. This alloy is of particular interest to the aerospace and nuclear industries due to its excellent mechanical properties, creep, and corrosion resistance at elevated temperatures [17].

The composition of IN718 is given in Table 1.1. As shown, nickel is the predominant element in this alloy; however, iron content distinguishes it from other nickel-based superalloys (e.g., Inconel[®] 625 (IN625)) [18] which contain a higher amount

of nickel but little to no iron. The addition of iron decreases the price point of IN718 relative to IN625 and affects the strengthening mechanism.

Table 1.1. Composition of IN718 [19].

Element	Min (Weight Percent)	Max (Weight Percent)
Nickel + Cobalt	50	55
Chromium	17	21
Iron	Balance	
Niobium	4.75	5.50
Molybdenum	2.80	3.30
Titanium	0.65	1.15
Aluminium	0.20	0.80

The rationale for use of nickel-based superalloys as high temperature materials lies in the connection between high-temperature deformation with the dimensionless shear strain rate. This is given by Reed [17] as

$$\bar{\dot{\gamma}} \propto \Omega^{\frac{2}{3}} \exp \left\{ -\frac{Q_v}{RT_m} \left(\frac{T_m}{T} - 1 \right) \right\} \quad (1)$$

where $\bar{\dot{\gamma}}$ is the dimensionless shear strain rate, Ω is the atomic volume, Q_v is the activation energy, $\frac{T}{T_m}$ is the temperature normalized by the melting temperature, and R is the ideal gas constant.

In order to reduce high-temperature deformation, one must minimize $\bar{\dot{\gamma}}$ by reducing $\frac{T}{T_m}$ with application of a high melting temperature material and maximizing the normalized activation energy ($\frac{Q_v}{RT_m}$) through the choice of crystal structure.

Nickel has a high melting temperature (T_m : 1455°C) that is on par with other typically used metallic elements (e.g., Ti (T_m : 1668°C) and Fe (T_m : 1538°C)) [20].

Furthermore, the matrix of IN718 is an austenitic gamma (γ) phase of face centered cubic

(FCC) crystal structure. Crystal structure is important as it is indicative of the thermal diffusivity of the material with FCC structures having high normalized activation energy and low thermal diffusivity relative to other common crystal structures (i.e., body centered cubic (BCC) and hexagonal closed packed (HCP)) [20].

The alloying elements of cobalt, iron, chromium and molybdenum tend to stabilize the γ matrix while other alloying elements (i.e., niobium, titanium, and aluminum) promote the formation of secondary phases that strengthen the matrix.

The strengthening mechanism of IN718 is a combination of the gamma prime (γ') phase ($\text{Ni}_3(\text{Al}, \text{Ti})$) and gamma double prime (γ'') phase (Ni_3Nb). γ' is a precipitate phase of cubic L1_2 structure (Figure 1.3) and while this precipitate is especially important in IN625 for strengthening, IN718 only contains a small volume fraction of γ' . The preeminent strengthening phase in IN718 is γ'' (Ni_3Nb) that forms from increased niobium content and is coherent with the γ matrix. γ'' crystallizes in the body-centered tetragonal (BCT) D0_{22} configuration and is shown schematically in Figure 1.4.

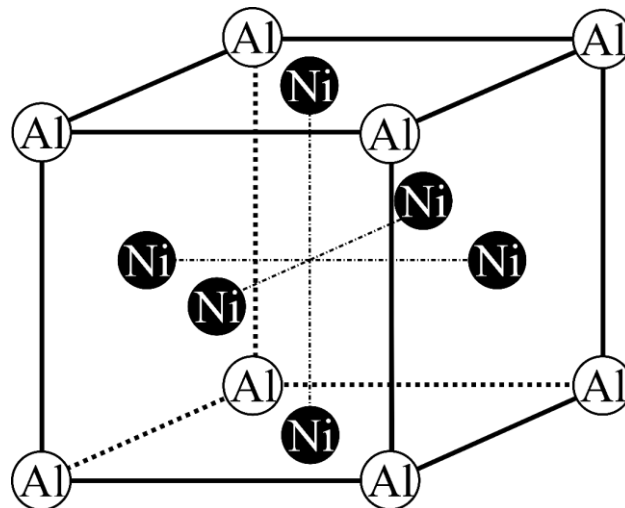


Figure 1.3. Gamma prime unit cell.

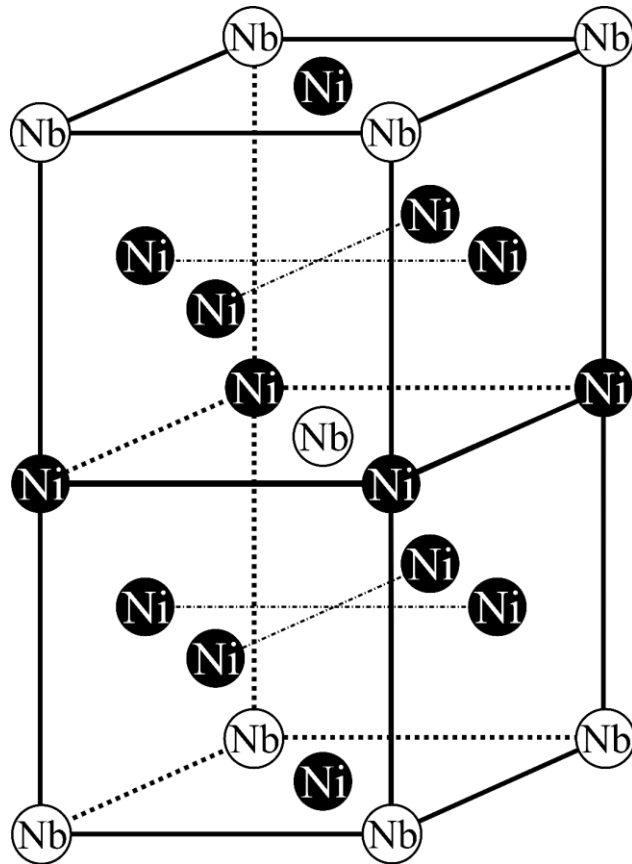


Figure 1.4. Gamma double prime unit cell.

IN718 is a precipitation hardenable alloy as stated above and necessitates heat treatment that precipitate the γ'' strengthening phase. As is typical in precipitation hardenable alloys, the heat treatment is two-fold [17]. First, a solutionizing treatment at a high temperature is used to allow all alloying elements to enter solid solution and is immediately followed by a water quench to suppress nucleation of secondary phases. Finally, an aging treatment at an intermediate temperature and over a long time period must be conducted to promote diffusion of elements and precipitation of strengthening phases.

The time temperature transformation (TTT) of IN718 is shown in Figure 1.5 where the precipitation inducing heat treatment is deciphered. The solutionizing

treatment is at temperature above 1000°C to bring elements into solid solution. This is then quenched to preserve the structure. The aging step is an 8 hour hold at 718°C followed by a furnace cool to 621°C and held for 10 hours.

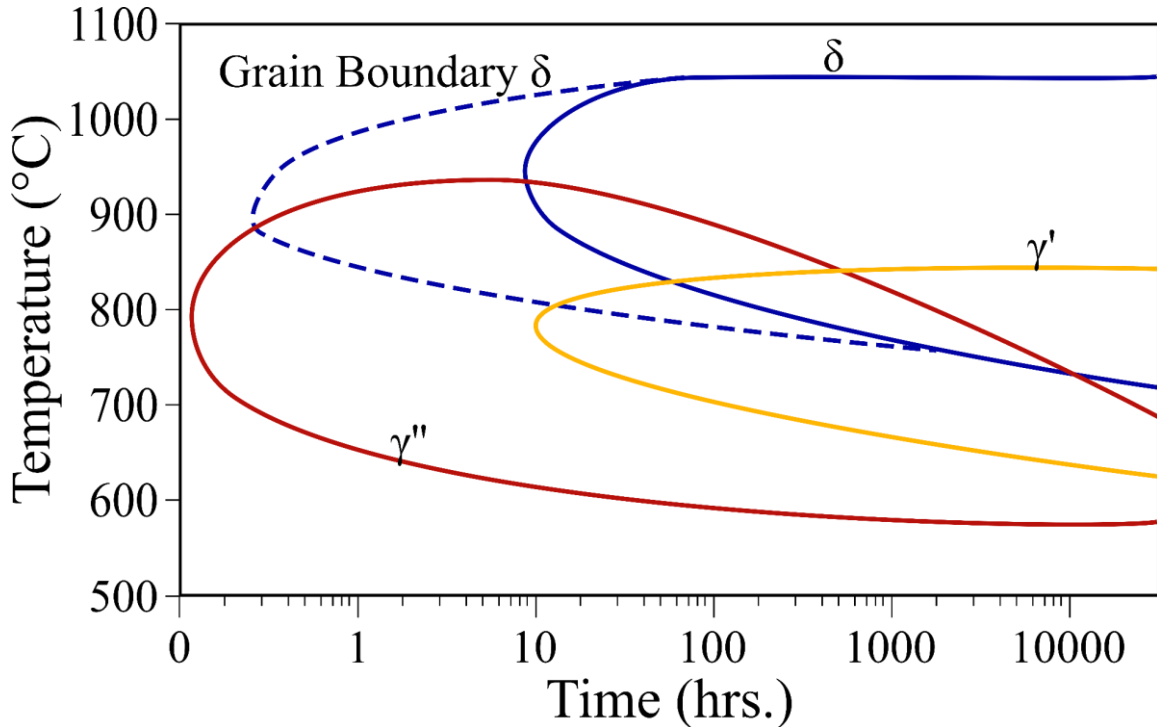


Figure 1.5. Time temperature transformation diagram showing precipitation kinetics in IN718. Figure adapted from [21].

1.2.2 Mechanical and Microstructural Properties

1.2.2.1 Conventional Properties

The microstructure and mechanical properties of IN718 are largely determined by heat treatment. This is because, as discussed IN718 develops much of its strength by precipitation of the coherent γ'' phase. The TTT diagram shown in Figure 1.5 helps to forecast the precipitates given by a particular solidification rate. This poses a unique problem towards the use of IN718 in AM because fast cooling rates will likely suppress the formation of the γ'' strengthening phase.

Ghosh and co-workers [22] reported the effect of heat treatments on the mechanical properties of IN718. The tests studied five different material conditions: forged, two solution treated and quenched samples, and two solution treated, quenched and aged samples. The results are shown in Table 1.2. Hardness values were converted from the Brinell Hardness Number (BHN) to Vickers Hardness Number (HV) using ASTM standard E140-12b [23].

Table 1.2. Values of IN718 under different heat treatment conditions.

Condition	Hardness [HV]	YS [MPa]	UTS [MPa]	Source
Solution Treated (940°C/1hr)	233	485	775	[22]
Solution Treated (1040°C/1hr)	194	407	598	
Solution Treated, Aged (940°C/1hr, 720°C/8hr)	413	826	1232	
Solution Treated, Aged (1040°C/1hr, 720°C/8hr)	405	824	1203	

Hardness, yield strength (YS), and ultimate tensile strength (UTS) decrease after solution treatment due to the lack of strengthening phases. The dissolution temperature of the γ'' is $\sim 650^\circ\text{C}$ [24]; therefore, the solution treatment temperatures dissolved secondary phases into solid solution.

Furthermore, mechanical properties change with solution treatment temperature. A lower hardness and tensile properties are obtained when solutionizing at higher temperatures. IN718 exhibits a δ phase that is useful in controlling grain size during solution treatment. However, the δ phase represents a depletion in Nb content that would otherwise be available to form the γ'' phase that is the superior strengthening phase [25].

Azadian and co-workers [25] suggest that solution treatment at 1025°C eliminates the majority of δ phase; however, additional treatment at 925°C led to significant precipitation of the δ phase. Therefore, the mechanical properties stated in Table 1.2 resulted from dissolution of the δ phase at high temperatures.

A significant increase in hardness occurred upon aging due to precipitation of the γ'' strengthening phase. The final mechanical properties after aging are independent of the initial aging temperature.

1.2.2.2 AM Properties

The fast cooling rates and complex thermal cycles in AM have been shown to have an impact on the microstructure and mechanical properties. Numerous publications show epitaxial growth of dendrites along the build direction of IN718 specimens built by DED [16], [26], electron beam melting [27], [28], and PBF [29] induced from the large thermal gradients associated with all AM processes. Furthermore, porosity had a detrimental effect on the mechanical properties in AM produced samples [30].

Zhao and co-workers [26] studied the mechanical properties of IN718 samples produced by DED relative to wrought specimens for two different powder types (GA and PREP). The AM samples were subjected to heat treatment and compared to as-deposited specimens. The as-deposited UTS and YS were far below that of wrought IN718; however, these increased to values comparable to wrought specimens upon solution treatment and aging (STA) heat treatment. The authors suggest high cooling rates in the DED process may suppress nucleation of phases in IN718, leading to a super saturated solid solution that precipitates strengthening phases when heat treated. Elongation of samples were dependent on the initial powder type with samples produced from GA powder

having significant gas entrapment porosity and lower elongation relative to PREP powder samples.

Qi and coworkers [16] studied the effect of standard heat treatments on DED produced IN718 samples and compared results to wrought IN718. The heat treatment conditions consisted of: as-deposited, STA, homogenization and STA, and direct aged (STA without solution treatment). The full results of this study are shown in Table 1.3. The authors found the samples produced by DED in the as-deposited state exhibited the lowest UTS and YS; however, upon direct aging, the UTS and YS rose to be the highest of all tested samples. Due to the tradeoff between strength and ductility, the directly aged specimen exhibited the lowest elongation. This tradeoff was mitigated through a high temperature homogenization step followed by STA where the authors suggest homogenization dissolves the brittle Laves phase back into solid solution allowing for better ductility while maintaining high strength.

Table 1.3. Mechanical properties of DED and wrought IN718 specimens under different heat treatments.

	UTS [MPa]	YS [MPa]	Elongation [%]	Source
As-Deposited	904	552	16.2	[16]
STA	1221	1007	16	
Homogenization + STA	1194	949	19.9	
Direct Aged	1333	1084	8.4	
Wrought	1276	1034	12	

In a similar study by Zhong and coworkers [31] the authors studied the microstructure and tensile properties of IN718 samples produced by DED with GA powder. In this, dendrite growth was in the direction of highest thermal gradient and numerous gas entrapment porosity were found in the as-deposited sample. Following a homogenization and STA heat treatment, brittle phases were dissolved into the γ matrix and strengthening phases were precipitated from aging with porosity remaining in the sample post heat treatment. Uniaxial tension results were consistent to Qi et al. results [16] where the as-deposited condition showed the lowest UTS and YS. However, Zhong and coworkers found greater ductility in the as-deposited samples (29 %) compared to Qi and coworkers and after heat treatment, DED UTS, YS, and ductility were comparable to wrought IN718 samples.

1.3 Ti-6Al-4V

1.3.1 Background

Ti-6Al-4V is the most popular titanium alloy used today and makes up over half of all titanium products used in industry as is shown in Figure 1.6 [32]. Ti-6Al-4V is

extremely important to many different industries because of its unique properties. Specifically, Ti-6Al-4V is important to biomedical industries as the material for implants because of biocompatibility, and it is used widely in the aerospace industry because of its excellent strength to weight ratio and corrosion resistance. Furthermore, this material is used in high performance applications as a way of maintaining advanced mechanical properties without sacrificing weight.

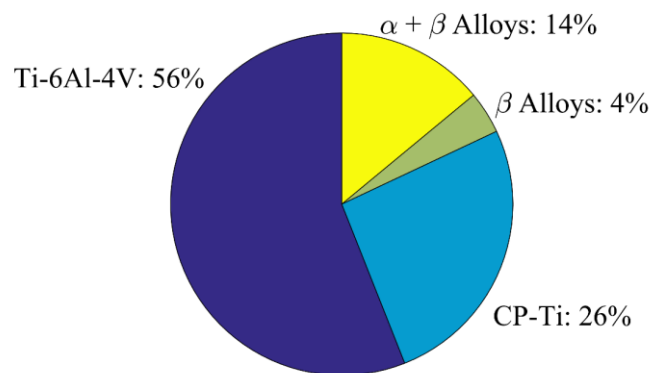


Figure 1.6. Percentage of titanium alloys used in industry. Data from [32].

Ti-6Al-4V consists of two phases at room temperature, α and β . The unit cells are shown in Figure 1.7 where α is of hexagonal closed packed (HCP) crystal structure and β in the body-centered cubic (BCC) structure. A schematic of the binary Ti-6Al and V phase diagram is shown in

Figure 1.8. At 4 weight percent vanadium and at room temperature, both α and β phases

are in equilibrium. Alloying elements in titanium may act as either α or β phase

stabilizers where aluminum performs as an α stabilizer and vanadium as a β stabilizer. A

temperature, termed the β transus (980°C for Ti-6Al-4V), signifies complete α phase

transformation to β phase. For other titanium alloys, the temperature will fluctuate

depending on concentrations of α or β phase stabilizing elements [33].

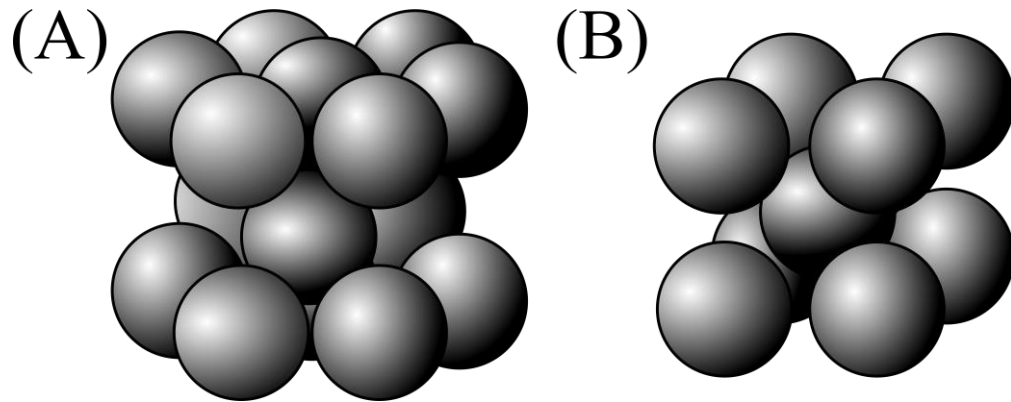


Figure 1.7. Unit cells of primary two phases in Ti-6Al-4V. (A) HCP, α phase and (B) BCC, β phase.

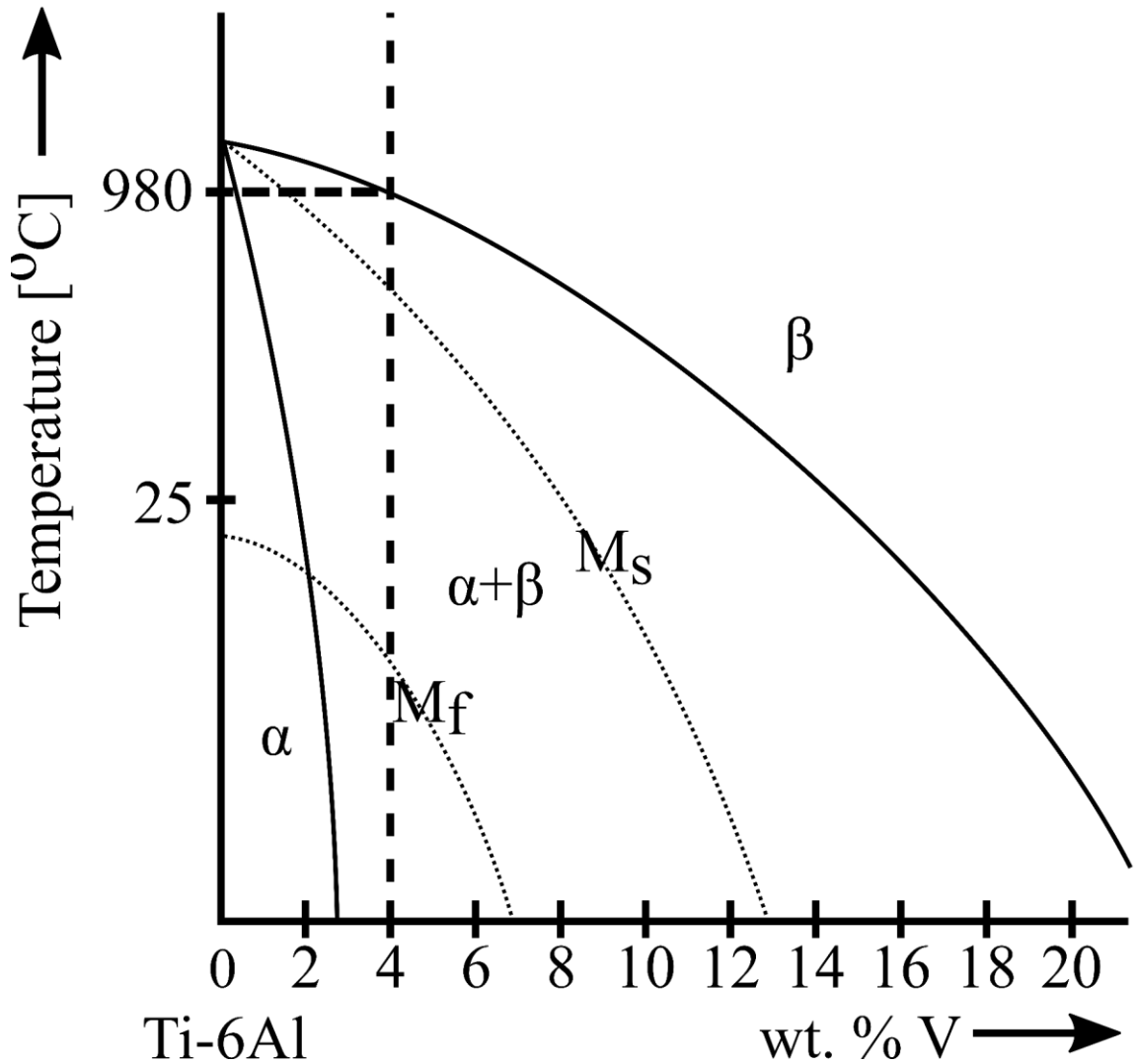


Figure 1.8. Schematic of Ti-6Al and V binary phase diagram.

Depending on cooling rate, various microstructures in Ti-6Al-4V are obtained. In Figure 1.8, the appearance of a martensite start (M_s) and martensite finish (M_f) temperatures reveal the importance of cooling rate in this alloy. Rapid cooling from the β transus results in decomposition of β phase into martensitic α' with a hexagonal structure or α'' with an orthorhombic structure [32]; however, cooling to room temperature does not decompose all β into α' or α'' because the M_f temperature for Ti-6Al-4V is below room temperature [33]. Meanwhile, slow cooling allows the

nucleation of α phase along β grain boundaries and the subsequent growth along preferred crystallographic planes. α phase continues to grow into coarse plates with retained β phase between the α plates. Upon slower cooling, coarser α laths are obtained relative to fast cooling that show a martensitic phase. Heating of martensite results in decomposition into α and β phase [32].

Ti-6Al-4V is a precipitation hardenable alloy. Material in the solution treated condition may be aged at 500°C over an extended period of time to precipitate coherent Ti_3Al particles [32]. Ti_3Al particles form in the α phase because of the abundance of aluminum and have a solvus temperature of 550°C in Ti-6Al-4V; therefore, the aging temperature must be lower than this to allow precipitation of the strengthening phase [32].

1.3.2 Mechanical and Microstructural Properties

1.3.2.1 Conventional Properties

The aforementioned microstructure influences the mechanical properties. As mentioned previously, the choice of heat treatment is crucial in determining the microstructure and mechanical properties. Depending on cooling rate from a temperature greater than the β transus temperature different microstructures are formed.

In a study by Lutjering [34] the effect of cooling rate on the resulting microstructure and mechanical properties were studied. The observed microstructure and mechanical properties were related to the cooling rate as shown in Table 1.4. The microstructure after cooling from the β transus is lamellar until a sufficiently high cooling rate is reached and martensite is the predominant microstructural feature. It was noted that as the cooling rate increases, the observed microstructure becomes finer. The finer

microstructure presents more barriers to dislocation motion thereby increasing the tensile strength of the material. However, ductility increases from the slow to intermediate cooling rate which is contrary to intuition. The authors note large amounts of continuous α phase on the grain boundaries for the behavior. As α is the more brittle phase, cracks propagate along the continuous α phase laying on the grain boundaries [34]. In the 100°C/s case, relatively less α phase lies on grain boundaries, creating a more tortuous crack path and thus, more ductility. In the 8000°C/s case, the fracture becomes less ductile and more brittle creating lower elongation.

Table 1.4. Microstructure and mechanical properties in Ti-6Al-4V relation to cooling rate from above β transus.

Cooling Rate [°C/s]	Observed Microstructure	Tensile Strength [MPa]	Elongation [%]	Source
0.02	Coarse lamellar structure; large amounts of continuous α on grain boundaries	900	6	[34]
100	Fine lamellar structure; continuous α on grain boundaries	910	8	
8000	Martensitic α' structure; no continuous α on grain boundaries	1110	4.5	

Another influence on the mechanical properties of Ti-6Al-4V are the presence of interstitial alloying elements [32]. Titanium is especially reactive to oxygen above 600°C and promote the formation of α_2 particles that increase the yield stress because of coherency within the α phase. However, α_2 particles allow for easier crack nucleation relative to α and β phases; thus causing premature failure. Furthermore, the small size of oxygen allows it to provide solid solution strengthening by lying on interstitial sites in the HCP lattice increasing yield stress by preventing dislocation movement.

1.3.2.2 *AM Properties*

As is the case in most metal based additive techniques; high cooling rates and complex thermal histories result in interesting properties in as-deposited Ti-6Al-4V. Furthermore, the directional nature in AM may result in crystallographic texture that results in an orientation dependence in mechanical properties. Recently, many research efforts have focused on the process-structure-relationships in the DED of Ti-6Al-4V.

Kelly and Kampe [35] studied the microstructure of CO₂ laser-deposited Ti-6Al-4V that utilized a powder-fed approach. The width of each layer was 3 mm and the produced sample was 18 layers high. The resulting microstructure exhibited large columnar prior β grains along the build direction of the sample and through multiple layers. Furthermore, the sample exhibited layer bands which were thought to be the result of thermal cycling which allowed for decomposition of α' or α'' into α and β [36]. α phase was present along the prior β grain boundaries and the authors note a basketweave Widmanstätten α lath structure. A quantitative measure of α lath width was performed and it was shown that α lath varies with respect to position in a layer. Just below a layer band, the average lath width was coarser (1.8 μm) relative to just above layer bands (0.9 μm). The authors suggest the gradient in alpha lath width is due to thermal effects. Microhardness in these two regions were similar (~350 HV). In the upper regions of the build, the microstructure transitioned from the basketweave structure to fine colonies of α .

In a paper by Wu and co-workers [37] the microstructure in DED Ti-6Al-4V builds and the microstructural variation with laser power, processing speed, and powder feed rate are studied independently. First, in one build, there is a change in

microstructure where α laths appear larger, higher in the build because of a decrease in heat extraction as the temperature increases from deposition of additional layers. The authors note with increasing laser power and decreasing processing speed a larger α lath is obtained. Increasing laser power and decreasing processing speed result in decreased thermal gradients leading to microstructure coarsening.

Bian and co-workers [38] compiled mechanical and microstructural data from previous DED Ti-6Al-4V literature. The authors note tensile properties that are similar or exceed that of conventionally processed material because of the rapid cooling rates that create extremely fine microstructures. While great tensile behavior is exhibited, elongation is severely crippled because of porosity induced by the AM process. Carroll and co-workers [5] found that proper elongation can be obtained when porosity-free parts are obtained.

Carroll and co-workers [5] continued to show the effect of loading direction on microstructure and mechanical properties in DED Ti-6Al-4V. The microstructure exhibited columnar prior β grains similar to that shown by Kelly and Kampe [36]. Continuous α phase was noted on the prior β grain boundaries that resulted in larger elongation when testing parallel to the build direction relative to testing perpendicular to the build direction. Continuous α phase provides a path for crack propagation. The authors suggested that a force applied perpendicular to the prior β grains (continuous α phase) provides tension along the entire α phase and promotes crack initiation. After a crack has formed, it may propagate along the prior β grain/ α phase. This crack path is easier relative to a crack that must travel intragranularly thereby resulting in decreased ductility compared to load applied long ways along the prior β grains.

Chapter 2: Single Bead Experiments: Inconel[®] 718

2.1 Introduction

In laser cladding, a layer of metallurgically-bonded material is deposited atop a component to enhance its surface properties. In most cases, a laser source is used to create a melt pool, within which powder or wire feed stock material is added to produce a clad. Laser cladding can be applied to reduce adhesive and abrasive wear, improve corrosion resistance and to repair of worn high-value components (e.g., [6]). In the aerospace industry, repair of IN718 components using laser cladding has been found to produces a better surface quality compared to plasma or arc welding [39]. Further, large thermal gradients and rapid solidification present in laser cladding result in a fine microstructure, leading to improved strength and wear resistance or repaired components [40].

When multiple clads are overlaid to create a three-dimensional component, the process is termed additive manufacturing (AM). Within AM and in the cladding of large regions, the fusion zone geometry becomes critical. An understanding of the relation between processing parameters (e.g., laser power, translation speed, powder flow rate) to melt pool geometry is necessary to reduce the probability of lack-of-fusion while maintaining an acceptable deposition rate. Lack of fusion porosity originates from inadequate melt pool penetration into the substrate or neighboring tracks, resulting in sharp voids [14] which are detrimental to mechanical properties [41].

Numerous investigation of the microstructure of DED AM IN718 exist but few focus on the fusion zone geometry. Typically, the fusion zone microstructure is found to consist of a dendritic structure with segregated intermetallic and amorphous particles

(Laves phase) [13]. The size of the Laves phase has been found to increase with laser power [13]. Ma and co-workers [42] also found that increasing energy input created non-continuous columnar grains and increased the interdendritic density of the brittle Laves phase. It may be noted that in their work, Lambarri and co-workers [43] questioned whether features appearing as the Laves phase may in fact be MC type carbides. Heat treatments dissolve the Laves phase [43], [44].

Porosity and the impact of post-processing have also been studied. Qi and coworkers [16] performed an optimization study to reduce porosity in directly deposited IN718 by changing powder type and energy input. They found that the combination of plasma rotating electrode processed (PREP) powder and high energy inputs, meaning increased laser power and decreased processing speed, reduced porosity to below 0.03 vol. %. Solution treatment of laser-deposited samples, presumably with very little porosity, followed by double aging was found to result in acceptable ultimate tensile strength but inferior elongation as compared to a forged bar [43]. The plastic behavior was attributed to twin boundaries between coatings and the base material [43]. However, ductility may have also been influenced by lack of fusion between deposited layers, as found by Blackwell [30] in his studies of the microstructure and mechanical properties before and after post-process hot isostatic pressing.

There are contradicting results in the literature on how deposit hardness is affected by processing parameters. Zhang and co-workers [45] and Lambarri and co-workers [43] reported the hardness profiles of IN718 deposits on an IN718 substrate with contrasting results. In the study by Zhang and co-workers the clad coating had a higher hardness relative to the substrate and was attributed to a high cooling rate in the clad

deposited layer. Lambarri and co-workers state the substrate is harder than the deposit because of intragranular δ particles that provide strengthening in the substrate but not the deposit.

The influence of processing parameters on the fusion zone geometry for IN718 is not-widely reported, especially at low laser powers. Zhang and co-workers [46] showed that the fusion zone geometry of a single bead deposit of IN 718 was hemispherical. However, numerical results by Lee and Farson [47] indicate that surface tension may play an important role. They found that bead geometry changed depending on the fluid flow and was shown to have an effect on the surface finish of the part; however, experimental work was not cited to validate these simulations.

Our work aims to complement the existing literature by characterizing the effects laser power, processing speed, working distance, and substrate preheat on the fusion zone geometry, microstructure, and hardness. Given the acute paucity of data available on the influence of these parameters, particularly working distance and substrate temperature, on laser cladding and AM processes, results reported here may aid experimentalists and modelers. Additionally, the effect of coupled parameters, including linear heat input and normalized enthalpy are investigated.

2.2 Coupled Parameters

In order to compare the effect of processing parameters within a single study or between studies a frequently used metric is the linear heat input (e.g., [48]), which is given as

$$\text{Linear Heat Input} = \frac{\text{Laser Power (W)}}{\text{Processing Speed } (\frac{m}{s})} \quad (2)$$

Normalized enthalpy, a dimensionless number defined by Hann and co-workers [49] that incorporates material properties and system parameters to predict laser-weld properties is given as

$$H^* = \frac{\Delta H}{h_s} = \frac{\eta P}{\rho h_s \sqrt{\pi \alpha \sigma^3} v} \quad (3)$$

where η is the surface absorptivity, P is the power, ρ is the material density, h_s is the enthalpy at the melting point, α is the thermal diffusivity, σ is half of the D4 σ beam width at the surface, and v is the processing speed. The material constants for the computation of normalized enthalpy in the present study are delineated in Table 2.1. The surface absorptivity was taken to be the same as Inconel Alloy 690, a nickel-base alloy with a similar chemical composition to IN718.

Table 2.1. Material properties used in normalized enthalpy calculation.

Material Properties				Reference
Surface Absorptivity	η	0.313	-	[50]
Density at Melting	ρ	7400	kg/m ³	[51]
Enthalpy at Melting	h_s	645000	J/kg	[51]
Thermal Diffusivity	α	5.60E-06	m ² /s	[51]
Specific Heat of Liquid	C_p	720	J/(kg·K)	[51]

As normalized enthalpy incorporates more processing parameters and material properties than linear heat input, the normalized enthalpy is used herein to elucidate links between processing, structure, and properties.

In the current investigation, a single bead of IN718 was deposited on a substrate of the same material. In laser cladding or additive manufacturing, it is necessary to deposit several subsequent beads to cover a surface; thus, understanding the integrity of a single bead is essential to establishing a basis for a full repair.

2.3 Experimental

The single beads were deposited using an Optomec, Inc. LENS[®] MR-7 directed energy deposition additive manufacturing system. A detailed schematic of the laser head configuration is given in a concurrent study on these beads [52]. The system utilized a 500 W IPG Photonics Yb-doped fiber laser. The build chamber was hermetically sealed and purged with argon, and the oxygen was maintained to less than 20 ppm during processing. The powder flow rate was 6.5 g/min. A schematic of the process with key measurement features highlighted is shown in Figure 2.1. The variable machine parameters and substrate initial temperatures are shown in Table 2.2 and Figure 2.2. A changing working distance includes variation in beam diameter and powder flow distribution. The range of working distance studied in the current investigation was selected as it goes through the powder focal point as shown in Figure 2.3. The working distance is explicitly coupled to beam diameter as shown in Table 2.2. The $D4\sigma$ width of the laser beam at the substrate was experimentally resolved with a Primes[®] FocusMonitor laser diagnostic system.

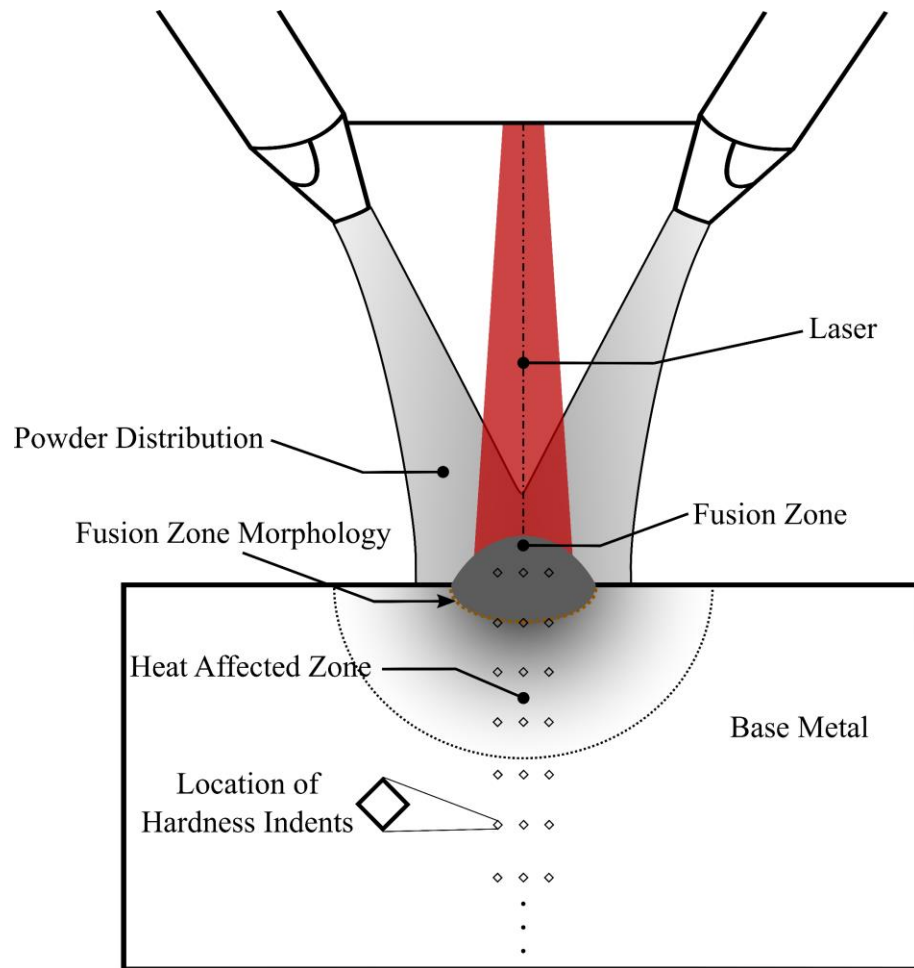


Figure 2.1. Schematic of bead-on-plate DED process with key features identified (not to scale).

Table 2.2. Processing parameters used in these experiments.

	Laser Power [W]	Processing Speed [mm/s]	Working Distance [mm]	Beam Diameter [μm]	Initial Substrate Temperature [°C]
Run 1	350	8.5→10.6→12.7→16.9	9.3	822	25
Run 2	350	8.5→10.6→12.7→16.9	9.3	822	350
Run 3	250→300→350→400	10.6	9.3	822	25
Run 4	250→300→350→400	10.6	9.3	822	350
Run 5	350	10.6	7.9→9.3→10.7→12.1	787→822→881→933	25
Run 6	350	10.6	7.9→9.3→10.7→12.1	787→822→881→933	350

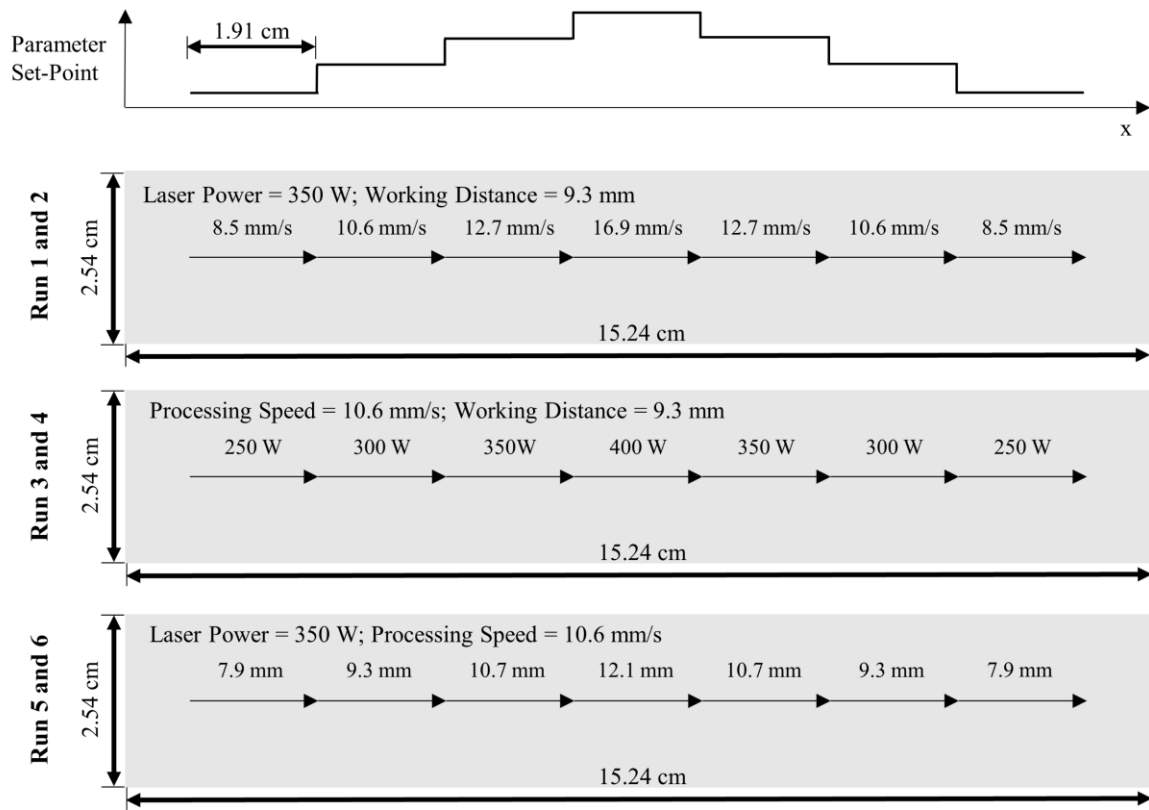


Figure 2.2. Schematic of beam path and parameter variation for laser cladding in the present study.

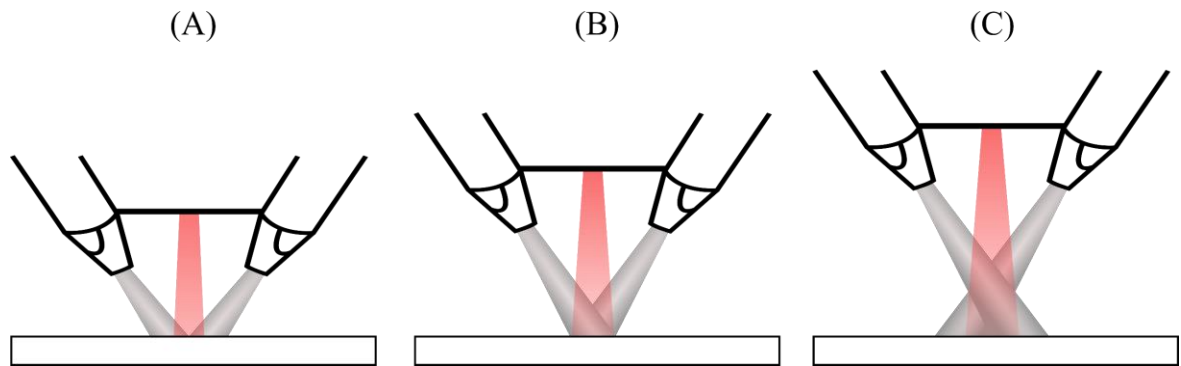


Figure 2.3. Schematic showing powder flow and beam diameter change with increasing working distance (not to scale). Processing at (A) above powder focus (B) at powder focus (C) below powder focus.

The beads were deposited onto annealed IN718 substrates 15.24 cm long, 2.54 cm wide, and 0.32 cm thick. The substrates were cleaned with acetone prior to deposition to remove oil and other contaminants. In experiments with preheating, each substrate was heated to 350°C with a strip heater (Vulcan OS-1408-250A) with the temperature measurement taken on the top of the substrate in the center of the edge parallel to the bead. Prealloyed IN718 (Carpenter Micro-Melt) was sieved using a mesh size of -120/+325, corresponding to a range of 44-125 μm powder diameter.

After deposition, the samples were cross-sectioned to view the microstructure and melt pool morphology. The samples were polished with a series of silicon carbide grinding papers and a final polish of 0.06 μm colloidal silica for 5 minutes. The samples were electrolytically etched in a 10 vol. % oxalic acid solution at 2 V for 3-5 seconds.

Microhardness measurements were performed using a Vickers hardness indenter (LECO M-400-G1) with a load of 300 g and a dwell time of 10 seconds transversely along the bead cross-section. The location of hardness measurements is schematically represented in Figure 2.1. Uncertainty in the hardness measurements were determined to be ± 5 HV.

Fusion zone measurements were performed using ImageJ image processing software.

2.4 Results and Discussion

2.4.1 Effect of Processing Parameters on Fusion Zone Morphology

Optical micrographs (Keyence VHX-2000) of each single bead track are given in Figures 2.4-2.6. Figure 2.4 shows images for variable processing speed, Figure 2.5 shows images for variable laser power, and Figure 2.6 shows images for variable working distance. Both room temperature and preheated cases are presented in Figures 2.4-2.6. In the figures, the fusion zone can be distinguished from the base metal by the contrasting microstructures. The fusion zone contains dendrites, which formed upon rapid solidification of the melt. Along the fusion zone-HAZ boundary, primary dendrites grow perpendicular to the solidification front.

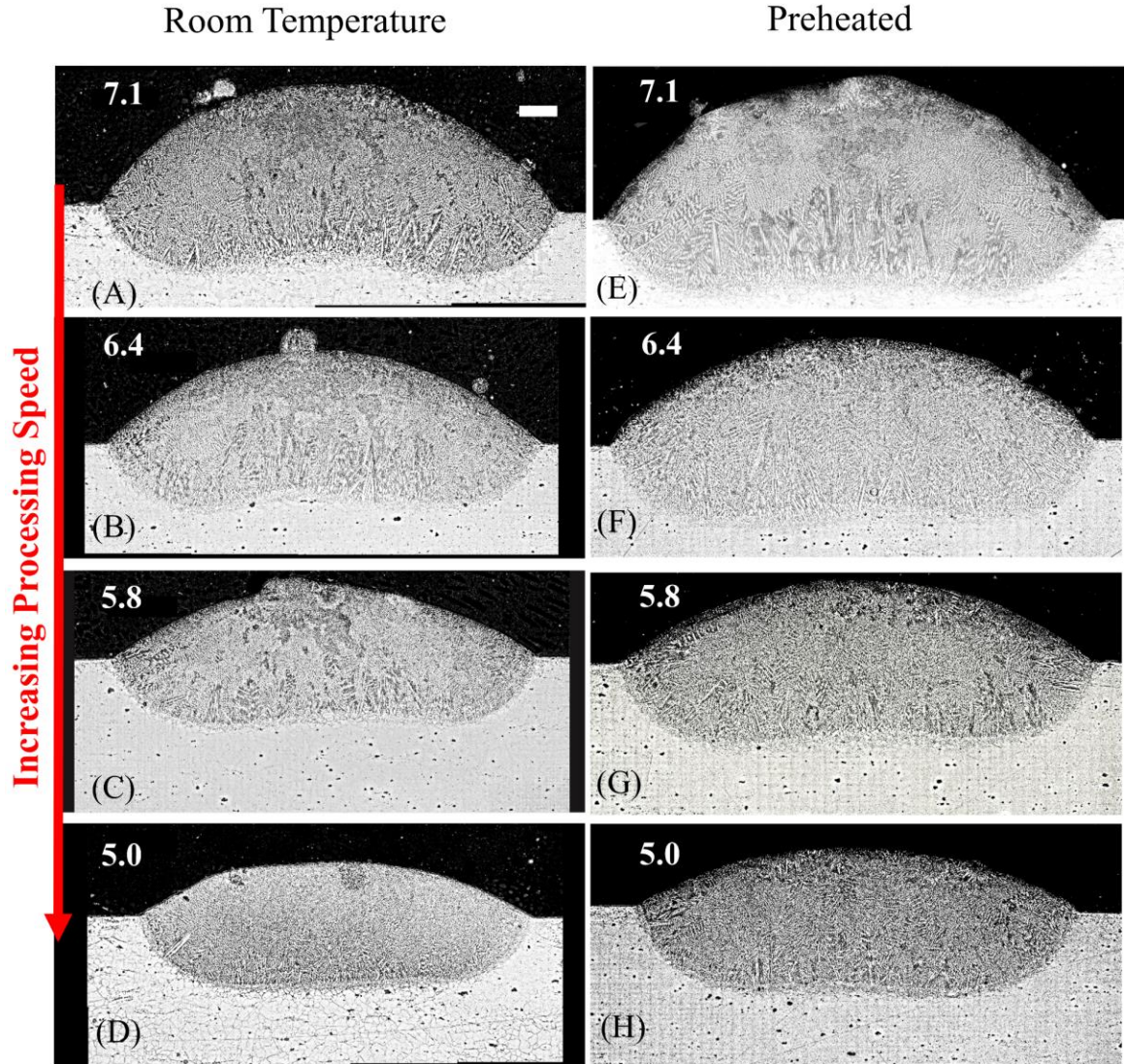


Figure 2.4. Micrographs of deposited beads on substrate with varying processing speed and initial substrate temperature, but constant laser power of 350 W and working distance of 9.3 mm. Processing speed is: 8.5 mm/s in (A) and (E), 10.6 mm/s in (B) and (F), 12.7 mm/s in (C) and (G) and 16.9 mm/s in (D) and (H). (A)-(D) substrates are initially room temperature. (E)-(H) substrates are preheated to 350°C. All images are at the same magnification, with the scale bar in (A) equal to 100 μm. The number in each figure corresponds to the normalized enthalpy (H^*) for each micrograph.

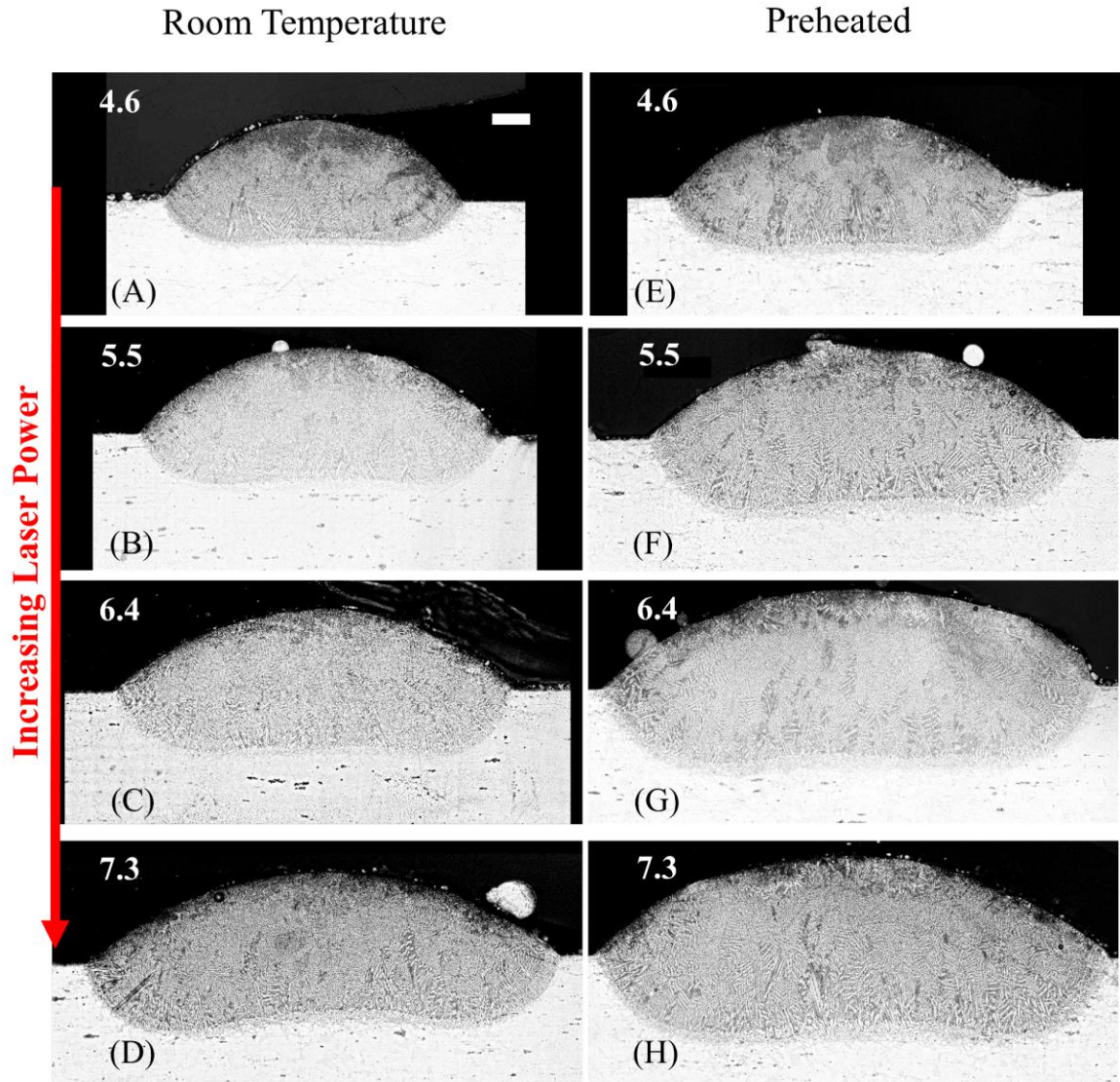


Figure 2.5. Micrographs of deposited beads on substrate with varying laser power and initial substrate temperature, but with laser scanning speed constant at 10.6 mm/s and working distance of 9.3 mm. Laser power is: 250 W in (A) and (E), 300 W in (B) and (F), 350 W in (C) and (G) and 400 W in (D) and (H). (A)-(D) substrates are initially room temperature. (E)-(H) substrates are preheated to 350°C. All images are at the same magnification, with the scale bar in (A) equal to 100 μm . The number in each figure corresponds to the normalized enthalpy (H^*) for each micrograph.

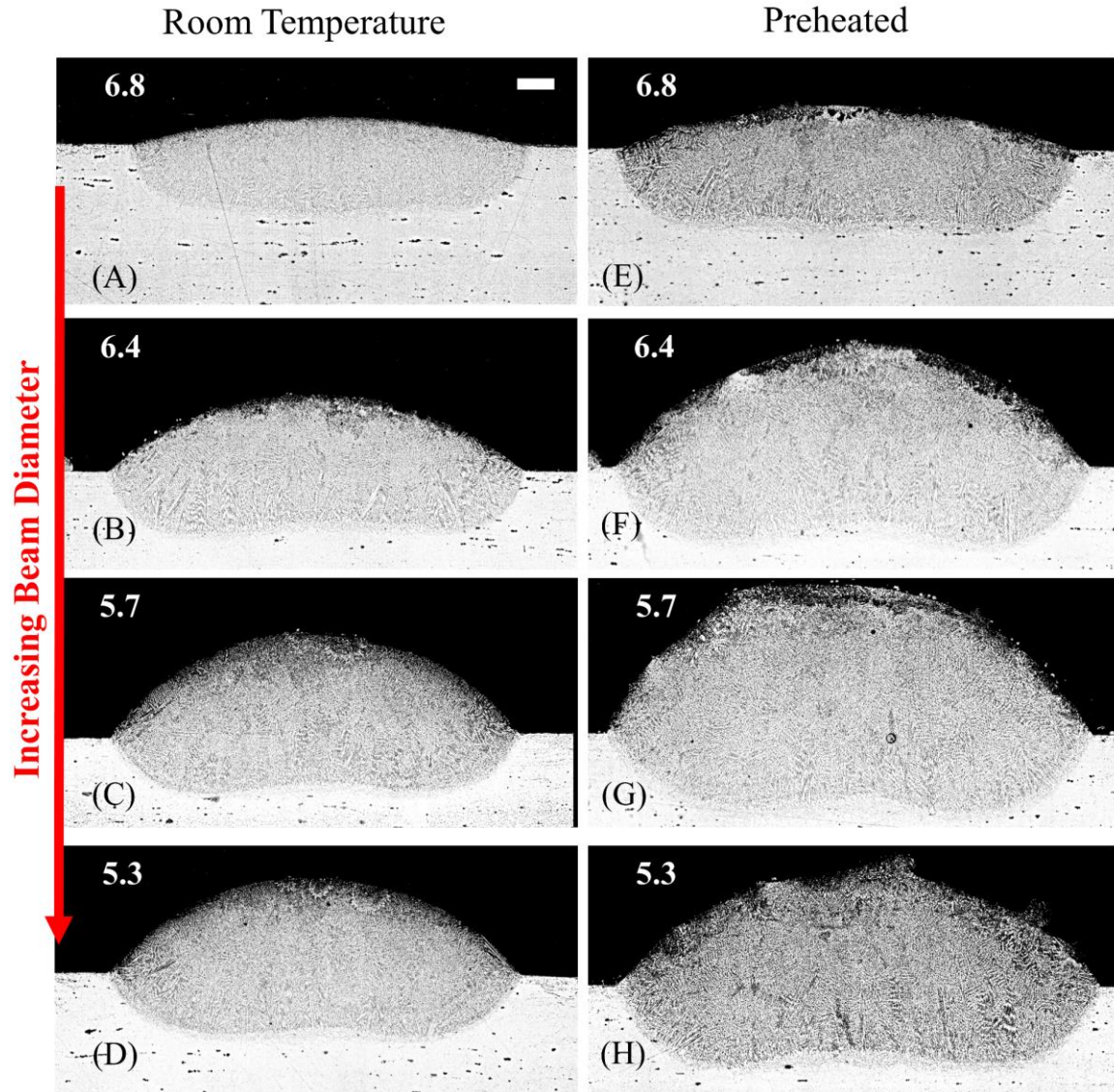


Figure 2.6. Micrographs of deposited beads on substrate with varying beam diameter and initial substrate temperature, but constant laser power of 350 W and processing speed of 10.6 mm/s. Working distance is: 7.9 mm in (A) and (E), 9.3 mm in (B) and (F), 10.7 mm in (C) and (G) and 12.1 mm in (D) and (H). (A)-(D) substrates are initially room temperature. (E)-(H) substrates are preheated to 350°C. All images are at the same magnification, with the scale bar in (A) equal to 100 μm . The number in each figure corresponds to the normalized enthalpy (H^*) for each micrograph.

The morphology of the fusion zone and the bead width change based on processing parameters. A rounded fusion zone boundary is seen with the following conditions: low laser power, high processing speed and small working distance.

However, increased laser power, decreased processing speed and a larger working

distance create a wavy morphology of the fusion zone boundary. There was no obvious difference in fusion zone morphology between room temperature and heated substrates for the conditions studied.

The fusion zone morphology is linked to process parameters that directly impact the size, and temperature of the melt pool. For instance, increasing power and decreasing speed allows more energy to be transferred to the powder, substrate, and melt pool per unit length. The change in fusion zone morphology from rounded to wavy is explained by the surface tension induced Marangoni flow, in which fluid flows from lower to higher surface tension. The surface tension in IN718 exhibits a parabolic relationship with temperature and has a peak around 1530°C due to the presence of surface active elements (e.g., sulfur) [53]. In previous literature, a change in fusion zone morphology due to convective heat transfer has been shown to occur with varying concentrations of surface active elements [54].

The fusion zone morphology in laser deposited IN718 has been shown to be controlled by convective flow [53]. The force of convective flow induced by the Marangoni effect is expressed by the Marangoni number as shown in equation 4 [55].

$$Ma = \frac{\rho C_p \sigma \frac{d\gamma}{dT} (T_p - T_m)}{k\mu} \quad (4)$$

where ρ is the density of the liquid metal at the melting point, C_p is the specific heat of the liquid, σ is half the D4 σ beam width at the surface, $\frac{d\gamma}{dT}$ is the first derivative of surface tension versus temperature at the peak temperature, T_p is the peak temperature in the melt pool, T_m is the melting temperature, k is the thermal diffusivity, and μ is the effective viscosity of the liquid metal.

In the current investigation, the half width of the laser beam, temperature coefficient of surface tension ($\frac{d\gamma}{dT}$), and the peak temperature are the only variables in equation 4. A schematic of surface tension versus temperature for IN718, showing how the slope changes as a function of temperature, is shown in Figure 2.7. A positive slope results in a rounded fusion zone, while a negative slope creates a wavy morphology due to variations in convective flow within the melt pool. The direction of flow in the melt pool may change depending on the slope in the surface tension versus temperature plot. As the laser power increases and processing speed decreases the temperature distribution shifts to regions of higher temperature and increased slope. This represents an increase in the Marangoni number and results in a higher driving force for convective flow, resulting in increased flow velocities. The combination of the direction of melt pool fluid flow and the increased velocity creates the wavy fusion zone morphology with increased heat input.

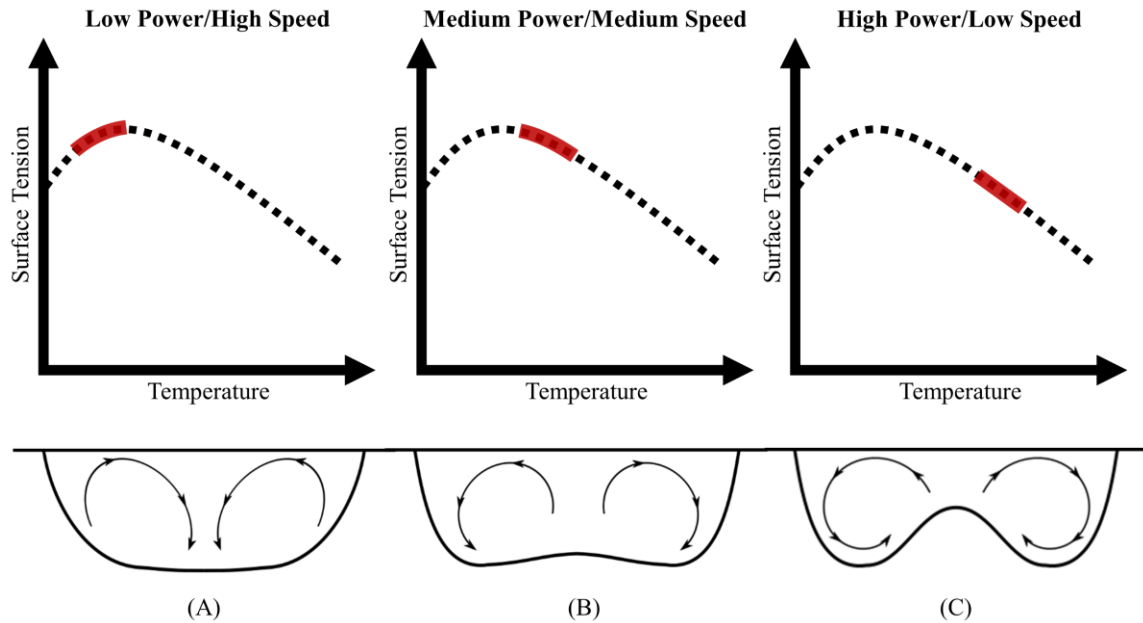


Figure 2.7. Schematic of surface tension and temperature curve for IN718. The red shaded region denotes a nominal melt pool temperature distribution for changing laser power and processing speed. (A) Low power and high speed, (B) Medium power and medium speed and (C) High power and low speed. Arrows in the melt pool schematics denote fluid flow direction.

As shown in the laser power and processing speed variable experiments, the wavy fusion zone became more prominent with increasing normalized enthalpy (Figure 2.4 and Figure 2.5). This correlation did not hold for variation in beam diameter (from increasing working distance) (Figure 2.6). Increasing beam diameter represents a decrease in normalized enthalpy, which should make a wavy fusion zone less prominent; however, increasing beam diameter is observed to make a wavy fusion zone more prominent. Therefore, normalized enthalpy cannot be used to explain the appearance of the wavy fusion zone with varying working distance.

All micrographs show the presence of a dendritic structure in the beads, which is shown more clearly in Figure 2.8, which compares microstructures for high and low normalized enthalpy conditions with and without substrate preheat. Quantitative secondary dendrite arm spacing is difficult to characterize in these samples due to the

chaotic nature of the microstructure and difficulty in identifying consistent secondary dendrite arm spacing.

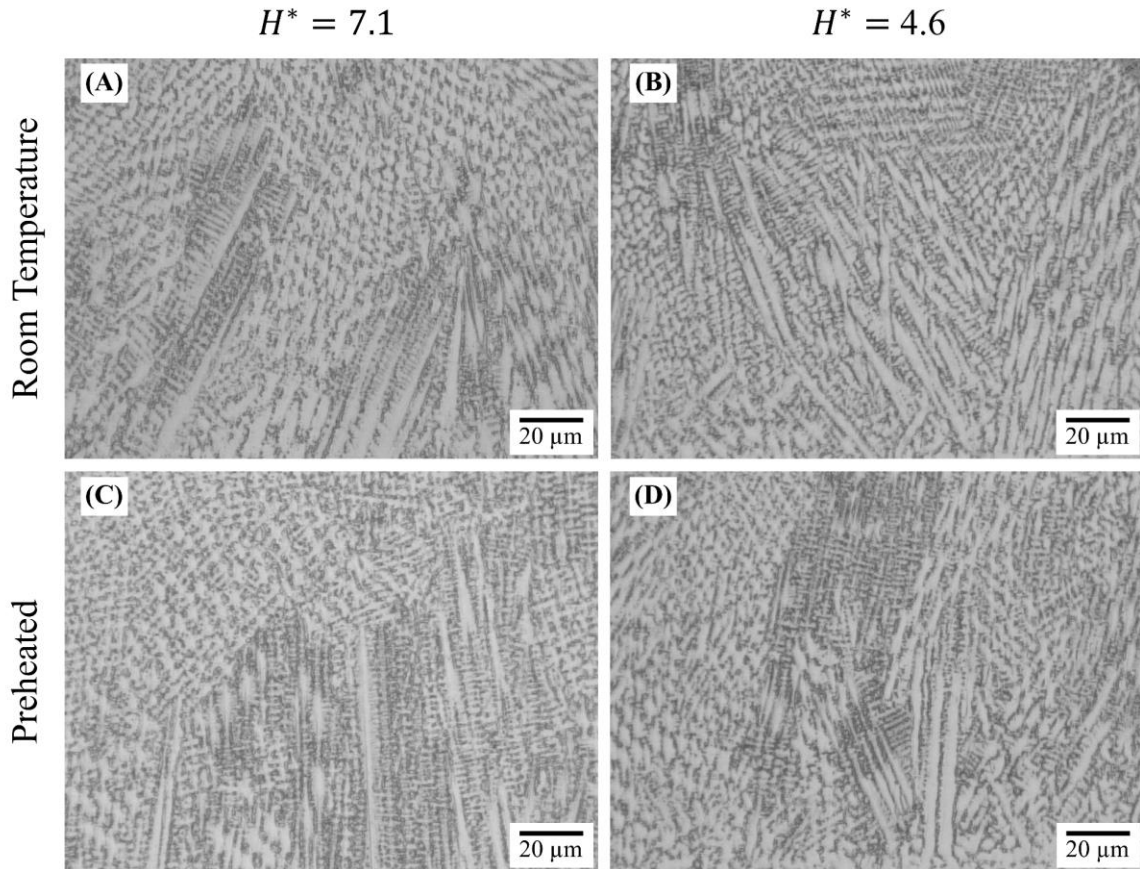


Figure 2.8. Microstructure images of dendrites at (A) Laser Power: 350 W, Processing Speed: 8.5 mm/s, Working Distance: 9.3 mm and Initial Substrate Temperature: 25°C (B) Laser Power: 250 W, Processing Speed: 10.6 mm/s, Working Distance: 9.3 mm and Initial Substrate Temperature: 25°C (C) Laser Power: 350 W, Processing Speed: 8.5 mm/s, Working Distance: 9.3 mm and Initial Substrate Temperature: 350°C (D) Laser Power: 250 W, Processing Speed: 10.6 mm/s, Working Distance: 9.3 mm and Initial Substrate Temperature: 350°C.

2.4.2 Effect of Processing Parameters on Bead Width and Fusion Zone Area

The width of the deposited bead was found to depend on processing parameters as shown in Figure 2.9. In the conditions used in the current investigation, increasing laser power from 250 W to 400 W with speed constant and decreasing speed from 16.9 mm/s to 8.5 mm/s with laser power constant, both had an effect on the bead width. Increasing

power from 250 to 400 W increases bead width by 424 μm , while slowing processing speed from 16.9 mm/s to 8.5 mm/s increased bead width by 168 μm . Therefore, for the conditions studied in the current investigation, increasing power by 150 W had more of an effect on bead width than abating the processing speed by 8.4 mm/s. Preheating the substrate preserves this result.

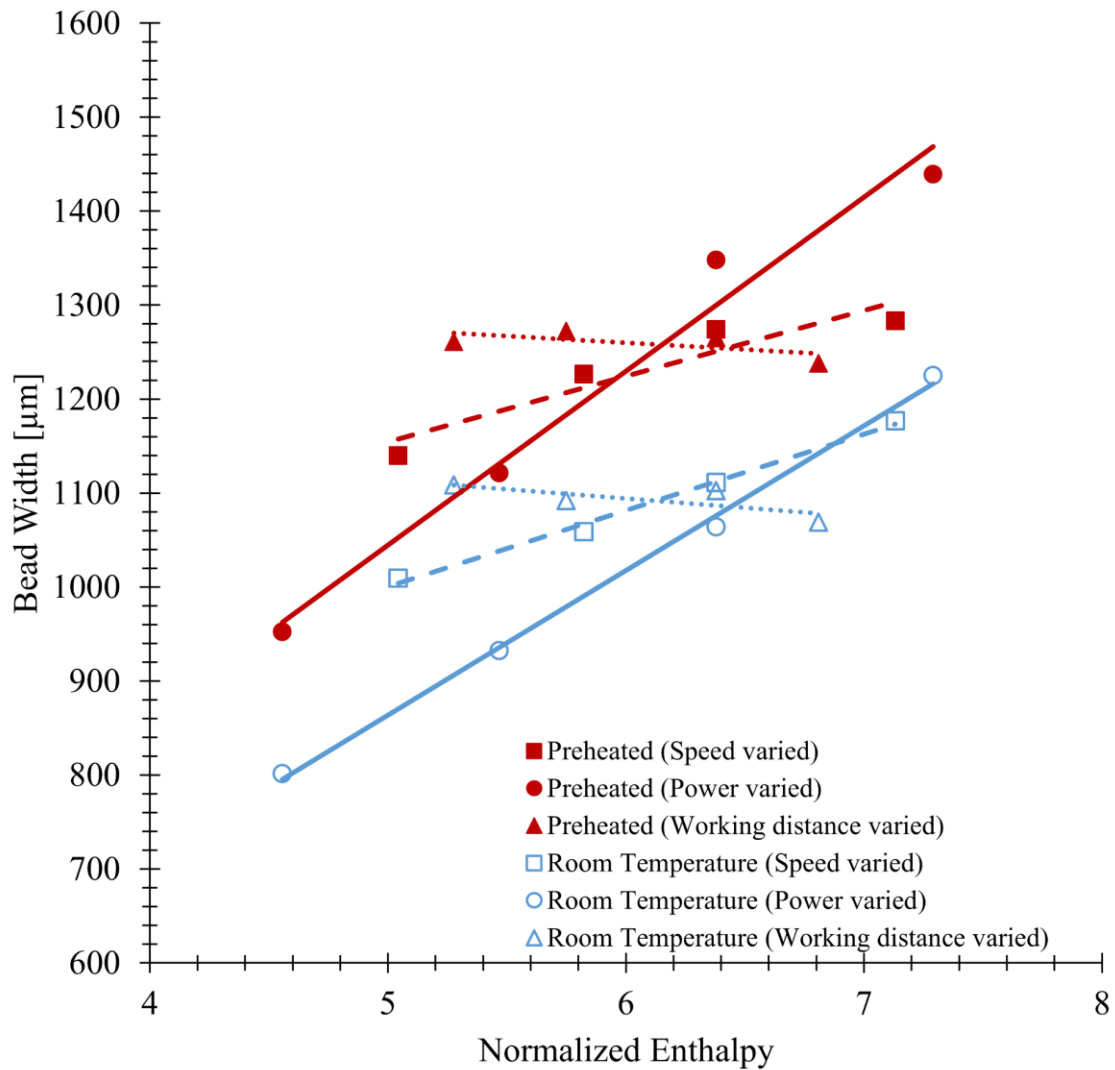


Figure 2.9. Plot of bead width with changing normalized enthalpy. Power, speed and working distance are varied and represented by squares, circles, and triangles respectively. Solid markers are preheated while hollow markers are room temperature.

Normalized enthalpy increases with decreasing processing speed. Increasing processing speed, which results in decreased normalized enthalpy, showed a decreased bead width. It should also be noted that powder flow is also affected by speed but not accounted for in the normalized enthalpy calculation. Ignoring the influence of powder flow, the energy imparted is dependent on processing speed and laser power. As the speed increases, less energy per unit volume is being imparted to the powder and substrate, which results in a smaller melt pool, and thereby a smaller bead width. As laser power increases, more energy is transferred to the powder and substrate, and a higher temperature in the melt pool is reached, which results in a larger melt pool and a wider bead.

Changing working distance had little effect on the resultant bead width. The normalized enthalpy calculation used in the current investigation does not encapsulate the powder flow distribution dependence on working distance as shown in Figure 2.3. At a working distance of 9.27 mm, the focus of the powder flow is below the surface of the substrate (Figure 2.3(a)). Therefore, increasing the working distance from 9.27 mm moved the powder distribution through its focus while decreasing the working distance moved the powder distribution further from the focus. The area blanketed by powder flow changes depending on the working distance from the substrate, which affects the capture efficiency of the melt pool with regards to the powder flow.

Substrate preheat increased the bead width by 180-200 μm and by an average of 16% over each corresponding room temperature case. An increased initial substrate temperature creates conditions for a wider melt pool. Through application of a substrate preheat, the energy input per unit volume necessary to reach the melting point is reduced.

Therefore, by applying the same energy input per unit volume to a preheated substrate, more material is melted and a wider melt track is created as compared to a room temperature substrate. A complimentary study by Corbin et al., [52] presents an empirical statistical model that describes the influence of processing parameters on external bead morphology in IN718 bead-on-plate experiments.

The variation in total fusion zone area shows a linear correlation with normalized enthalpy for laser power and processing speed, but a parabolic trend for changing working distance as shown in Figure 2.10. Higher laser powers and slower processing speeds apply more energy per volume that allows for increased melting of substrate and powder relative to low laser powers and fast processing speeds. Preheating the substrate increases the fusion zone area relative to the same room temperature cases.

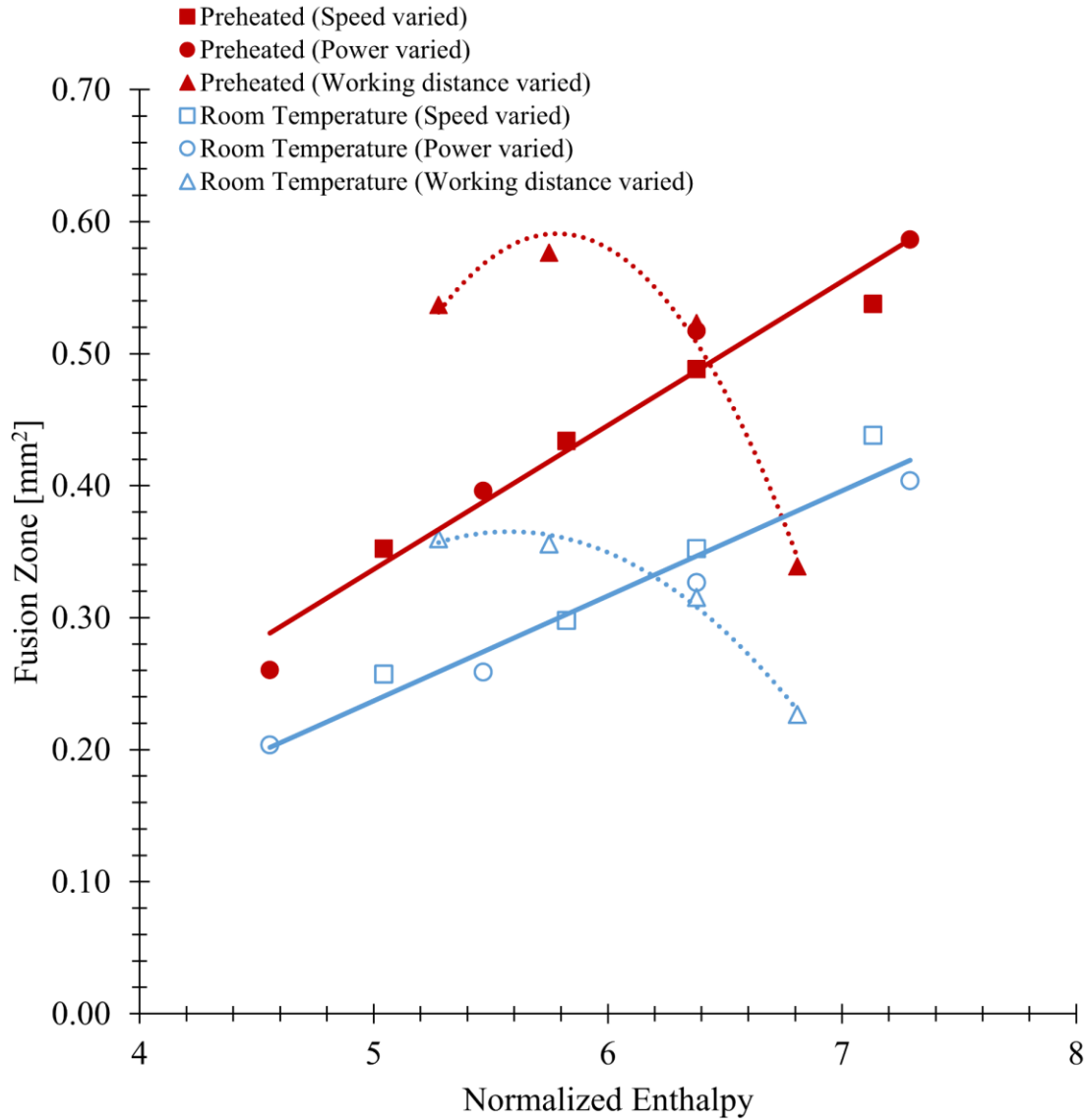


Figure 2.10. Plot of fusion zone area with normalized enthalpy. Power, speed and working distance are varied and represented by squares, circles, and triangles respectively. Solid markers are preheated while hollow markers are room temperature. Solid lines denote line of best fit for laser power and speed data. Dashed lines denote line of best fit for working distance variable data.

The parabolic trend of fusion zone area with working distance is explained by the powder flow distribution, shown schematically in Figure 2.3, though the relationship with normalized enthalpy is incidental due to the nature of beam spot size and powder flow geometry in this work. The data point of largest fusion zone corresponds to a working distance at the powder focal point where the most amount of powder is added into the

melt pool (Figure 2.3(b)). At the focused powder distribution, more powder is added into the melt pool relative to unfocused powder distributions (Figure 2.3(a) and (c)). Working distance above and below the powder focal point are cases with unfocused powder distribution, resulting in less powder captured and a smaller fusion zone area. Additional effects resulting from beam-powder interactions may also apply. Furthermore, by preheating the substrate, energy input per unit volume more readily melts the substrate and powder relative to the room temperature case.

2.4.3 Effect of Processing Parameters on Microhardness

Microhardness measurements were performed to assess the local mechanical properties of the deposit and underlying substrate. Microhardness indentations from the fusion zone, to the heat affected zone and into the base metal revealed a dependence of hardness on initial substrate temperature, but not on normalized enthalpy. Microhardness is indicative of a material's ability to plastically deform, and can be related to the material's yield strength [56].

The initial substrate temperature had a significant impact on the resultant hardness profile while the other processing parameters, and normalized enthalpy alone, had little effect. As shown in Figure 2.11, the room temperature initial substrate temperature shows large deviation in hardness between different normalized enthalpies especially in the fusion and heat affected zones. For the preheated substrates shown in Figure 2.12, with the same range of normalized enthalpies, the hardness profiles overlap in all cases and at all depths of the sample. This includes the fusion zone into the heat affected zone and finally the base metal. Furthermore, the hardness stayed uniform from the bead deposit and into the base metal relative to the room temperature test cases. These

findings may be applicable in repair applications where significant deviation in hardness between base metal and deposited material are not ideal.

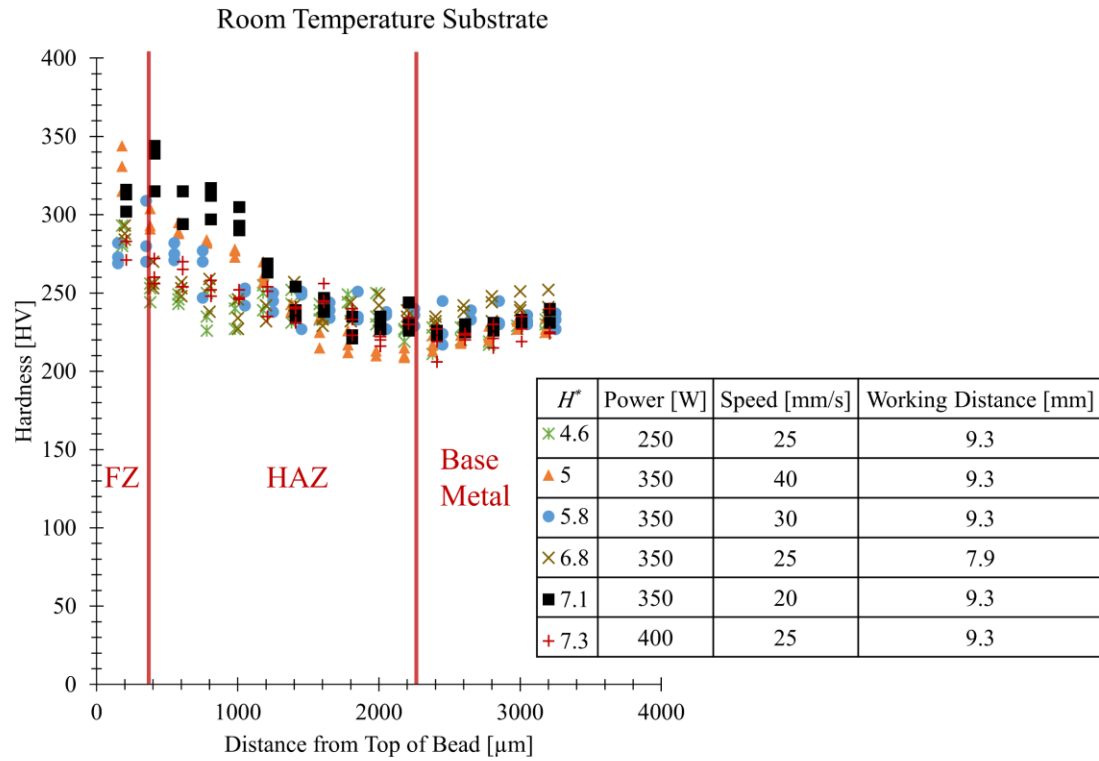


Figure 2.11. Hardness traverses along cross-sections of room temperature substrate deposits at different normalized enthalpies. Approximate fusion zone (FZ), heat affected zone (HAZ), and base metal regions are denoted.

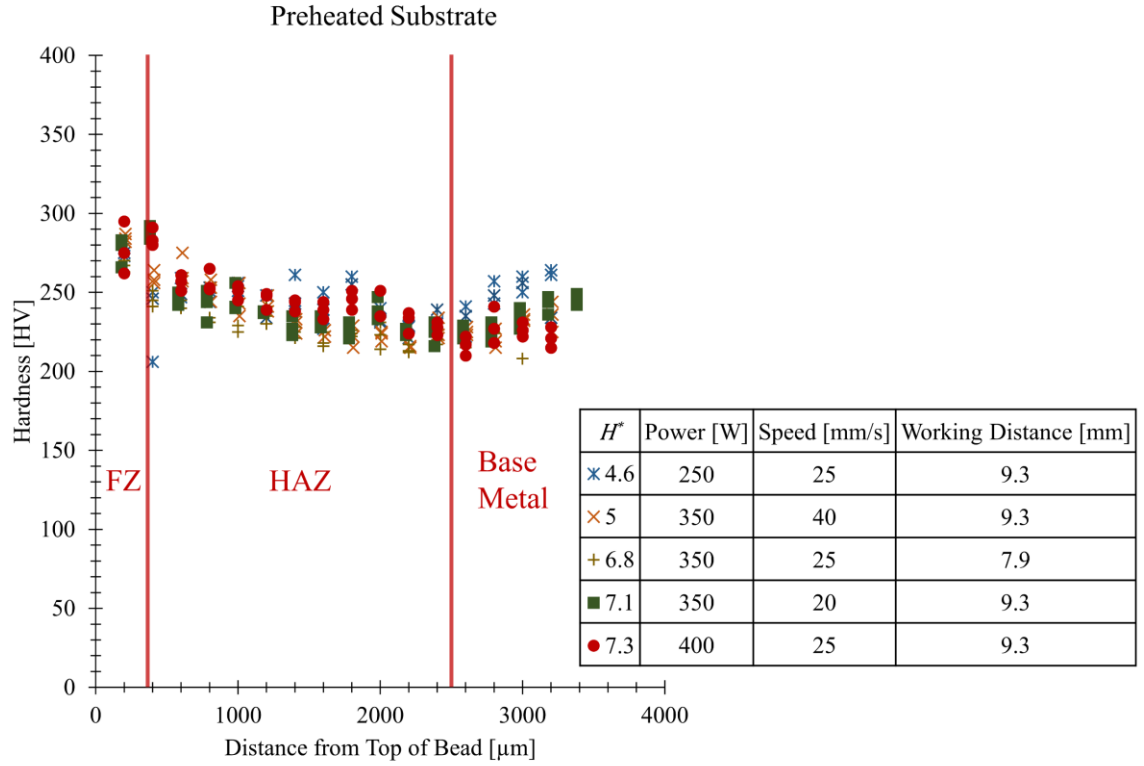


Figure 2.12. Hardness traverses along cross-sections of preheated substrate deposits at different normalized enthalpies. Approximate fusion zone (FZ), heat affected zone (HAZ), and base metal regions are denoted.

The reduction in deviation in hardness with substrate preheating can be explained using a calculation of the cooling rate at the center-line of a weld derived from the Rosenthal solution:

$$\frac{dT}{dt} = 2\pi k \frac{v}{\eta Q} (T_m - T_0)^2 \quad (5)$$

where k is the thermal conductivity, v is the processing speed, T_m is the melting temperature, T_0 is the substrate temperature, η is the surface absorptivity and Q is the laser power. An increase in T_0 results in a reduction of the cooling rate as well as a narrowing of the range of cooling rates due to variations in the linear heat input (v/Q).

As shown in Figure 2.13, the hardness in the fusion zone tends to increase with higher cooling rates across the conditions studied in the present investigation.

Figure 2.14 shows back scattered electron (BSE) scanning electron microscope (SEM) (FEI Quanta 200) images of the fusion zone in room temperature and preheated substrate cases. The room temperature and preheated runs pictured exhibited a hardness of 330 HV and 256 HV respectively, corresponding to the samples with highest and lowest fusion zone hardness in the present study. The bright regions in these images, corresponding to the interdendritic regions, were found to be enriched in Nb, Mo, and Ti compared to the matrix, which is indicative of the formation of brittle Laves phase [57]. The dispersion of the Laves phase in the room temperature case is finer than in the preheated case leading to higher hardness.

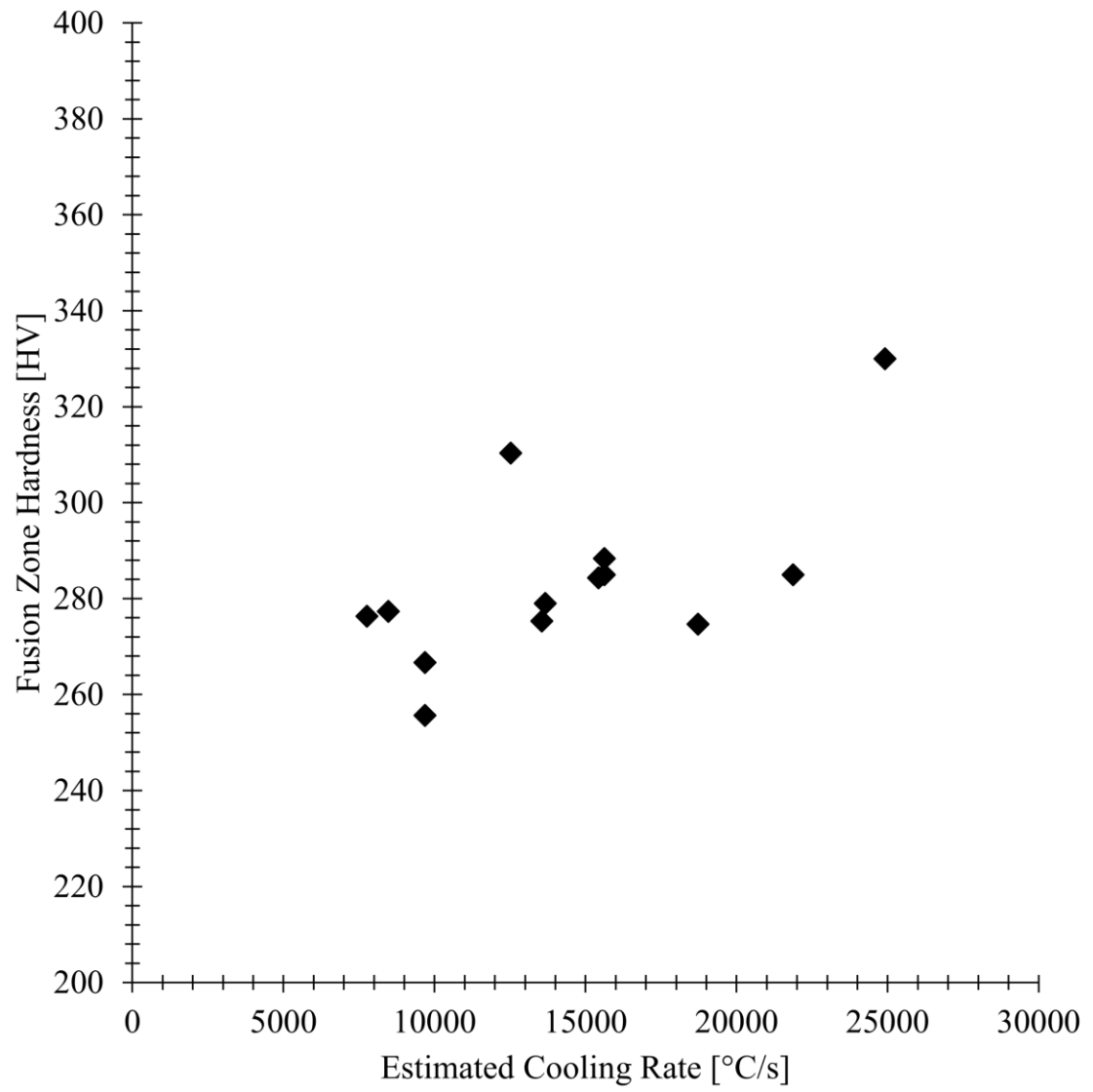


Figure 2.13. Hardness in the fusion zone as a function of cooling rate.

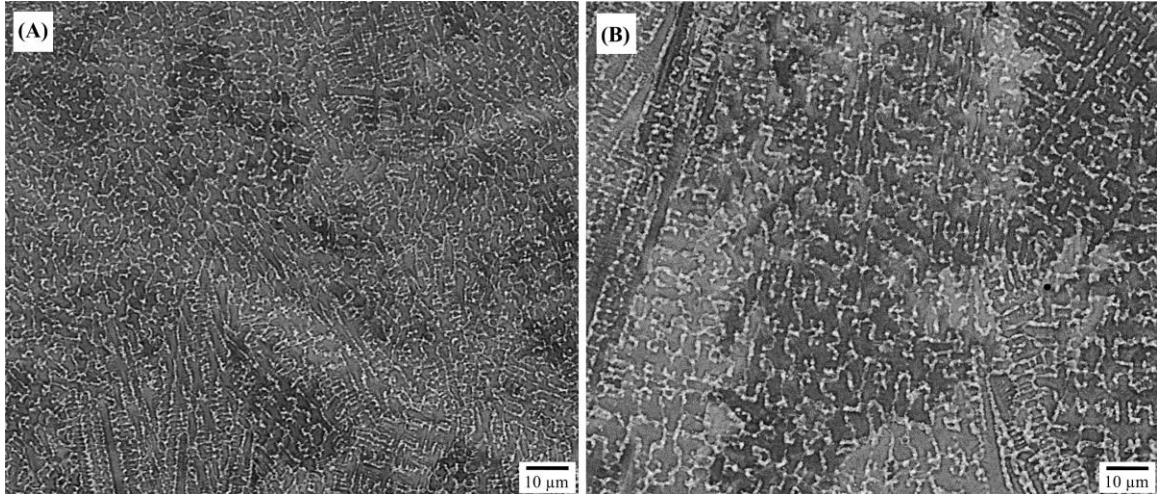


Figure 2.14. Back scattered electron SEM images of (A) High hardness, Laser Power: 350 W, Processing Speed: 16.9 mm/s, Working Distance: 9.3 mm and Initial Substrate Temperature: 25°C, and (B) Low Hardness, Laser Power: 350 W, Processing Speed: 10.6 mm/s, Working distance: 12.1 mm and Initial Substrate Temperature: 350°C.

2.5 Summary and Conclusions

The aim of this research was to supply experimental data towards the effect of processing parameters on various aspects of a single deposit by directed energy deposition and providing a physical explanation to the observed trends. This investigation studied the effect of power, speed, working distance and initial substrate temperature on the microhardness, fusion zone morphology, fusion zone area and bead width. Working distance encapsulates changing powder flow distribution and beam diameter. The key findings from this study are:

- Preheating the substrate increased the bead width and fusion zone area, and resulted in a similar hardness through the fusion zone to the base metal material. This may be of interest in applications where consistent mechanical properties between clad and base metal is needed.

- In room temperature cases, hardness increased from the base metal to the fusion zone. This may be applicable when a higher hardness clad relative to the substrate is desirable.
- Increased laser power and decreased processing speed showed a linear correlation with bead width and fusion zone area. However, changes to working distance showed little effect on bead width and a parabolic correlation with fusion zone area. This was attributed to a combination of factors, including changes in the heat input per unit area, coupled with changes in powder flow distribution at the surface of the substrate.
- Increasing laser power and decreasing processing speed created a wavy fusion zone due to increased Marangoni convection from higher melt pool temperature, while the same result was seen upon increasing working distance.

2.6 Acknowledgments

The authors would like to acknowledge the Office of Naval Research, under Contract No. N00014-11-1-0668. Any opinions, findings and conclusions or recommendations expressed in this publication are those of the authors and do not necessarily reflect the views of the Office of Naval Research. This material is based on research sponsored by Air Force Research Laboratory under agreement number FA8650-12-2-7230. The U.S. Government is authorized to reproduce and distribute reprints for Governmental purposes notwithstanding any copyright notation thereon. The views and conclusions contained herein are those of the authors and should not be interpreted as necessarily representing the official policies or endorsements, either expressed or

implied, of Air Force Research Laboratory or the U.S. Government. Mr. Ed Good, Kyle Snyder and Gabrielle Gunderman from the Pennsylvania State University Center for Innovative Material Processing Through Direct Digital Deposition (CIMP-3D) are thanked for their assistance in metallographic preparation and hardness measurements. The authors also acknowledge the support of Tom McDonald and Optomec in the completion of this work.

Chapter 3: Single Bead Experiments: Ti-6Al-4V

3.1 Introduction

Directed energy deposition (DED) is an additive manufacturing (AM) process that utilizes a laser to create a melt pool on a substrate, within which powder or wire feedstock is added to create a deposited bead. In DED, beads are deposited adjacent to one another to create a layer and upon completion of one layer, the stage or laser head moves in the z-direction and the next layer is deposited on top of the previous. In this, intricate 3-dimensional components can be made because of computer numeric control (CNC) allowing for precise x-y-z stage and laser head movement from inputted computer automated design (CAD) files. However, DED has also found application for repair of worn high value parts and generation of hard facing coatings (i.e., laser cladding) [58].

Ti-6Al-4V is the most widely used titanium alloy in industry [32]. The combination of high tensile strength, low density, and exceptional corrosion resistance makes the alloy ideal for use in critical applications that require lightweight advanced materials (i.e., aerospace and biomedical) [33]. Ti-6Al-4V is costly and difficult to machine; therefore, as a cost saving measure, additive technologies may be used to create near net shape components. Furthermore, additive approaches can be used to repair components by replacing worn material and eliminating the need to replace the entire part [59].

The microstructure and mechanical properties of single bead deposits of Ti-6Al-4V using wire feedstock with a laser heat source have been characterized by Brandl and co-workers over a range of laser powers (1.75 – 3.5 kW), processing speeds (7.5 – 40 mm/s) with a beam diameter of 4.1 mm [60], [61]. In the microstructure, the authors note

a fusion zone (FZ) in which material was completely melted during processing, and columnar grains were formed. The alpha laths in the FZ were found to have a martensitic, basketweave structure. Furthermore, the authors found a multi-region heat affected zone (HAZ) comprising $(HAZ)_\beta$ and $(HAZ)_{\alpha+\beta}$. The authors qualitatively characterized the microstructure with changing laser power and speed by measuring the width of prior β grains in the FZ and size of globular prior β grains in the $(HAZ)_\beta$ region. The authors showed that the width and size of prior β grains increased with increased linear heat input (increased laser power, decreased processing speed).

Brandl and co-workers also studied the impact of parameters on the dimension and hardness of single beads made by wire-fed laser deposition [61]. The hardness of the deposited material and base metal were found to be dependent on the microstructural region where the $(HAZ)_\beta$ region exhibited higher hardness than both the added material and the base metal. The authors suggest this phenomenon is two-fold. First, higher amounts of interstitial alloying elements (C, O, N, etc.) were found in the substrate material relative to the wire feedstock creating a harder material in the $(HAZ)_\beta$ region compared to the deposit. Second, the $(HAZ)_\beta$ region experienced temperatures greater than the β transus followed by extremely fast cooling resulting in a fine microstructure and higher hardness than the unaffected base metal. Processing parameters had an effect on the hardness where increased laser power led to increased hardness in the FZ meanwhile no relationship was noted with processing speed. The authors suggest the increased laser power in the ranges studied had a larger effect on the solidification rate compared to processing speed. Furthermore, bead dimensions were affected by linear heat input where increased linear heat input (i.e., increased laser power, decreased

processing speed) increased the area of the FZ and (HAZ)_β while creating wider, but shorter deposited beads. The angle of repose is the tangential angle the bead makes with the substrate and was shown to decrease with increased linear heat input. The results presented by Brandl and co-workers provide an excellent starting point for comparison of single bead hardness and geometry trends between alternative DED methods that utilize different feed stock (i.e., powder and wire). The present paper works to elucidate trends found in DED single beads using powder feedstock and compare the results to those found by Brandl and co-workers.

Sun and Hao studied the effect of laser power (332 – 668 W), processing speed (7.2 – 12.8 mm/s), and powder feed rate (20 – 70 rev/min) on the single bead geometry in DED of Ti-6Al-4V metal powder using a non-commercial AM system with beam diameter at processing height of 2 mm in an effort to determine the most important variable to the bead geometry [62]. The authors found powder feed rate was the most significant processing parameter for bead height and width. Meanwhile, melt pool penetration was most affected by processing speed. All relationships between the powder feed rate and measured outcomes were reported to be linear; however, laser power and height, laser power and width, and processing speed and width showed parabolic relationships. While this study contributes vital information for bead geometry, it does so using an average of cross-sectional measurements that may not be fully representative of the entire bead. Furthermore, the local mechanical property change from the bead to the base plate and between processing conditions were not studied.

In order to fully understand the DED process, one must first understand the geometry of a single bead. Megahed and co-workers showed results of simulation and

experimental work that reveal overlap percentage between adjacent beads had an effect on the final surface quality [63]. Joshi and co-workers elaborated on this in experimental and simulation of two beads placed at different overlap distances using a wire-fed welding technique [64]. They found varying degrees of overlap between beads had a topological effect on the geometry of two deposited beads. Therefore, the work done by these authors show the need to examine the geometry of a single bead deposit to be confident in the inputted processing parameters.

The present paper aims to present a systematic examination of the geometry, FZ, and microhardness of a single bead deposited by DED as a function of inputted processing parameters for a commercially available and widely used DED machine. Quintessential to the DED and AM processes is the understanding of a single bead. Prior to multi-bead, multi-layer build-up, single bead geometry must be evaluated in order to tune the mechanics of the system (e.g., hatch spacing, layer thickness, etc.) to properly complete a build without significant defects (e.g., surface topology, lack-of-fusion porosity, etc.). In this work, we vary laser power and processing speed independently to see how these parameters impact bead geometry, microstructure, and hardness. Furthermore, a non-destructive evaluation tool is compared to traditional metallographic geometry measurements to determine its accuracy in measuring geometric features.

3.2 Experimental

An Optomec[®], Inc. LENS[®] MR-7 directed energy deposition (DED) additive manufacturing system, equipped with a 500 W IPG Photonics Yb-doped fiber, was used to deposit the single beads in this study. The laser processing head in this system utilized four copper nozzles with orifice diameter of 1.19 mm to direct powder into the melt pool created by the laser. The laser is directed to be perpendicular to the substrate. The working distance between the tip of the copper nozzles and substrate was 9.27 mm. Beam characterization diagnostics completed using a Primes[®] FocusMonitor system determined the $D4\sigma$ width of beam at the substrate to be 990 μm using ISO standard 11146-1 [65]. The powder flow rate was 3.0 g/min. Argon gas was flowed coaxially with the laser and through the powder feeding nozzles at 30 lpm and 4 lpm, respectively. To minimize oxygen contamination, the build chamber was purged to less than 20 ppm oxygen content prior to processing. In this system, the stage moves in the x-y plane at a specified speed referred in this report as the “processing speed”. In these experiments, one continuous bead was deposited with laser power and processing speed varied through deposition as shown in Figure 3.1. The length of each deposition was 13.37 cm in length with parameter adjustment every 1.91 cm.

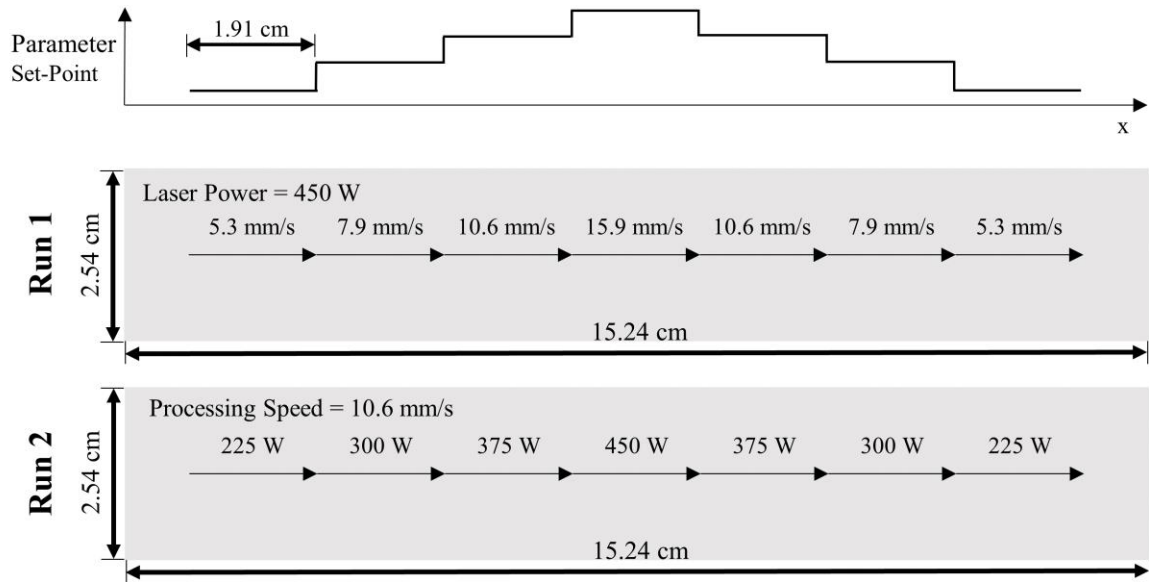


Figure 3.1. Schematic of tool path and variable variation.

A Ti-6Al-4V substrate of dimensions 15.24 cm by 2.54 cm with a thickness of 0.25 cm was used. Prealloyed Ti-6Al-4V extra low interstitial (ELI) spherical powder produced by Phelly Materials Inc. was used in this study. The powder was sieved using mesh sizes of -100/+325 corresponding to a powder diameter range of 45-150 μm . Chemical composition of substrate and powder material are shown in Table 3.1. Powder composition was given by the manufacturer while substrate oxygen and nitrogen content were measured by inert gas fusion and carbon by combustion infrared detection.

Table 3.1. Chemical composition (in weight percent) of substrate and powder used in these experiments. Substrate was only characterized for O, N, and C to determine discrepancies with powder.

	Ti	Al	V	Fe	O	N	C
Substrate	-	-	-	-	0.186	0.008	0.028
Powder	Balance	5.94	4.0	0.13	0.07	0.04	0.01

Samples were cross-sectioned and polished in order to examine micro and macrostructural features. Beads were sectioned at the midpoint of each parameter change. Standard metallographic preparation was used with a final polishing step of 0.05

μm colloidal silica for 8 minutes. Samples were etched using Kroll's reagent that conformed to ASTM E407 [66].

Hardness measurements were taken in the bead and into the baseplate, with three indents at each height as shown in Figure 3.2 using a Vickers indenter (LECO M-400-G1) with an applied load of 300 g and a dwell time of 10s. Uncertainty in these measurements was determined to be ± 5 HV.

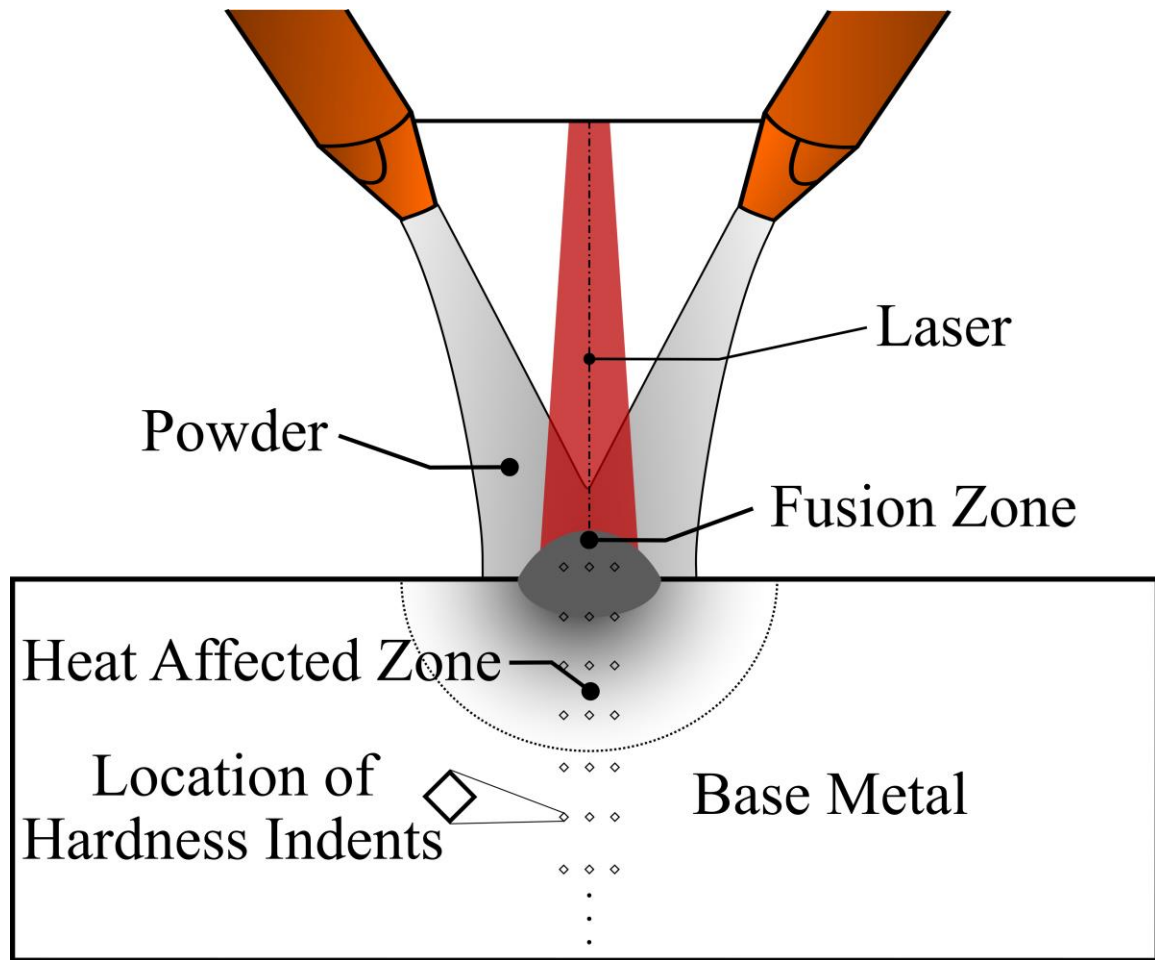


Figure 3.2. Schematic of powder fed DED process with key measurement locations labeled.

Bead geometry measurements were taken using two techniques: metallography and optical profilometry. Metallographic measurements were made using the ImageJ image processing software. Optical profilometry was conducted on a Zygo® NewView

7300 equipped with a 2.75x zoom Michelson interferometer lens and using a 3X coherence scanning interferometry (CSI) measure mode. Individual images were stitched together in the x-y plane to obtain the data across the entire bead in one scan. Profilometry data was analyzed using MATLAB. An algorithm was developed to analyze every cross-section along the length of the bead. First, a third-order median filter was used to reduce experimental noise. In order to determine bead geometry, the algorithm recognized flat regions of the profilometry data as the substrate material. A set threshold in the z-direction was used to determine the edges of the bead in the x-y plane and the bead width was the difference between the bead edge x-coordinates. Next, a second order polynomial was fit to the bead cross-section. Height was calculated as the difference between the top of the second order polynomial and the substrate. Angle of repose was calculated as the angle between the detected substrate and the fitted polynomial.

3.3 Results and Discussion

3.3.1 Internal Bead Characterization (Fusion Zone, Heat Affected Zone and Microhardness)

A macrograph of a representative bead with the key discernable features labeled is shown in Figure 3.3, where three distinct regions are visible. A FZ is seen propagating into the substrate showing that a metallurgical bond exists between the deposited bead and the substrate material. The FZ is distinguished from the other microstructural areas because it contains large columnar prior β grains that grew in the direction of largest thermal gradient (i.e., toward highest temperature created by laser). The HAZ is the region where the microstructure is visibly affected by the heat input. In Ti-6Al-4V the HAZ is separated into two different regions, $((\text{HAZ})_\beta$ and $(\text{HAZ})_{\alpha+\beta}$) and are

distinguished by a change in color as shown in Figure 3.3. The $(HAZ)_\beta$ region is the area in closest proximity to the FZ and is characterized by a dark gray color where prior β grains are not columnar. This region experienced temperatures greater than the β transus allowing for significant prior β grain coarsening relative to the non-heat affected base metal. The second HAZ region, $(HAZ)_{\alpha+\beta}$, is characterized by a light grey color in Figure 3.3. This region did not exceed temperatures higher than the β transus temperature, but was exposed to excessive temperatures that resulted in a microstructural transformation, specifically growth of existing α laths from the original base metal.

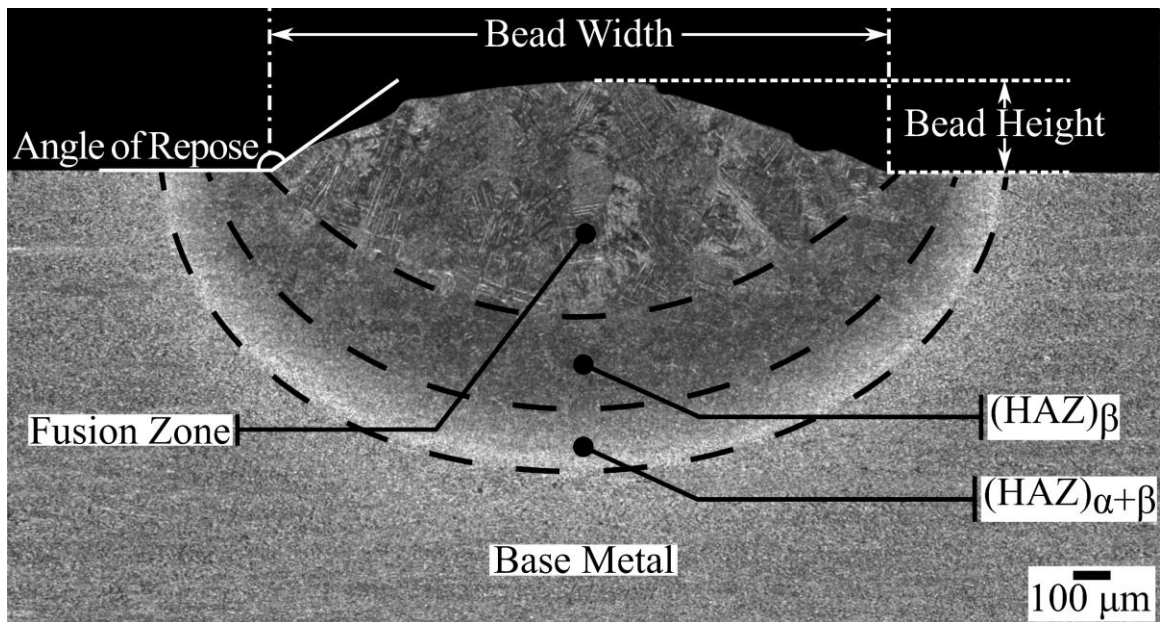


Figure 3.3. Overlay of key microstructural areas and measurements.

Macrostructural overviews of all samples in the present study are shown in Figure 3.4 and Figure 3.5 corresponding to varying laser power and processing speed, respectively. All samples had hemispherical FZ and HAZ that propagate into the substrate and increased with increased heat input.

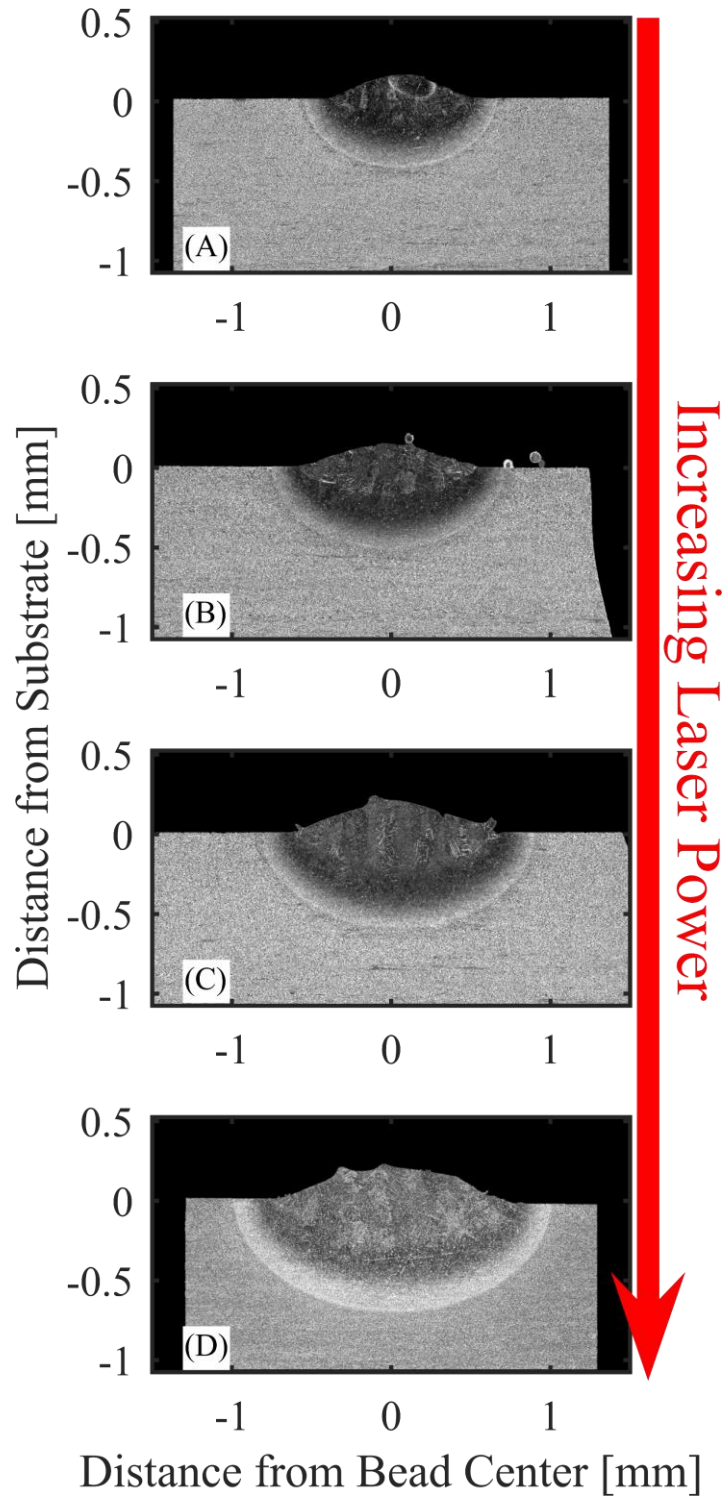


Figure 3.4. Optical macrographs of variable laser power cases. (A) 225 W, (B) 300 W, (C) 375 W and (D) 450 W. Processing speed held constant at 10.6 mm/s.

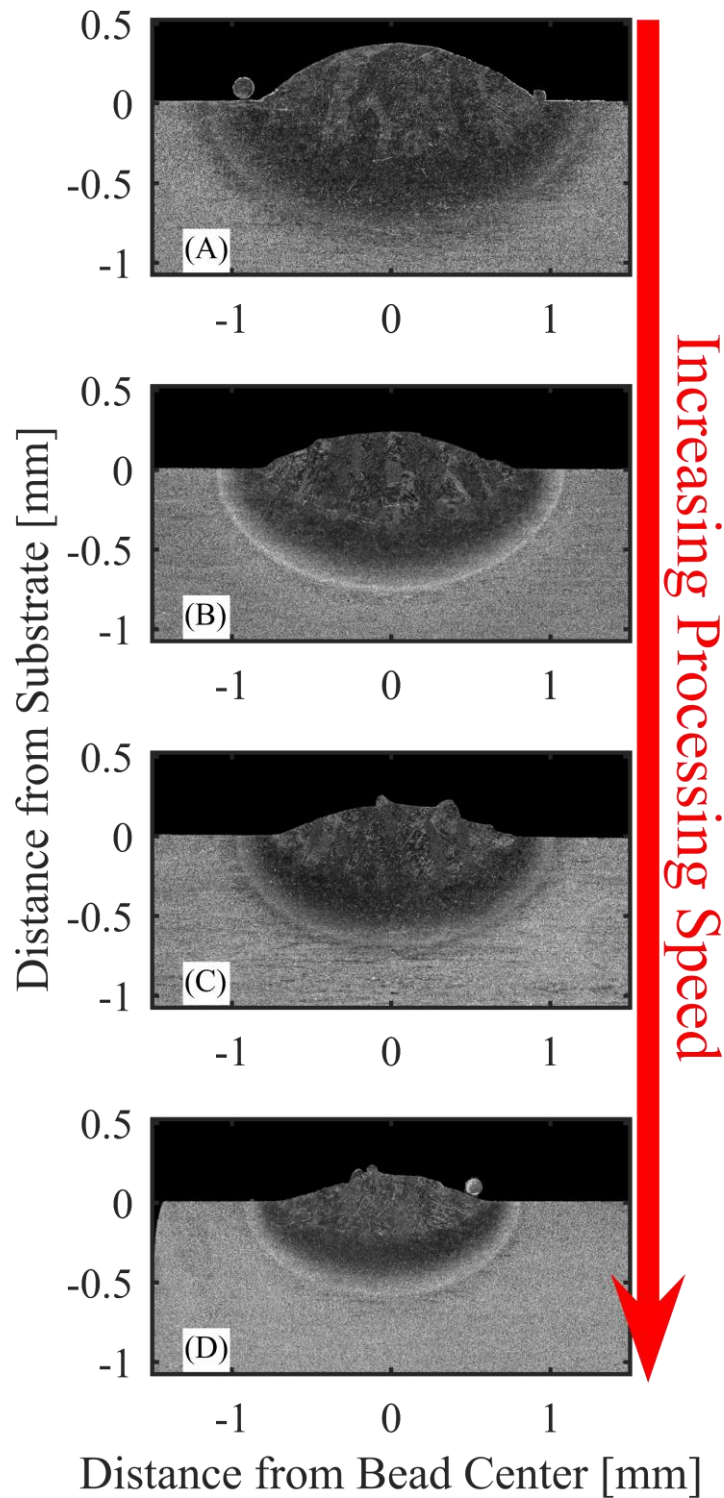


Figure 3.5. Optical macrographs of variable processing speed cases. (A) 5.3 mm/s, (B) 7.9 mm/s, (C) 10.6 mm/s and (D) 15.9 mm/s. Laser power held constant at 450 W.

The area of the fusion zone was determined using ImageJ, and as a function of linear heat input is shown in Figure 3.6. We note a linear correlation between FZ area with increased heat input. As heat input increases, more energy is available to melt the underlying substrate resulting in more base metal and feed stock material being fully melted. In the ranges studied, the change in FZ area increased linearly with increasing linear heat input. This trend is widely reported in laser-welding literature [67]–[71]; however, it is necessary to study the FZ geometry for a powder-fed DED approach as it is of greater consequence in AM than traditional welding techniques. One may expect the FZ area to increase more with decreased processing speed compared to increased laser power because slower processing speed allows more powder to be injected into the melt pool relative to fast processing speeds. However, changing laser power does not change the rate of powder fed into the melt pool. The change in FZ area was linear as shown in Figure 3.6 with increased linear heat input and not dependent on the varied parameter. Therefore, it is speculated as laser power is increased, the temperature in the melt pool increases, and captures more powder particles creating a larger FZ at the same rate as decreased processing speed.

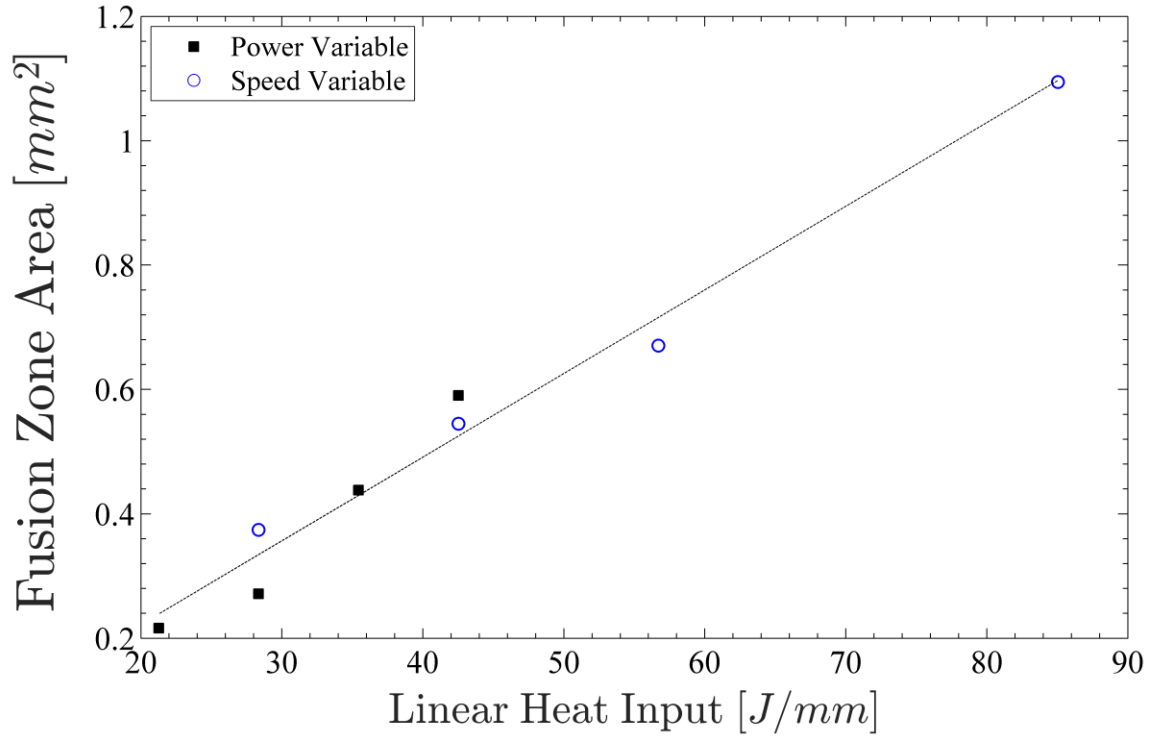


Figure 3.6. Fusion zone propagation area as a function of linear heat input.

Microhardness as a function of depth in the deposit is shown in Figure 3.7. The vertical dashed lines denote the metallographically measured $(HAZ)_{\alpha+\beta}$ distance from the top of the deposit for each case. The set of data points nearest the top of the bead show hardness of the FZ where the sample produced by highest linear heat input (85 J/mm) exhibits slightly lower FZ hardness ($363 \text{ HV} \pm 10 \text{ HV}$) relative to samples made by lower laser power. This trend is similar to that noted by Shanmugarajan and co-workers who studied the effect of welding parameters on the microstructure and mechanical properties of laser welded borated stainless steel [72]. They found a decrease in FZ hardness with increased heat input and attributed it to a more refined microstructure in the low heat input case.

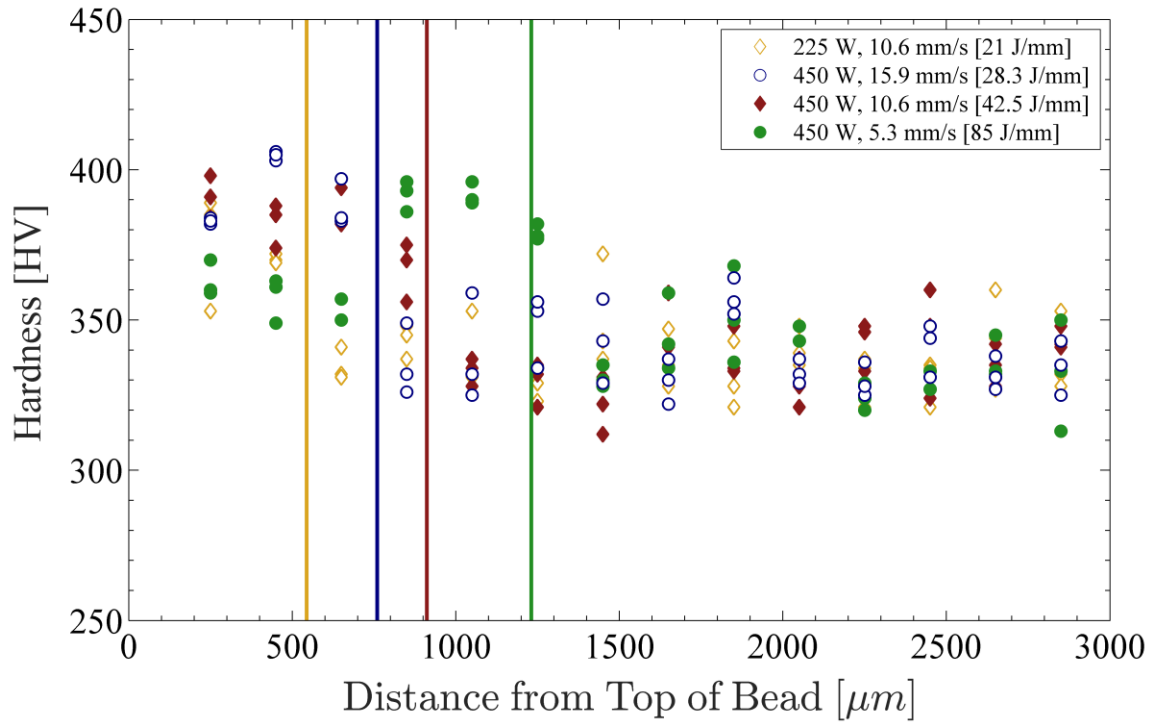


Figure 3.7. Microhardness as a function of distance from the top of the bead. Closed circles and filled squares denote power and speed variable data respectively. Lines show the metallographic measured heat affected zone from the top of the bead.

A sharp decrease in hardness is present at the HAZ and base metal boundary.

High hardness is retained deeper into the sample of highest linear heat input (85 J/mm) with $(HAZ)_{\alpha+\beta}$ depth of 846 μm ; while, lowest linear heat input (21 J/mm) corresponded to shallowest $(HAZ)_{\alpha+\beta}$ depth of 429 μm . In all studied cases, the FZ and HAZ exhibited a greater hardness than the non-heat affected substrate material. The FZ of each sample is subjected to high cooling rates, leading to a fine microstructure relative to the base material. Therefore, the FZ is expected to show an increased hardness. Additionally, as expected, the HAZ remains harder than the base material. This is likely from the rapid increase in temperature and subsequent fast cooling induced by the deposition process. Furthermore, the solidification process could result in large amounts of residual stress in

the HAZ area especially for low laser powers and high processing speeds that would affect the HAZ hardness[73].

Interestingly, the highest hardness in the sample with largest linear heat input was not located in the FZ; but rather in (HAZ)_{α+β} region. The (HAZ)_{α+β} microstructural area corresponds to the region that did not experience significant prior β grain growth because temperatures did not exceed the β transus. Therefore, smaller grains relative to the FZ allow more boundaries to prevent dislocation movement; thus increasing hardness by the Hall-Petch relationship. Furthermore, as shown in Table 3.1 the amount of interstitial strengthening elements (e.g., O, N, and C) differs between the substrate and powder. An oxygen equivalent number may be calculated as [74]

$$O_{eq} = O + (2 \times N) + \left(\frac{2}{3} \times C\right) \quad (6)$$

where all values are in weight percent. Computation of the oxygen equivalence in the substrate and powder are 0.221 wt. % and 0.157 wt. %, respectively. Therefore, a larger amount of interstitial elements caused the higher hardness in the HAZ relative to the FZ. As shown by Donachie, small amounts of oxygen (e.g., 0.1 wt. %) can increase the Vickers hardness by as much as 50 HV [33].

A conceivable explanation for why this is not seen in all samples is due to the size of the HAZ. Indents are ~40 μm large and require a spacing between measurements of 2.5 times the width of the indents as specified by ASTM E384 [75]. Therefore, more indents are possible in the highest linear heat input (85 J/mm) case as it has a significantly larger (HAZ)_{α+β} depth (846 μm) relative to the lowest linear heat input (21 J/mm) case (429 μm). The spacing between indents was held constant at 200 μm for all samples.

3.3.2 External Bead Characterization (Width, Height, and Angle of Repose)

Bead height as a function of linear heat input is shown in Figure 3.8. Both metallographic and profilometry data show a linear trend upon increasing linear heat input. The profilometer box plots represent all measurements taken on beads deposited using a given linear heat input. Metallographic data is comparable to the profilometry data, as the metallographic data points appear between the 25th and 75th quantile ranges denoted by the box in the box plot. Bead height increased with increased linear heat input because of a higher peak melt pool temperature, which allowed for more efficient capture and melting of the powder.

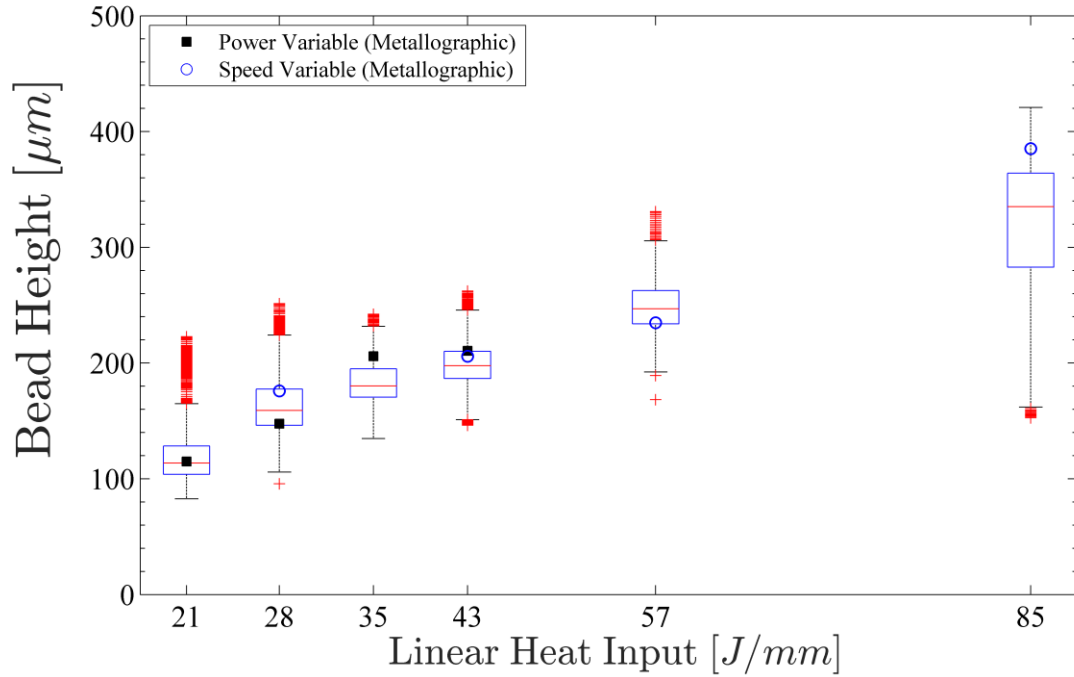


Figure 3.8. Profilometer and metallographic bead height as a function of linear heat input.

Bead width as a function of linear heat input is shown in Figure 3.9. We note a correlation between bead width and increased linear heat input. Metallographic data is comparable to profilometry data. Bead width increased with linear heat input because of

higher temperatures in the melt pool at high linear heat inputs. The viscosity of the liquid metal drops with increasing temperature allowing for a higher degree of melt pool spreading on the surface of the substrate. However, the degree of bead width increase was dependent on the varied parameter where width increased at a faster rate with laser power compared to processing speed.

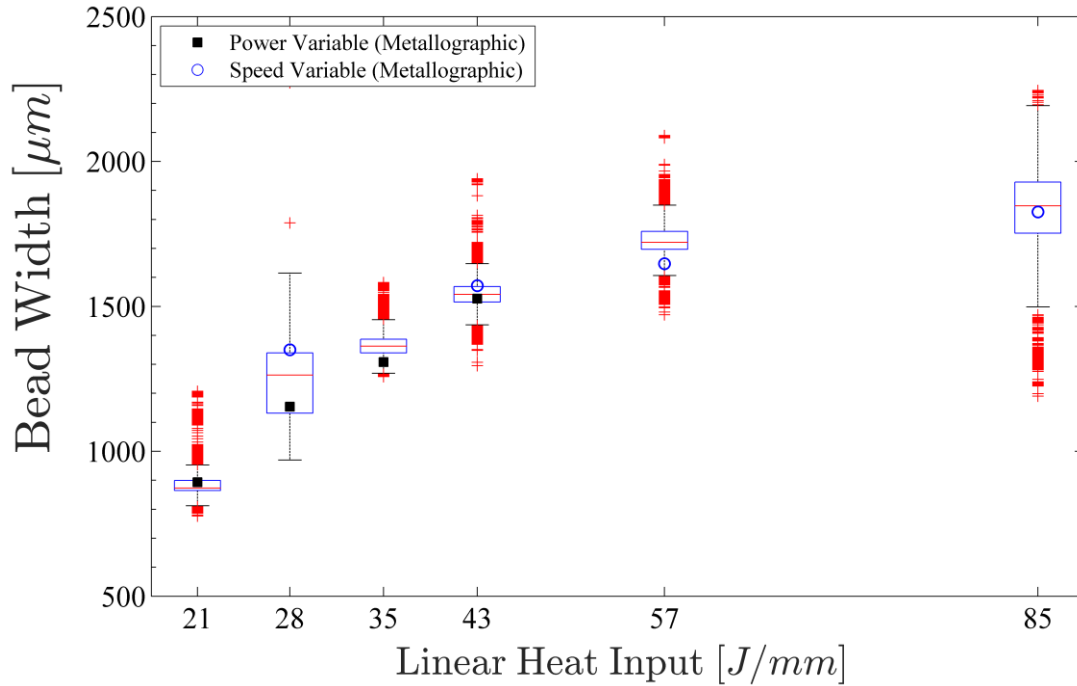


Figure 3.9. Profilometer and metallographic measured bead width as a function of linear heat input.

These results differ with the trends found by Brandl and co-workers who studied the effect of laser additive manufacturing parameters on the geometry of single beads beginning with wire feedstock [61]. Their work showed a competing effect between the width and height (i.e., width increase was compensated by a height decrease, and vice versa). In the current study width and height are both shown to increase with increased heat input where we used a powder feed approach that is significantly different than the wire feed approach used in the work by Brandl in which wire is delivered to the melt pool at a consistent rate. Therefore, the amount of material deposited is steady resulting in a

competition between bead width and height (e.g., increased height, decreased width). However, in powder-fed DED, not all powder particles fed through the powder nozzles are melted and the amount collected in the melt pool is a function of processing speed and laser power (i.e., temperature of the melt pool). As discussed in detail by Zekovic and co-workers, powder is captured and melted in the molten pool [76]. Therefore, with a hotter and larger molten pool (i.e., high heat input) more powder was captured and a wider and taller bead was created.

Angle of repose as a function of linear heat input is shown in Figure 3.10. For profilometer data, angle of repose tends to decrease with increasing heat input. This is not as profound an effect as that shown by bead width and height. Metallographic angle of repose data is not consistently near the median of the angle of repose profilometry data set. This is because the change in angle between processing parameters is small relative to the other studied dependent variables (height and width). Metallography only accounts for one cross-section of the sample and may not be representative of the bead as a whole. This uncertainty is magnified when changes in the studied dimension is small. Profilometry accounts for an entire bead and is suggested to be better in revealing trends when changes are small.

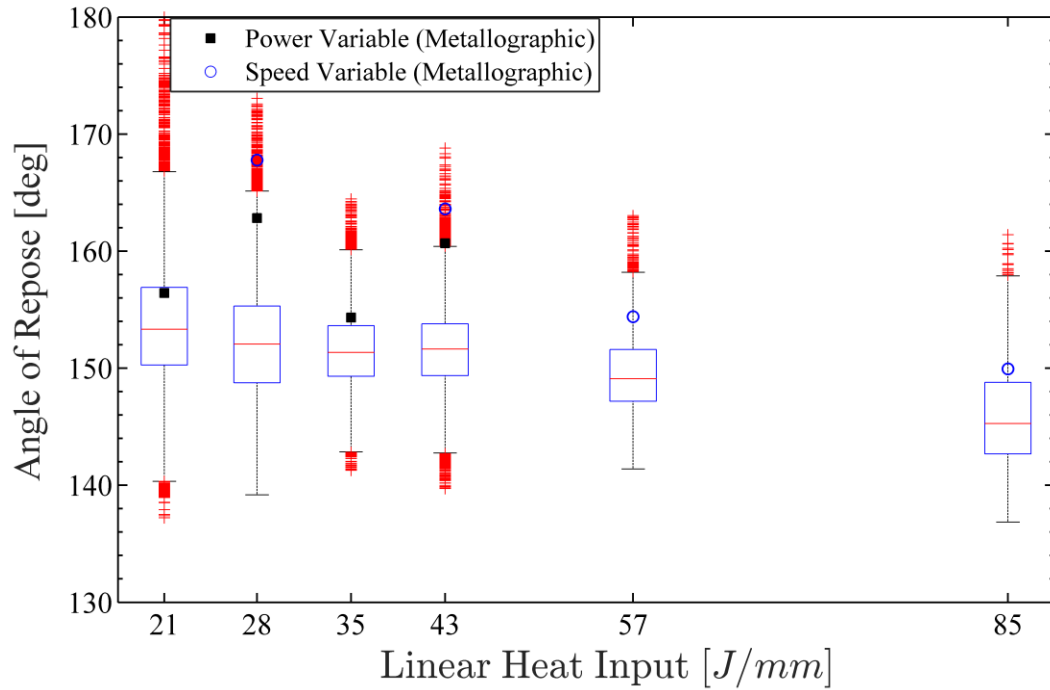


Figure 3.10. Profilometer and metallographic measured angle of repose as a function of linear heat input.

The metallographic data points for the power variable experiments do not reveal strong correlation; however, speed variable metallographic measurements show a clear decrease in angle of repose with decreased processing speed (increased linear heat input) revealing a similar trend to profilometer data. The correlation between linear heat input and angle of repose is explained as the width and height of the beads are both shown to increase with increasing heat input. However, the height of the bead appears linear with increasing heat input while the width does not increase linearly at the highest heat input. Because of the comparatively large increase in height relative to the width increase, the angle of repose drops slightly. At increased laser power and decreased processing speed a higher melt pool temperature is reached allowing for capture of more powder and a taller bead; thus a smaller angle of repose.

3.4 Summary and Conclusions

The current study focused on single beads of Ti-6Al-4V deposited by powder-fed DED to elucidate the effect of changing laser power and processing speed on the bead dimensions (i.e., height width, and angle), microstructure (i.e. FZ, heat affected zone, base metal), and microhardness. Furthermore, two different approaches were used to measure the exterior bead geometry, one destructive and one non-destructive. The current study adds to previous research by expanding on the impact DED processing conditions have on the geometry of a single bead deposit and compares the observed trends to different feedstock methods. The following are the key conclusions from this study:

- The FZ area (region that exhibited columnar grains) showed a strong linear trend with increased linear heat input independent of which processing parameter was varied, e.g., laser power and processing speed.
- The FZ hardness was not dependent on processing parameters. No correlation in FZ hardness was seen with changing laser power or processing speed.
- Bead width and height increased with linear heat input. Height increased linearly; however, bead width reached a threshold at the highest linear heat input, thereby resulting in an increasingly shallow angle of repose.
- Metallographic data largely appeared to be representative of the profilometry data for bead width and height; however, metallographic data points were sporadic in angle of repose while profilometry showed a consistent trend. Therefore, metallography may not be a robust method to measure bead geometry whereas optical profilometry is a much better technique.

- The (HAZ)_β showed highest hardness along the bead cross-section for which different explanations were suggested. First, higher oxygen content in the base metal and the subsequent diffusion of oxygen towards the molten pool may have resulted in high interstitial element concentrations compared to the added material. Second, fast cooling rates may have led to a finer microstructure than the base metal. Lastly, residual stresses in the HAZ may have led to an increase in hardness.

3.5 Acknowledgments

The authors would like to acknowledge the Office of Naval Research, under Contract No. N00014-11-1-0668. Any opinions, findings and conclusions or recommendations expressed in this publication are those of the authors and do not necessarily reflect the views of the Office of Naval Research. This material is based on research sponsored by Air Force Research Laboratory under agreement number FA8650-12-2-7230. The U.S. Government is authorized to reproduce and distribute reprints for Governmental purposes notwithstanding any copyright notation thereon. The views and conclusions contained herein are those of the authors and should not be interpreted as necessarily representing the official policies or endorsements, either expressed or implied, of Air Force Research Laboratory or the U.S. Government. Mr. Ed Good, Kyle Snider and Catherine Pomorski from the Pennsylvania State University Center for Innovative Material Processing Through Direct Digital Deposition (CIMP-3D) are thanked for his assistance in metallographic preparation and measurements. The authors also acknowledge the support of Tom McDonald and Optomec in the completion of this work.

Chapter 4: Ti-6Al-4V Patch Experiments

4.1 Introduction

Ti-6Al-4V is a widely used and key material in modern aerospace engines because of its high tensile and yield strength while minimizing weight compared to other structural materials (e.g., steel) [32]. Furthermore, Ti-6Al-4V's excellent corrosion resistance allows its use in the harsh chemical environments experienced during deep sea drilling operations, its biocompatibility allows use in biomedical applications requiring structural properties, it is common in consumer products (e.g., sporting goods and jewelry), and in engineering applications that require advanced mechanical properties. Ti-6Al-4V material is expensive to purchase and is also expensive to machine because of its high strength [33]. Therefore, it is necessary to develop a repair technique for returning high value components to service quickly.

Directed energy deposition (DED) is a novel material processing technique that utilizes a laser and powder feedstock to deposit material in 3-dimensions that is fused to a substrate. A laser is directed to a substrate and the beam heats the materials and creates a molten pool into which coaxial nozzles provide a continuous stream of metal powder into the molten pool. The added material is fully melted and solidifies to create a metallurgically bonded deposit on the substrate. Many of these individual depositions are executed adjacent to one another to create a layer; multiple stacked layers create a 3-dimensional component.

Ti-6Al-4V is a two phase alloy at room temperature composed of a hexagonal close-packed (HCP) α phase and a body centered cubic (BCC) β phase [33] whose

microstructure is known to depend on the cooling rate from the β transus [34], the temperature above which 100% β phase is present. Fast cooling rates ($\sim 8000^\circ\text{C/s}$) that were produced by water quench created a martensitic α' structure. In an experimental study on the temperature fluctuations during a DED experiment by Marshall and co-workers [77], cooling rates as high as $13,000^\circ\text{C/s}$ were noted in the first layers of the build using a laser power of 350 W and processing speed of 16.9 mm/s where temperature data was measured using a calibrated dual wavelength pyrometer and an infrared (IR) camera. Cooling rate decreased higher in the build because of increased heat build-up. Microstructure in the lower portions of the build was postulated to be initially martensitic α' that decomposed into Widmanstätten α and β because of thermal cycling from deposition of additional layers.

Multiple researchers have studied the microstructure in Ti-6Al-4V deposited by DED. A preliminary study of laser deposited Ti-6Al-4V powder on Ti-6Al-4V substrates by Kobryn and Semiatin [78] found large columnar prior β grains along the build direction that have been corroborated by other reports for a range of processing parameters [5], [35], [79]–[83]. Further, α lath features were visually coarser in high power CO_2 depositions relative to lower power Nd:YAG depositions. In a study on multi-layer builds by Kelly and Kampe [35] the α lath size width was a function of location in the deposit. Furthermore, the authors noted the formation of periodic layer bands that result in a visual perturbation in the macrostructure and exhibited a coarser α lath width relative to the other regions of the build. The layer bands were suggested to form because of thermal cycles where temperature increase from the deposition of additional layers resulted in a small area with a coarse microstructure.

In a study by Wu and co-workers [81] the resulting microstructure was shown to be affected by variable laser power (222 – 516 W), processing speed (3.3 – 16.7 mm/s), and powder feed rate (4 – 20 g/min). Prior β grain size increased under higher laser power, slower processing speed, and lower powder feed rates. The authors attribute this to changes in the number of nuclei for grain initiation; where higher laser power, slower processing speed, and lower feed rates result in fewer nuclei for grain nucleation and thereby, larger grains.

Paydas and co-workers [84] studied laser-deposited repair of a Ti-6Al-4V component and the effect of changing laser power (1100 W and 210 W) and path strategy had on the microstructure and hardness of the sample. The authors noted a basketweave α lath microstructure at the higher laser power that was visually finer for the sample processed with lower laser power. Moreover, the hardness in the cross-section was dependent on the thickness of the deposit. In multiple layer regions of the deposit a softer region (~330 HV) was observed relative to regions that did not experience as many thermal cycles (~360 HV). The authors suggest that this is from decomposition of martensitic α' to α and β from reheating, similar to what Marshall and co-workers noted [77]. In lower laser power builds, the microstructure was mainly martensitic throughout and not dependent on location in the repair. Hardness was typically greater than 375 HV showing an increase relative to the higher laser power sample. The authors noted no change in microstructure or hardness due to changing path strategy.

Carroll and co-workers [5] studied the tensile behavior of samples extracted from walls built by high laser power DED with laser power of 2 kW, processing speed of 10.6 mm/s, and beam diameter of 4 mm. Strength values were commensurate to wrought

material; however, variability in the measurements were higher in deposited material and was attributed to the additive process. The authors noted significantly higher ductility (11-14%) relative to efforts by previous researchers [79], which was attributed to comparatively low amounts of porosity. Ductility was anisotropic, and the authors noted a continuous α phase on the columnar grain boundaries that they hypothesized underwent accelerated damage accumulation in samples pulled perpendicular to the building direction.

While the microstructure and mechanical properties of builds produced by laser-based additive manufacturing have been reported, the variables studied are mainly limited to laser power, processing speed, and path strategy. The current investigation expands upon these studies by investigating the effect of initial substrate temperature, interlayer dwell time (IDT), substrate thickness, hatch pattern, and number of layers deposited on the process-structure-property relationships including the microstructure, porosity, and microhardness. Furthermore, the hardness in the deposited region is compared to that of the heat affected zone (HAZ) in the substrate, which should not be neglected along with porosity and depth of HAZ as these are metrics to judge the repair quality. Lastly, the current study utilizes a two-dimensional approach for porosity measurements, which is compared to volumetric X-Ray Computer Tomography (CT) data.

4.2 Experimental

Experiments were conducted on a commercial Optomec LENS[®] MR-7 directed energy deposition (DED) machine that was equipped with an IPG Photonics Yb-doped fiber laser capable of achieving a power of 500 W. A laser power of 300 W and a processing speed of 10.6 mm/s was used for all builds in the current investigation. The

D4 σ width of the laser was experimentally measured to be 990 μm at the substrate. The laser processing head consisted of four copper powder feeding nozzles with orifice diameter of 1.19 mm that delivered material at a rate of 2 g/min. Argon gas was flowed through the nozzles at 4 lpm and coaxially at 30 lpm to protect the laser focusing lens. The chamber was purged with argon prior to deposition and processing only commenced when the oxygen concentration was less than 20 ppm.

Patches were deposited on 7.6 cm by 5.1 cm Ti-6Al-4V mill-annealed substrates (ASTM B265 [85], Performance Titanium Group) with two different substrate thicknesses (0.25 and 1.3 cm) and a chemical composition shown in Table 4.1. Prior to deposition, the substrates were glass bead blasted using media size number 13 and cleaned with acetone to remove oil and other contaminants. Prealloyed Ti-6Al-4V powder (TIMET[®]) was made using the plasma rotating electrode process (PREP) and the chemical composition is shown in Table 4.1. The powder was sieved using -100/+325 meshes corresponding to a particle size range of 44-150 μm .

A heating apparatus was used to preheat substrates from the top surface prior to deposition. For all preheated experiments, the heating apparatus was removed and deposition commenced when a removable thermocouple at the center of the substrate read a temperature of 400°C. A schematic of this setup is shown in Figure 4.1.

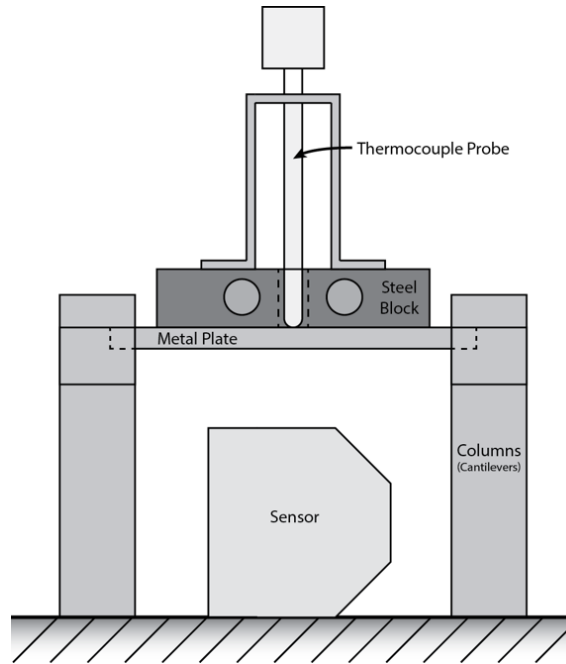


Figure 4.1. Schematic of heating apparatus placement in the current study.

Table 4.1. Substrate and powder chemical compositions in weight percent.

	Ti	Al	V	Fe	C	N	O	H
Substrate	Balance	6.37	4.00	0.21	0.01	<0.01	0.19	<0.01
Powder	Balance	6.23	3.80	0.16	0.04	<0.01	0.18	<0.01

In these experiments, 2.5 cm by 2.5 cm square builds of various thicknesses were deposited under varying processing conditions. Thirty-six hatches were deposited to complete one layer with a hatch spacing of 0.71 mm. After the completion of one layer, the laser head stepped up by 0.25 mm to deposit the next layer. The same hatch spacing and incremental layer height were used in all 28 depositions.

In total, five parameters were varied resulting in 28 distinct “runs” as shown in Table 4.2. The five parameters are: initial substrate temperature, IDT, substrate thickness, hatch pattern, and number of layers. Initial substrate temperature refers to the substrate temperature prior to deposition as measured at the center of the top surface.

IDT is the time delay after the completion of one layer prior to start of processing on the

next layer. Substrate thickness is the thickness of substrate used for deposition. Hatch pattern is the path strategy in the deposition. The two hatch patterns, parallel and cross, used in the current study are shown in Figure 4.2. Number of layers are the number of layers deposited. Each run refers to an individual patch build that was completed.

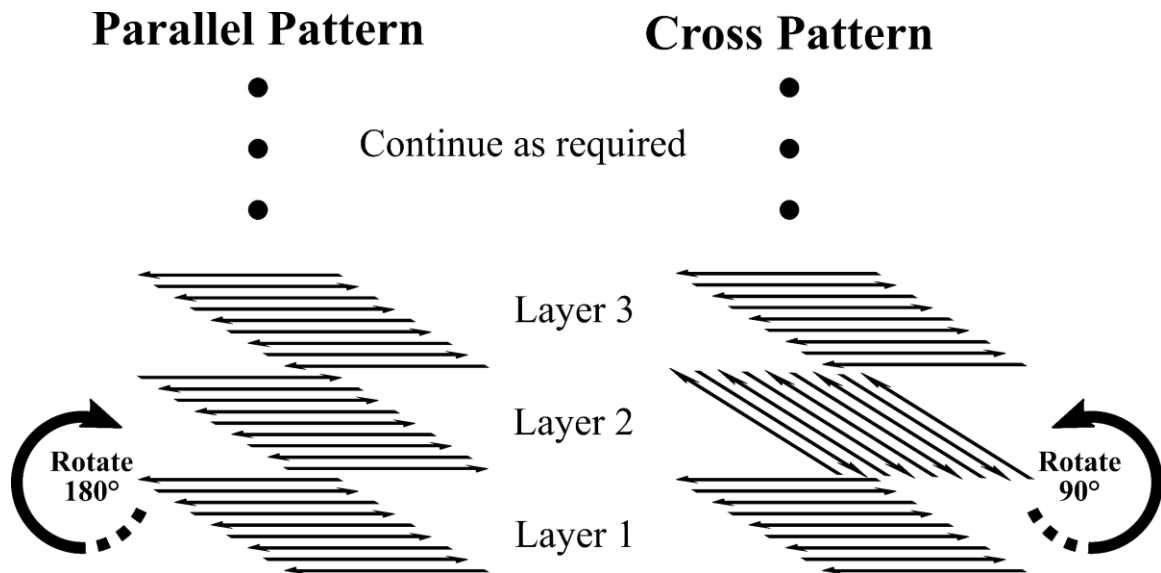


Figure 4.2. Hatch patterns used in the current study.

Table 4.2. Parameter sets used in the current study.

Run	Initial Substrate Temperature [°C]	Interlayer Dwell Time [s]	Substrate Thickness [mm]	Hatch Pattern	Number of Layers
1	0	25	2.5	Parallel	3
2	40	25	2.5	Parallel	3
3	0	400	2.5	Parallel	3
4	40	400	2.5	Parallel	3
5	0	25	12.7	Parallel	3
6	40	25	12.7	Parallel	3
7	0	400	12.7	Parallel	3
8	40	400	12.7	Parallel	3
9	0	25	2.5	Cross	3
10	40	25	2.5	Cross	3
11	0	25	12.7	Cross	3
12	40	25	12.7	Cross	3
13	0	400	12.7	Cross	3
14	40	400	12.7	Cross	3
15	0	25	2.5	Parallel	10
16	40	25	2.5	Parallel	10
17	0	400	2.5	Parallel	10
18	40	400	2.5	Parallel	10
19	0	25	12.7	Parallel	10
20	40	25	12.7	Parallel	10
21	0	400	12.7	Parallel	10
22	40	400	12.7	Parallel	10
23	0	25	2.5	Cross	10
24	40	25	2.5	Cross	10
25	0	25	12.7	Cross	10
26	40	25	12.7	Cross	10
27	0	400	12.7	Cross	10
28	40	400	12.7	Cross	10

For characterization, samples were cut using a silicon carbide cut-off wheel approximately 1.91 cm from the laser start point and mounted to obtain a cross-sectional view. Standard metallographic preparation techniques were used to grind and polish the sample. Following grinding, polishing was completed using a 0.06 μm colloidal silica solution. Samples were etched using Kroll's reagent [66].

Optical macrographs of the entire cross-section in both unetched and etched conditions were taken using a Keyence VHX-2000 outfitted with a VH-Z20R High-performance zoom lens. Unetched macrographs were used to identify porosity by applying the default threshold method in ImageJ image processing software until porosity was black and surrounding dense material was white as shown in Figure 4.3. Next, the deposit region of the image was analyzed in ImageJ to determine conglomerates of black pixels that exceeded an area $250 \mu\text{m}^2$. This lower bound was selected to remove background noise generated in the thresholding process; however, porosity smaller the lower bound will not be resolved. The percent density of the deposit was determined by taking the overall pore area divided by the total deposited area.

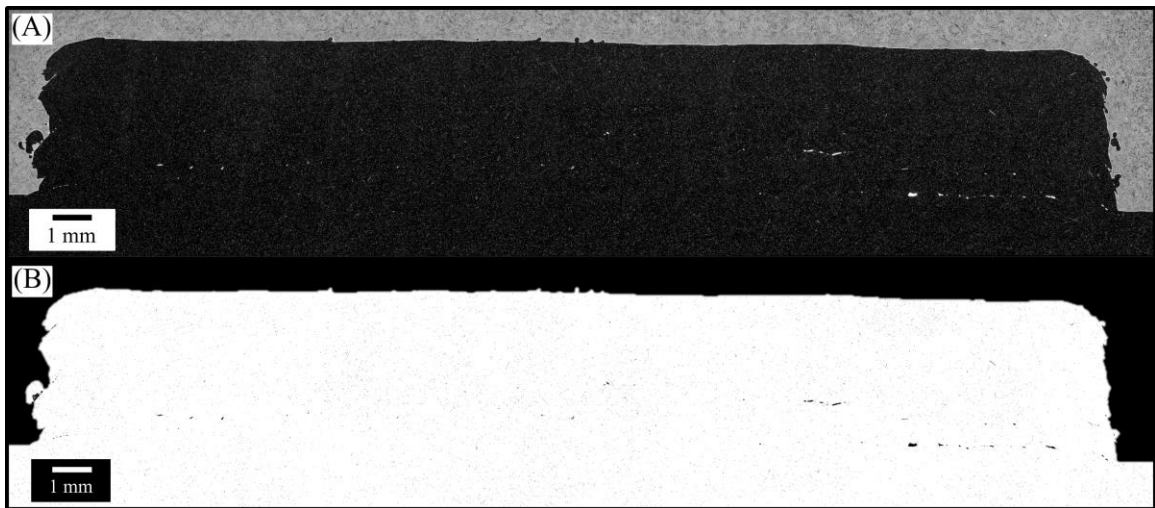


Figure 4.3. (A) Raw and (B) thresholded cross-sectional image to show lack-of-fusion porosity (black spots in deposit).

Validation of metallographically measured porosity was performed using X-Ray Computed Tomography (CT) on a GE phoenix v|tome|x m 300 machine using a voltage of 270 kV and a current of 120 μ A. A 0.2 mm copper filter was used and a voxel size of 32.4 μ m was obtained. Porosity analysis was completed using the VGDefX (version 2.2) algorithm in the VGStudio Max (version 2.2) software. A lower bound of 3 voxels (97.2 μ m) was selected in X-Ray CT porosity analysis.

For comparison, two samples (Run 10 and Run 23) were cross-sectioned and porosity was observed using the metallographic approach. The opposite halves that were not used for metallography were observed by CT. Metallographic measurements were found to be within 0.02% of X-Ray CT assessments.

Microhardness was performed using a Vickers indenter (LECO M-400-G1) with an applied load of 300 g and dwell time of 10 seconds at locations specified in Figure 4.11, Figure 4.12, and Figure 4.13. Uncertainty in these measurements were ± 5 HV.

4.3 Results and Discussion

4.3.1 Microstructure and Heat Affected Zone

The macrostructure of a 10-layer deposit on a room temperature thin substrate, a 0s IDT, and with a parallel hatch pattern is shown in Figure 4.4. As is characteristic of laser deposited Ti-6Al-4V [86], large prior β grains are present along the build direction of the deposit because of high thermal gradients associated with laser-based deposition. Furthermore, prior β grains grew across multiple deposited layers showing nucleation from the previously deposited layer as has been identified in previous research efforts [14], [35], [86].

The HAZ is shown propagating into the base material in Figure 4.4. The HAZ clearly consists of two regimes ($(HAZ)_{\alpha+\beta}$ and $(HAZ)_{\beta}$) shown in a macrograph of a single bead deposit in Figure 4.5. The $(HAZ)_{\beta}$ region corresponds to the area that was heated to temperatures greater than the β transus (980°C for Ti-6Al-4V [33]). The $(HAZ)_{\alpha+\beta}$ depth exceeds the $(HAZ)_{\beta}$ region and did not exceed the β transus during processing, but temperatures were high enough to cause α lath coarsening resulting in the visual microstructural difference.

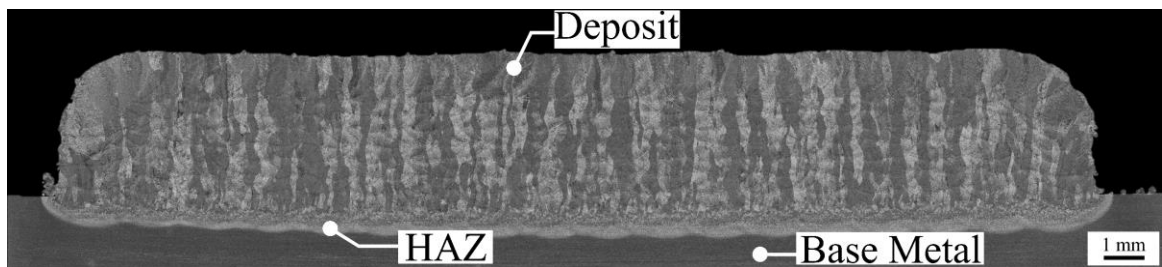


Figure 4.4. Macrostructure of 10-layer, 0s IDT, 25°C , 2.5 mm substrate thickness, parallel hatch pattern build (Run 15).

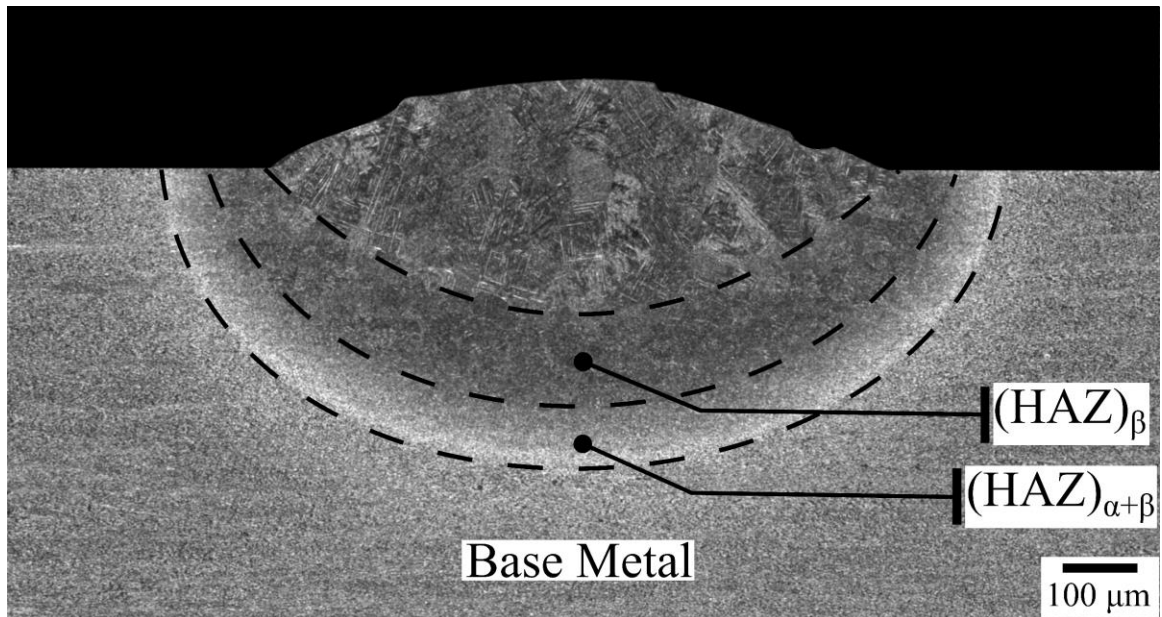


Figure 4.5. Cross-section of a single bead-on-plate using the same laser power and processing speed (300 W, 10.6 mm/s) as the patch deposits with key features labeled.

The maximum metallographically measured $\text{HAZ}_{\alpha+\beta}$ for each of the 28 different testing conditions are shown in Figure 4.6 and Figure 4.7 for room temperature and preheated substrates respectively. The depth of the $(\text{HAZ})_{\alpha+\beta}$ for a single bead is represented by the horizontal black dotted line.

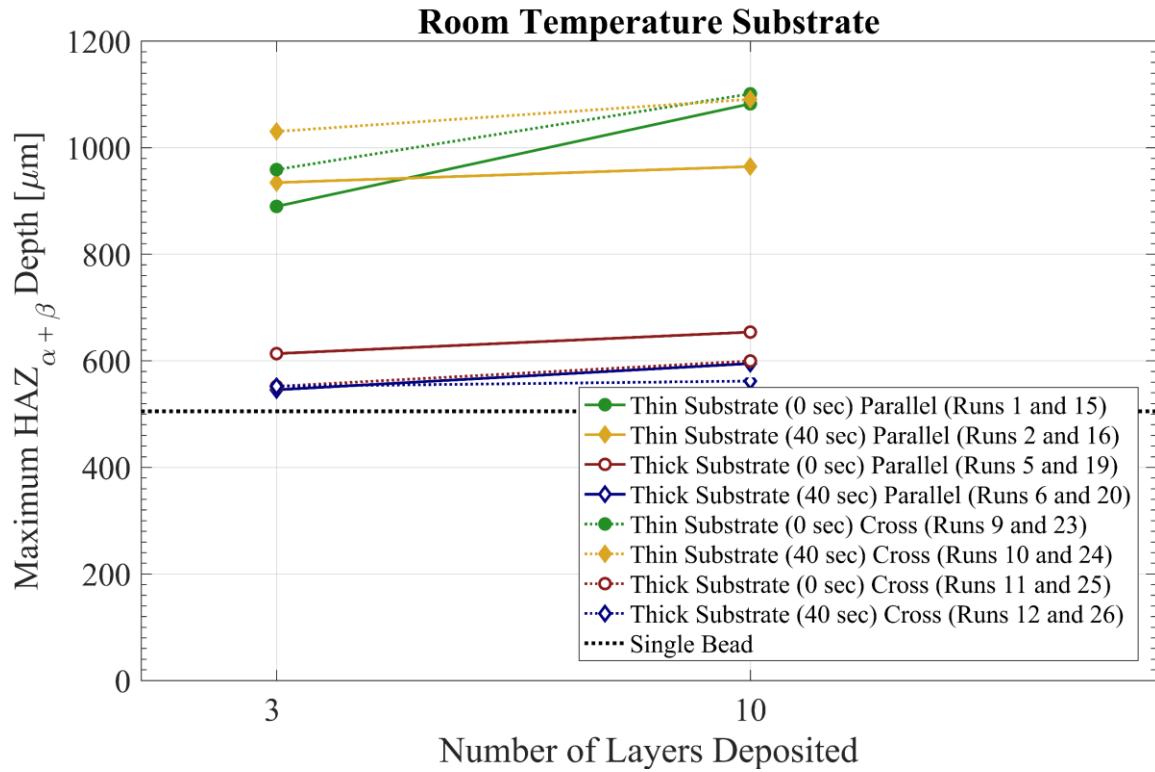


Figure 4.6. Maximum $(\text{HAZ})_{\alpha+\beta}$ depth measured from the substrate surface for all room temperature patch builds. Dashed line denote the $(\text{HAZ})_{\alpha+\beta}$ depth of the single bead-on-plate.

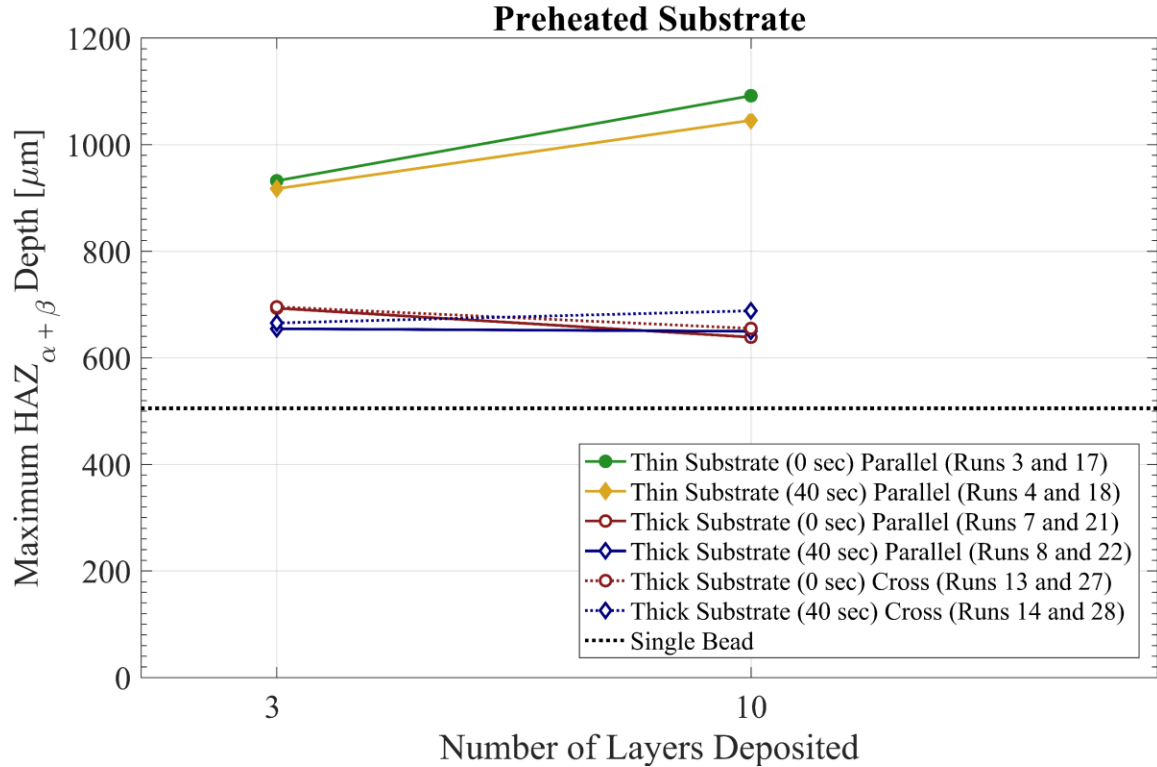


Figure 4.7. Maximum $(HAZ)_{\alpha+\beta}$ depth measured from the substrate surface for all preheated patch builds. Dashed line denote the $(HAZ)_{\alpha+\beta}$ depth of the single bead-on-plate.

All patch builds in Figure 4.6 and Figure 4.7 show a larger $(HAZ)_{\alpha+\beta}$ region relative to the single bead-on-plate measurement. This is the region exposed to high temperatures (lower than β transus) that created a microstructural change. As multiple beads were placed next to one another, heat built up in the sample, and resulted in a larger $(HAZ)_{\alpha+\beta}$ depth relative to single bead-on-plate experiments.

The $(HAZ)_{\alpha+\beta}$ depth in all thin substrate cases is larger than thick substrate cases. A more efficient heat sink was obtained in thicker material relative to thin substrates. The change in conduction resulted in a smaller region for heat accumulation creating a smaller HAZ. In thin substrates, heat was not as efficiently removed from the region near the deposit creating a larger $(HAZ)_{\alpha+\beta}$ region.

The $(HAZ)_{\alpha+\beta}$ depth increased in thick, preheated substrate cases relative to thick, room temperature substrate cases; however, this result is not conserved for thin substrates. A preheat created higher temperatures among all depths of the substrate. Therefore, in preheated cases heat was not extracted as quickly, thereby more heat was accumulated and the $(HAZ)_{\alpha+\beta}$ depth was larger relative to room temperature substrates.

4.3.2 Porosity

Porosity measurements are presented here as percent dense, which is the total, cumulative area of resolved porosity in the deposit region divided by the total cross-sectional area of the deposit. Percent dense values for all testing conditions are shown in Figure 4.8 and Figure 4.9 for room temperature and preheated initial substrate temperatures, respectively. All samples in the current study show density greater than 99.7% dense using the optical microscopy thresholding method.

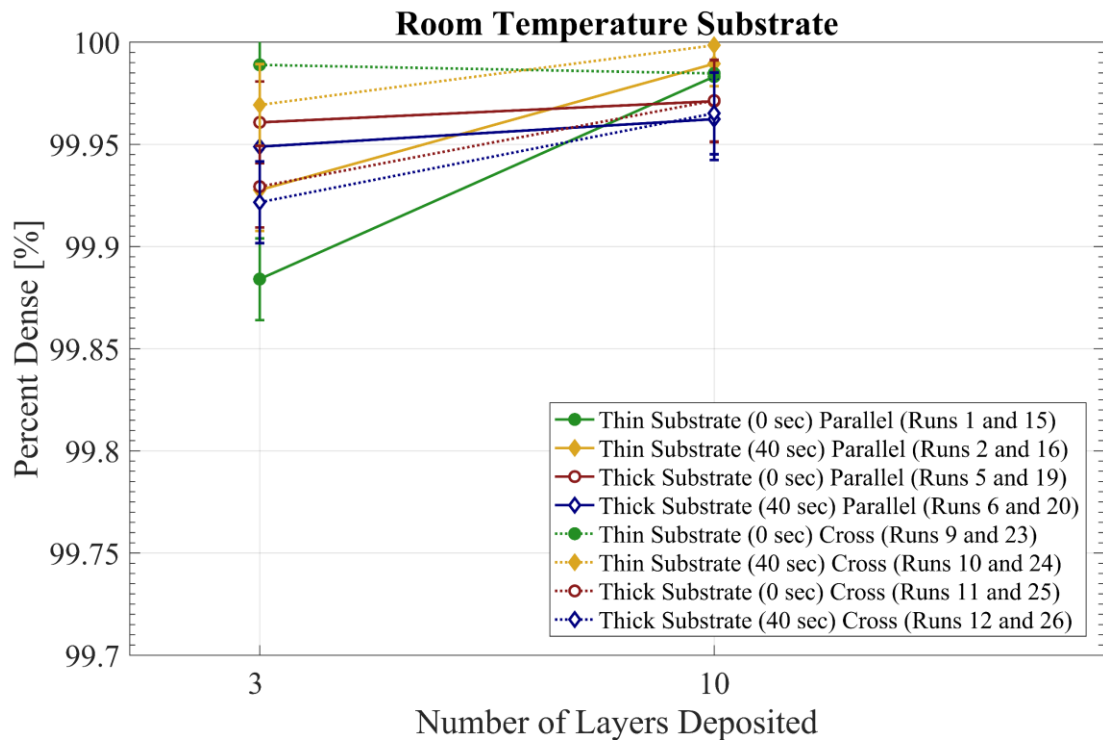


Figure 4.8. Overall density measurements for room temperature substrate samples in the current study. Symbol shape denotes IDT, line style denotes hatch pattern used and symbol face denotes substrate thickness.

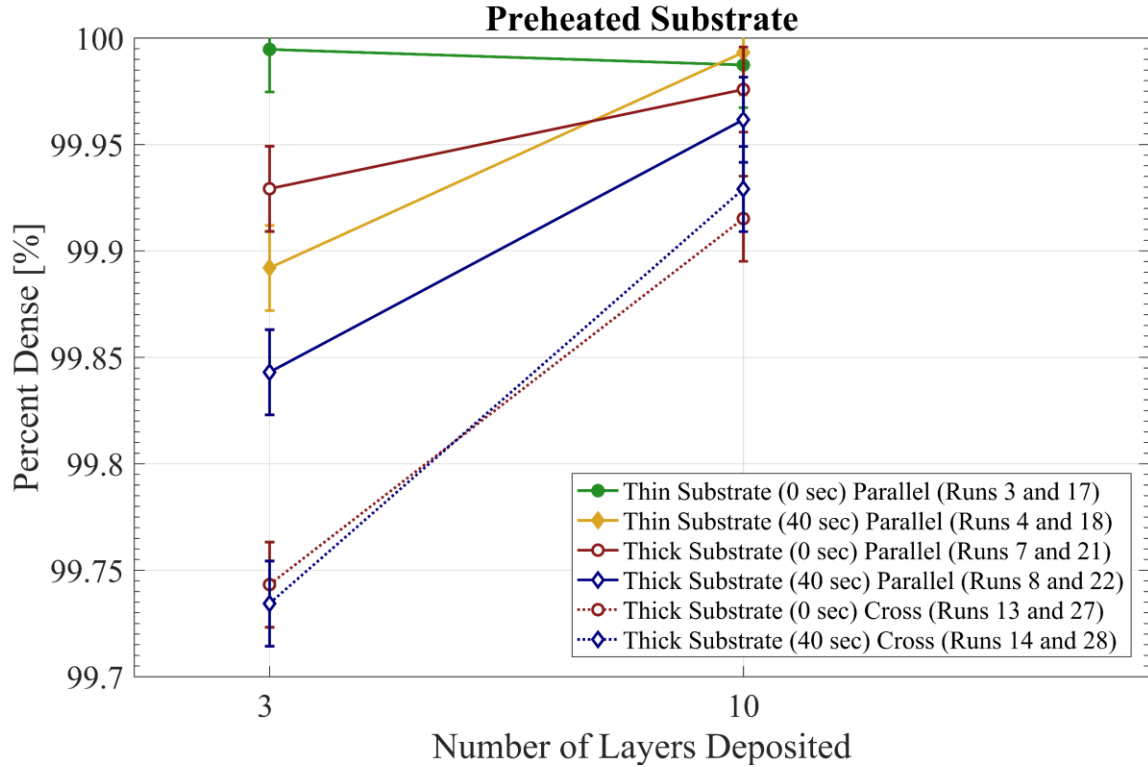


Figure 4.9. Overall density measurements for preheated substrate samples in the current study. Symbol shape denotes IDT, line style denotes hatch pattern used and symbol face denotes substrate thickness.

Room temperature samples consistently had higher density relative to preheated substrate samples. Porosity in DED is explicitly linked to optimization of inputted processing parameters (e.g., laser power, spot size, travel speed, hatch spacing, layer height, etc.) based on the dimensions of a single bead. Hatch spacing and layer height were consistent among all builds; however, bead geometry (width and height) changed from substrate preheat [87] resulting in non-optimal machine inputs and an unexpected increase in porosity.

There is a higher density in the 10-layer high deposits relative to 3-layer deposits as shown in Figure 4.8 and Figure 4.9. A gradient in porosity is observed in all patches, in which the porosity is concentrated near the bottom of the patch, and the top of the patch is dense, as shown in Figure 4.3. The porosity gradient is likely due to faster

cooling rates near the substrate, and as the temperature of the deposition rises, the melt pool becomes more fluid and less energy is needed to melt the powder and previous deposited layer. Therefore, the overall porosity decreased in 10-layer builds despite porosity being the same in the bottom region of the deposit. This point is reinforced by Figure 4.10 that shows a higher percent dense value in a 10-layer build (Run 25) despite more observed porosity relative to a 3-layer build under the same processing conditions (Run 11).

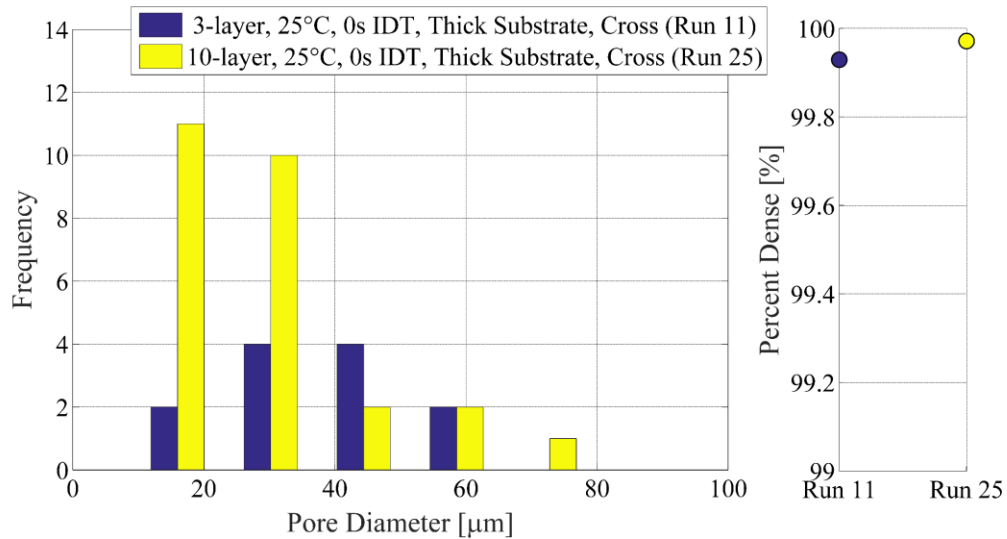


Figure 4.10. Histogram relating observed porosity in 0s IDT, room temperature initial substrate temperature, 12.7 mm substrate thickness, cross hatch pattern, and 3 deposited layers (Run 11) and 0s IDT, room temperature initial substrate temperature, 12.7 mm substrate thickness, cross hatch pattern, and 10 deposited layers (Run 25).

4.3.3 Hardness

Hardness indents for selected samples are shown in Figure 4.11 and Figure 4.12. The samples selected were exposed to extremes in cooling rates. Figure 4.11 shows longitudinal hardness taken approximately halfway up the height of the cross-section going across the width of the deposit region in a room temperature substrate with a 40s IDT (Run 2) and a preheated substrate with a 0s IDT (Run 3). Hardness traverses taken vertically along the deposit are shown in Figure 4.12 for Run 2, Run 3, and a 10-layer, room temperature, 40s IDT, parallel hatch pattern deposit on a thin substrate (Run 16). The average and standard deviation hardness in the substrate material is shown by the orange solid and dotted lines. The average and standard deviation hardness of a single deposited bead is denoted by the black solid and dashed lines in Figure 4.12.

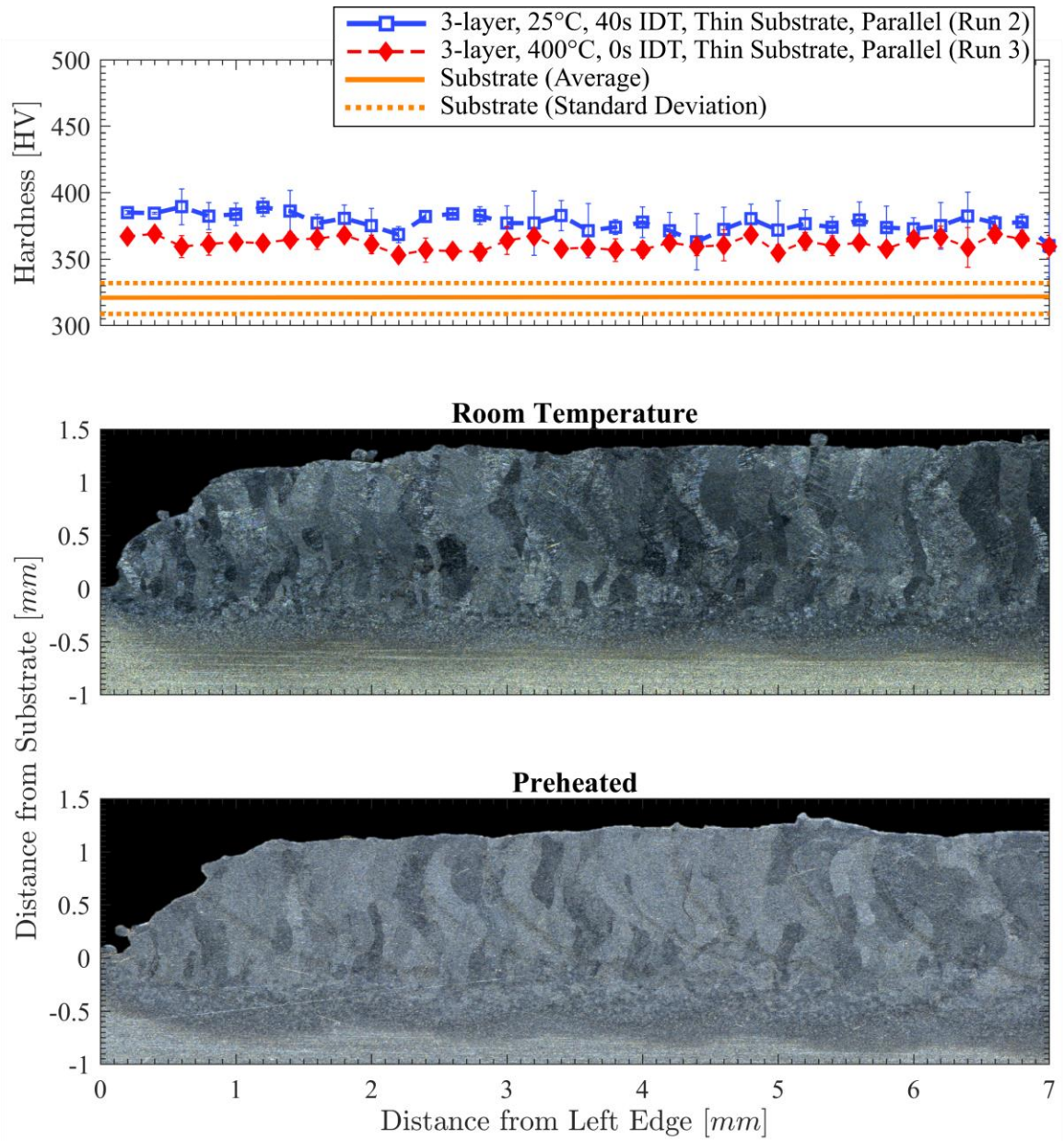


Figure 4.11. Horizontal hardness traverses in 3-layer deposit, 25°C, 40s IDT, thin substrate, parallel hatch pattern (Run 2) and 3-layer deposit, 400°C, 0s IDT, thin substrate, parallel hatch pattern (Run 3).

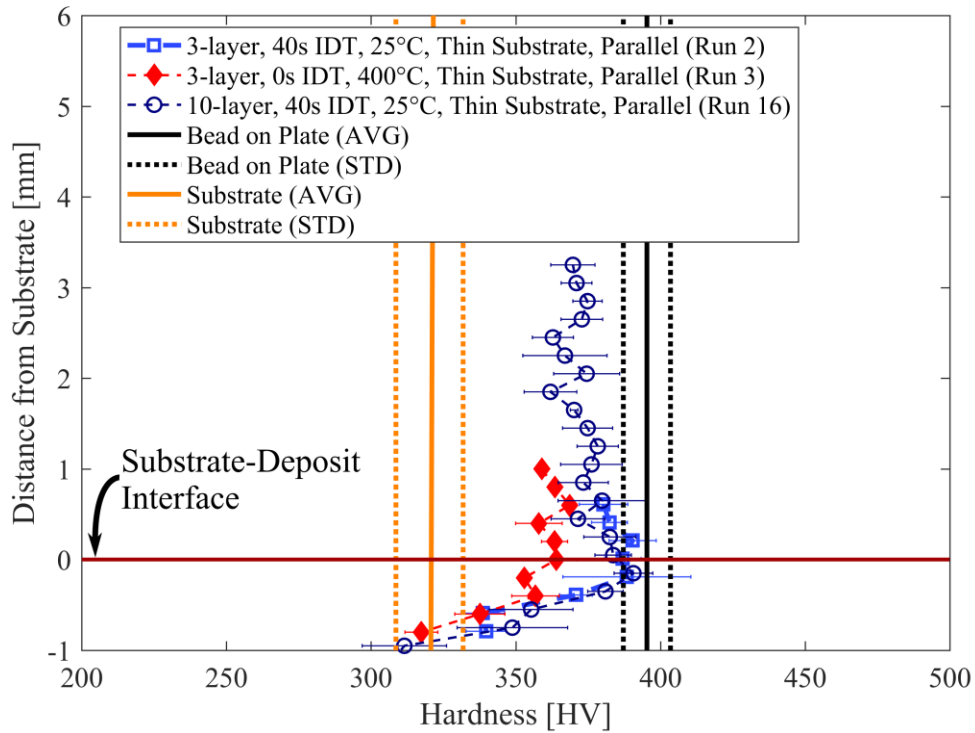


Figure 4.12. Vertical hardness traverses in runs 3-layer deposit, 25°C, 40s IDT, thin substrate, thin substrate, parallel hatch pattern (Run 2), 3-layer deposit, 400°C, 0s IDT, thin substrate, parallel hatch pattern (Run 3) and 10-layer deposit, 25°C, 40s IDT, thick substrate, parallel hatch pattern (Run 20). Dashed line denotes hardness of single bead.

Little deviation was seen in hardness going across the width of the deposit as shown in Figure 4.11 along with the accompanying macrographs of the deposits where hardness indents were taken. A gradient in hardness from the edge to interior of the patch is not seen.

The hardness in room temperature substrate deposits is consistently higher than preheated substrate cases in both horizontal and vertical hardness traverses in the deposited region as shown in Figure 4.11 and Figure 4.12 and showed statistical significance in the deposit hardness with a p-value of 0.0287 (two-sample t-test, 95% confidence interval) shown in Table 4.3. The hardness indents taken into account for statistical analysis are shown in Figure 4.13. Smaller thermal gradients in preheated

substrates resulted in slower cooling rates creating a coarser microstructure and softer deposited region. This explanation is consistent with simulation results from Zhao and co-workers [88] that showed lower thermal gradients higher in the build from increased heat build-up.

Table 4.3. Statistical results of relative influence of different variables on hardness variations in the FZ of current data from a two sample T-Test where a p-value less than 0.05 shows a statistically significant influence.

Variable	P-Value (All)	P-Value (Only Room Temperature)	P-Value (Only Preheated)
Number of Layers	0.159	0.146	0.572
Dwell Time	0.053	0.130	0.168
Hatch Pattern	0.244	0.369	0.816
Substrate Thickness	0.781	0.250	0.716
Substrate Temperature	0.029	-	-

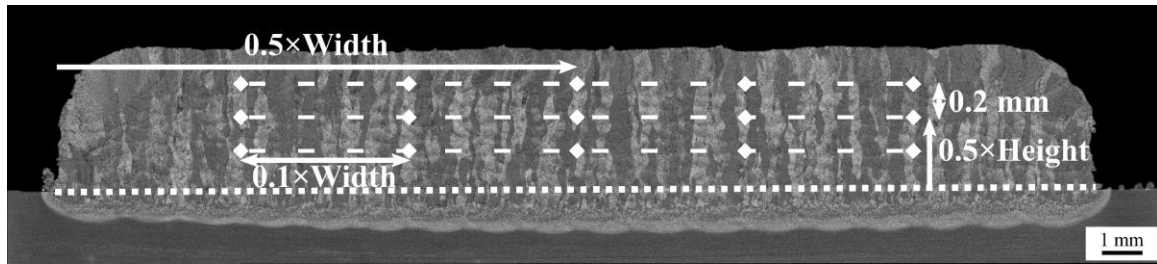


Figure 4.13. Location of hardness indents in all patch samples in the current study overlaid on 10-layer deposit, 25°C, 0s IDT, thin substrate, and parallel hatch pattern deposit (Run 15).

Hardness traverses going vertically down a 10-layer room temperature deposit with a 40s IDT (Run 20), a 3-layer room temperature deposit with a 40s IDT (Run 2), and a 3-layer preheated substrate with a 0s IDT (Run 3) are shown in Figure 4.12.

In the 3-layer deposits, hardness remains consistent along the height where the hardness only deviates by ± 10 HV. In the 10-layer deposit high hardness is seen near the surface of the substrate (fast cooling rates) and settles into a steady-state higher in the deposit (~ 1 mm). Furthermore, two-sample t-test results in Table 4.3 show a p-value of 0.1590 meaning the difference in average hardness between 3-layer and 10-layer deposits was not statistically significant. This is a different result from that reported by Nassar and co-workers [89] who found a statistically significant hardness gradient along the height of DED produced Ti-6Al-4V builds with hardest material at the top. The authors attributed this to thermal cycling from the laser-deposition process. In that study they used a higher laser power (450W) and deposited more layers (25) in a thin wall geometry which is different than the current patch geometry. Therefore, the difference in hardness trends may be because the present patch deposits heat up enough in the first 2-3 layers to achieve a relative steady-state cooling rate and thus a steady-state hardness. The time for achieving steady state may vary greatly with deposition geometry and other processing conditions resulting in changes to observed trends between Nassar et al. and the present study.

The hardness in the bottom three layers of the 10-layer room temperature deposit is analogous to that in the 3-layer room temperature deposit as hardness indents in the last three layers of the 10-layer patch overlapped with the hardness in the 3-layer build.

Therefore, hardness in the initial three layers was not affected by deposition of additional layers.

As shown previously, the hardness in the deposit region does not change with respect to location in the 3-layer builds and reaches a steady state after the first 2-3 layers in the 10-layer build. Therefore, the hardness of each of the 28 runs is taken to be an average of 15 indents at the locations specified by Figure 4.13 with all measurements taken about the third layer in the 10-layer builds. These measurements are shown in Figure 4.14 and Figure 4.15 for room temperature and preheated substrates, respectively. Solid and dotted black lines show the average and standard deviation hardness in the fusion zone of a single bead on a room temperature substrate. This was the highest cooling rate obtained in the current study and was not subjected to thermal cycles. Solid and dotted orange lines show the average and standard deviation hardness of the unaffected mill-annealed substrate.

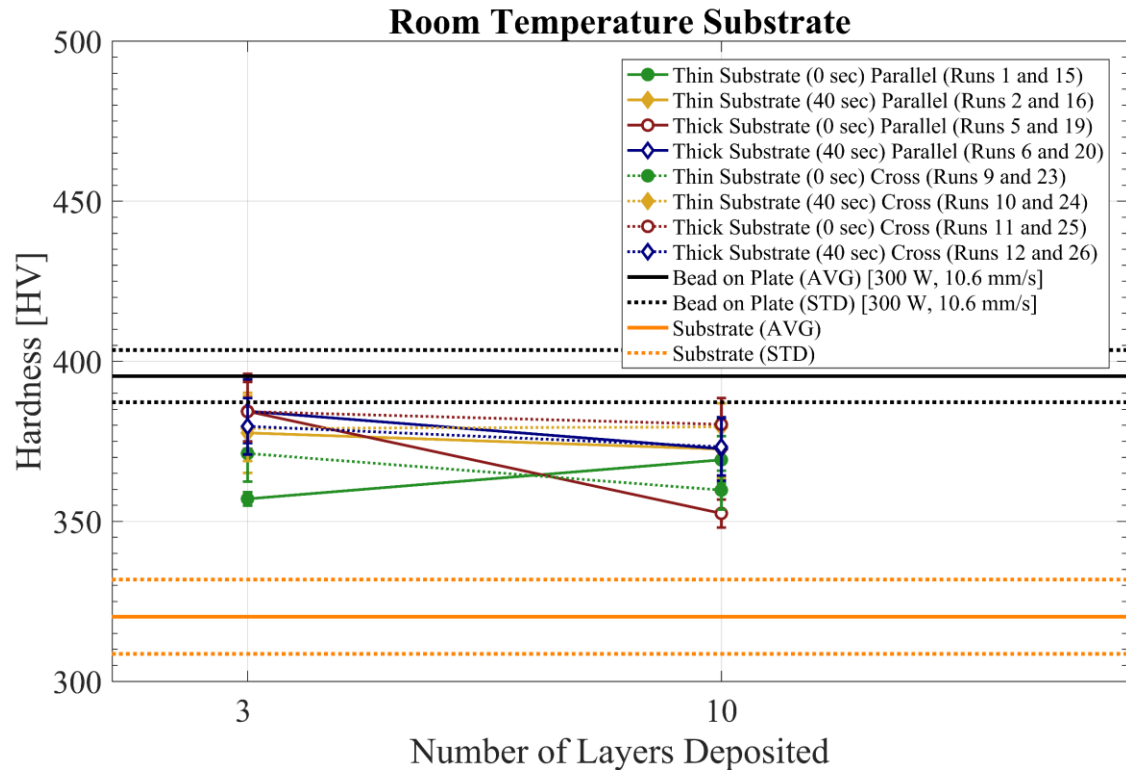


Figure 4.14. Average deposit hardness of room temperature substrate cases. Black horizontal lines denote the hardness and standard deviation of a single bead while orange horizontal lines denote the hardness and standard deviation of the substrate material.

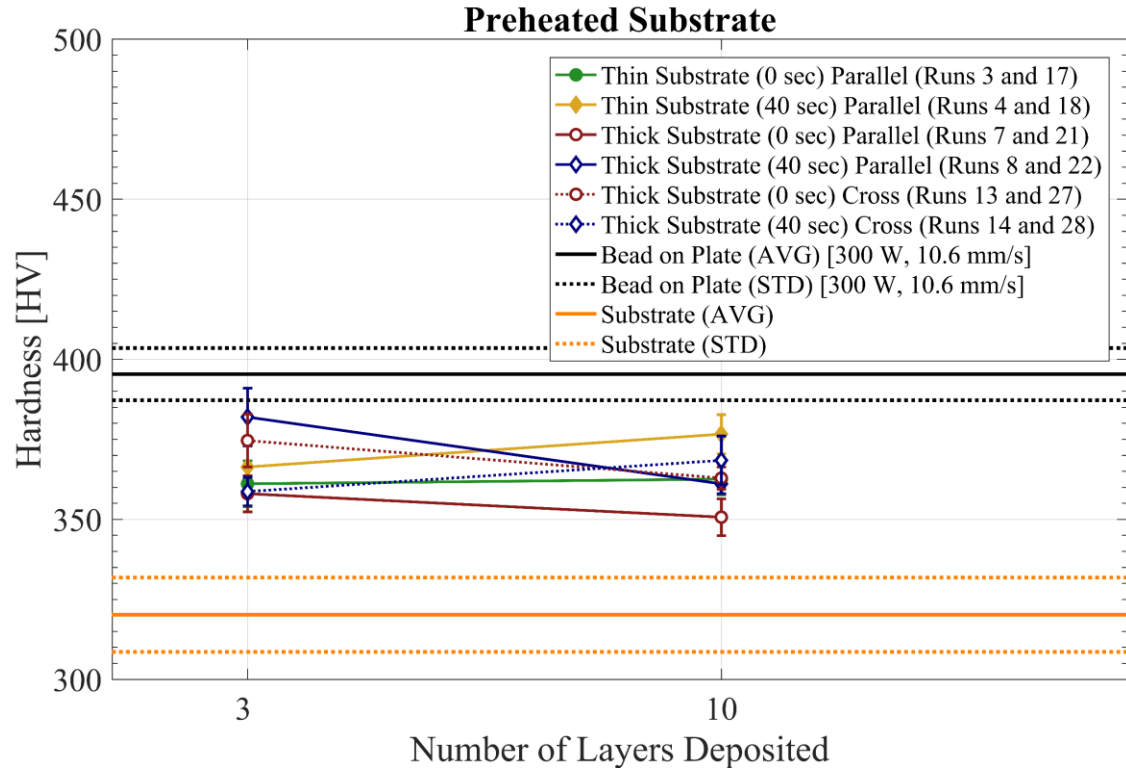


Figure 4.15. Average deposit hardness of preheated substrate cases. Black horizontal lines denote the hardness and standard deviation of a single bead while orange horizontal lines denote the hardness and standard deviation of the substrate material.

As shown in Figure 4.14 and Figure 4.15, all samples in the current study have a hardness between that of the mill-annealed substrate and single deposited bead. The single deposited bead was exposed to the maximum cooling rate and shows the highest hardness. Although patches consist of many beads, the addition of adjacent beads and layers resulted in heat accumulation in the deposit and substrate resulting in a less efficient heat sink. As shown in the previous comparison between room temperature and preheated substrates; higher temperatures result in slower cooling rates and a softer deposited material. The mill-annealed substrate is expected to be softer than the deposited material that experienced rapid cooling.

Although not less than the 0.05 p-value cutoff, IDT (p-value: 0.0527) shows trend in the deposited region hardness where a 40s IDT has higher hardness relative to 0s IDT

cases. The explanation towards this is similar to that stated prior where the 40s IDT allows time for the previously deposited layer to cool. Then the subsequently deposited layer may have higher cooling rates because the cooler material below acts as a larger heat sink relative to 0s IDT cases. Moreover, more heat accumulation may occur in the 0s IDT case creating lower cooling rates as more layers were deposited. A longer IDT (e.g., 60s) may create a statistically significant result ($p\text{-value} < 0.05$) in deposited region hardness.

The remaining processing parameters, hatch pattern ($p\text{-value}$: 0.2441) and substrate thickness ($p\text{-value}$: 0.7805), did not show significant correlation with hardness. In order to investigate further, these variables were statistically analyzed between room temperature and preheated substrate cases (only variable that caused significant change) to determine if a change is noted in room temperature or preheated cases and are presented in Table 4.3. However, hardness differences in these variables are not significant in either initial substrate temperature condition. These processing parameters may result in negligible changes to cooling rate relative to initial substrate temperature and IDT. The difference in hardness between a slow cool (annealed substrate) and a fast cool (single bead) are within 100 HV so it may be difficult to identify differences in hardness from these processing parameters.

4.4 Summary and Conclusions

The current study used an AM powder-fed DED approach to deposit square patches under different process conditions to simulate various conditions of a component repair. These patches were analyzed to identify changes to microstructure, porosity, and hardness due to different heat sinking conditions, and to determine the relative sensitivity

of repair quality (e.g., porosity, hardness, etc.) to variations in each. The variables studied were interlayer dwell time (time between deposition of layers), initial substrate temperature, substrate thickness, hatch pattern (deposition strategy) and number of layers deposited. The following are the key conclusions:

- The depth of HAZ was most dependent on substrate thickness (Thin Substrates: $\sim 1000\ \mu\text{m}$, Thick Substrates: $\sim 600\ \mu\text{m}$). Thick substrates allowed for rapid extraction of heat from the deposit region forming a smaller HAZ relative to thin substrates.
- Although low amounts of porosity are found (all samples greater than 99.7% dense), porosity was concentrated near the substrate surface resulting in a relatively lower overall density for samples composed of more layers. Furthermore, density was higher for room temperature initial substrate conditions relative to preheated cases, which may be the result of bead dimension change from preheating resulting in non-optimal processing parameters because of less energy required to fully melt, thereby increasing melt pool temperatures and melt fluidity.
- Independent to processing parameters, hardness in the deposit region was higher than the substrate (320 HV) but lower than a single deposited bead (395 HV). Further, hardness was constant through the deposited region (i.e., no edge or height effects).
- Statistical analysis showed hardness in the deposit region was significantly affected by the initial substrate temperature (p-value: 0.03). Interlayer dwell time (p-value: 0.05) was the next impactful processing condition to deposit

hardness. Substrate thickness (p-value: 0.78), number of layers deposited (p-value: 0.16), and hatch pattern (p-value: 0.24) did not have a large statistical significance.

4.5 Acknowledgements

The authors would like to acknowledge the Office of Naval Research, under Contract No. N00014-11-1-0668. Any opinions, findings and conclusions or recommendations expressed in this publication are those of the authors and do not necessarily reflect the views of the Office of Naval Research. This material is based on research sponsored by Air Force Research Laboratory under agreement number FA8650-12-2-7230. The U.S. Government is authorized to reproduce and distribute reprints for Governmental purposes notwithstanding any copyright notation thereon. The views and conclusions contained herein are those of the authors and should not be interpreted as necessarily representing the official policies or endorsements, either expressed or implied, of Air Force Research Laboratory or the U.S. Government. Mr. Ed Good and Patrick Illig from the Pennsylvania State University Center for Innovative Material Processing Through Direct Digital Deposition (CIMP-3D) are thanked for his assistance in metallographic preparation and measurements. The authors also acknowledge the support of Tom McDonald and Optomec in the completion of this work.

Chapter 5: Conclusions and Future Work

This thesis contributes to the evolving field of additive manufacturing especially in regards to experimental data of DED processing parameter influence on both single bead deposits and full builds. This understanding is critical if the Department of Defense is to correctly apply DED AM technology to repair and refurbishment of worn, corroded, and damaged components in an aging fleet. The macrostructure in single bead IN718 deposits showed a change in fusion zone morphology with laser power, processing speed, and working distance. Furthermore, single bead deposits of Ti-6Al-4V showed correlation with bead geometry (i.e., width, height, and angle of repose). However, in either case (i.e., IN718 or Ti-6Al-4V) fusion zone hardness was not dependent on the inputted processing parameters for the ranges studied. The Ti-6Al-4V single bead data was used to identify optimal processing parameters (i.e., hatch spacing and layer height) to build square patches and understand the effect of various repair conditions (i.e., initial substrate temperature, interlayer dwell time, number of deposited layers, substrate thickness, and hatch pattern) on the heat affected zone, porosity, and hardness. Substrate thickness had the largest effect on heat affected zone depth and initial substrate temperature had the largest effect on porosity and hardness. Moreover, interlayer dwell time showed correlation with hardness; however, this was secondary compared to the effect by initial substrate temperature.

Additional future work that would bring more understanding of the effect of directed energy deposition processing parameters on the end result includes the following:

- In the current study, IN718 bead-on-plate (Chapter 2) studied the effect of substrate preheat and working distance that was not covered in Ti-6Al-4V bead-on-plate (Chapter 3) experiments. Therefore, additional Ti-6Al-4V bead-on-plate experiments should be done to match the experiments completed on IN718. Furthermore, other processing parameters can be varied as well (e.g., powder feed rate, beam diameter, coaxial and powder gas flow rates, etc.) to increase understanding of the process.
- Computational simulations on fluid flow and thermal state can be compared to experimental results for both alloying systems to more thoroughly understand the physical mechanism for changing fusion morphology and generate a predictive tool for use with other laser powers, processing speeds, and working distances.
- Quantitative analysis of α lath width in both bead-on-plate and patch Ti-6Al-4V experiments will generate a quantitative and more thorough link between microstructure and mechanical properties.
- In order to advance from non-structure to structural repair, larger specimens must be built using the parameters stated in Chapter 4. After completion, the builds should be analyzed for quality metrics (e.g., microstructure and porosity) prior to more robust mechanical testing methods (e.g., uniaxial tensile testing, fatigue life testing, etc.). After which, links between the quality metrics and mechanical testing results can be generated.
- The preheating technique used in the current study could be improved to preheat the substrate to a uniform temperature during deposition. One example is to preheat the substrate continuously during deposition by applying the heater

underneath the substrate. This was not possible in current experiments because of sensor interference.

References

- [1] D. Gu, *Laser Additive Manufacturing of High-Performance Materials*. Springer Science+Business Media, 2015.
- [2] B. Mueller, *Additive Manufacturing Technologies*, vol. 32, no. 2. 2012.
- [3] I. Gibson, D. W. D. W. Rosen, and B. Stucker, *Additive Manufacturing Technologies: Rapid Prototyping to Direct Digital Manufacturing*, vol. 54. Springer Science+Business Media, 2009.
- [4] J. C. Heigel, P. Michaleris, and T. a. Palmer, “In situ monitoring and characterization of distortion during laser cladding of Inconel® 625,” *J. Mater. Process. Technol.*, vol. 220, pp. 135–145, 2015.
- [5] B. E. Carroll, T. A. Palmer, and A. M. Beese, “Anisotropic tensile behavior of Ti–6Al–4V components fabricated with directed energy deposition additive manufacturing,” *Acta Mater.*, vol. 87, pp. 309–320, 2015.
- [6] R. Vilar, “Laser cladding,” *J. Laser Appl.*, vol. 11, no. 2, p. 64, 1999.
- [7] J. A. Slotwinski and E. J. Garboczi, “Metrology Needs for Metal Additive Manufacturing Powders,” *Jom*, vol. 67, no. 3, pp. 538–543, 2015.
- [8] Malvern Instruments Limited, “Malvern Morphologi G3-ID.” Worcestershire, UK.
- [9] A. Strondl, O. Lyckfeldt, H. Brodin, and U. Ackelid, “Characterization and Control of Powder Properties for Additive Manufacturing,” *Jom*, vol. 67, no. 3, pp. 549–554, 2015.
- [10] Freeman Technology, “Measuring and understanding the flow properties of powders with the FT4 Powder Rheometer,” p. —, 2012.
- [11] Ophir Photonics, “Beamwatch Datasheet.” .
- [12] Ophir Photonics, “NanoScan 2s Datasheet.” .
- [13] L. L. Parimi, G. Ravi, D. Clark, and M. M. Attallah, “Microstructural and texture development in direct laser fabricated IN718,” *Mater. Charact.*, vol. 89, pp. 102–111, 2014.
- [14] P. A. Kobryn, E. H. Moore, and S. L. Semiatin, “Effect of laser power and traverse speed on microstructure, porosity, and build height in laser-deposited Ti-6Al-4V,” *Scr. Mater.*, vol. 43, no. 4, pp. 299–305, 2000.

- [15] G. P. Dinda, a. K. Dasgupta, and J. Mazumder, "Texture control during laser deposition of nickel-based superalloy," *Scr. Mater.*, vol. 67, no. 5, pp. 503–506, 2012.
- [16] H. Qi, M. Azer, and A. Ritter, "Studies of Standard Heat Treatment Effects on Microstructure and Mechanical Properties of Laser Net Shape Manufactured INCONEL 718," *Metall. Mater. Trans. A*, vol. 40, no. 10, pp. 2410–2422, Aug. 2009.
- [17] R. Reed, *The Superalloys, Fundamentals and Applications*. Cambridge, UK: Cambridge University Press, 2006.
- [18] Special Metal, "INCONEL Alloy 625," 2013.
- [19] Special Metals, "INCONEL Alloy 718."
- [20] W. D. Callister and D. G. Rethwisch, *Materials Science and Engineering: An Introduction*, 8th ed. New York: John Wiley and Sons, Inc., 2010.
- [21] A. Thomas, M. El-Wahabi, J. M. Cabrera, and J. M. Prado, "High temperature deformation of Inconel 718," *J. Mater. Process. Technol. 11th Int. Conf. Met. Form. 2006*, 2006.
- [22] S. Ghosh, S. Yadav, and G. Das, "Study of standard heat treatment on mechanical properties of Inconel 718 using ball indentation technique," *Mater. Lett.*, vol. 62, no. 17–18, pp. 2619–2622, 2008.
- [23] ASTM International, "Standard Hardness Conversion Tables for Metals Relationship Among Brinell Hardness, Vickers Hardness, Rockwell Hardness, Superficial Hardness, Knoop Hardness, Scleroscope Hardness, and Leeb Hardness," 2012.
- [24] B. B. Geddes, H. Leon, Z. Huang, and X. Huang, *Superalloys - Alloying and Performance*. Materials Park, OH: ASM International, 2010.
- [25] S. Azadian, L. Y. Wei, and R. Warren, "Delta phase precipitation in Inconel 718," *Mater. Charact.*, vol. 53, pp. 7–16, 2004.
- [26] X. Zhao, J. Chen, X. Lin, and W. Huang, "Study on microstructure and mechanical properties of laser rapid forming Inconel 718," *Mater. Sci. Eng. A*, vol. 478, no. 1–2, pp. 119–124, Apr. 2008.
- [27] W. Tayon, R. Shenoy, M. Redding, K. Bird, and R. Hafley, "Correlation Between Microstructure and Mechanical Properties in an INCONEL 718 Deposit Produced Via Electron Beam Freeform Fabrication," *Journal of Manufacturing Science and Engineering*, vol. 136. 2014.

- [28] R. R. Dehoff, M. M. Kirka, F. a. List III, K. a. Unocic, and W. J. Sames, "Crystallographic texture engineering through novel melt strategies via electron beam melting: Inconel 718," *Mater. Sci. Technol.*, vol. 000, no. 000, p. 1743284714Y.000, Oct. 2014.
- [29] Q. Jia and D. Gu, "Selective laser melting additive manufacturing of Inconel 718 superalloy parts: Densification, microstructure and properties," *J. Alloys Compd.*, vol. 585, pp. 713–721, 2014.
- [30] P. L. Blackwell, "The mechanical and microstructural characteristics of laser-deposited IN718," *J. Mater. Process. Technol.*, vol. 170, no. 1–2, pp. 240–246, Dec. 2005.
- [31] C. Zhong, A. Gasser, J. Kittel, J. Fu, Y. Ding, and R. Poprawe, "Microstructures and tensile properties of Inconel 718 formed by high deposition-rate laser metal deposition," *J. Laser Appl.*, vol. 28, no. 2, 2016.
- [32] G. Lütjering and J. C. Williams, *Titanium*, 2nd ed. Berlin Heidelberg: Springer-Verlag, 2007.
- [33] Donachie MJ, *Titanium - A Technical Guide*, 2nd ed. ASM International, 2000.
- [34] G. Lütjering, "Influence of processing on microstructure and mechanical properties of (α + β) titanium alloys," *Mater. Sci. Eng. A*, vol. 243, no. 1–2, pp. 32–45, 1998.
- [35] S. M. Kelly and S. L. Kampe, "Microstructural evolution in Laser-Deposited multilayer Ti6Al-4V build: Part I. Microstructural characterization," *Metall. Mater. Trans. A*, vol. 35, no. June, pp. 1861–1867, 2004.
- [36] S. M. Kelly, S. L. Kampe, and C. R. Crowe, "Microstructural study of laser formed Ti-6Al-4V," *Solid Free. Addit. Fabr.*, vol. 625, no. June, pp. 3–8, 2000.
- [37] X. Wu, J. Liang, J. Mei, C. Mitchell, P. S. Goodwin, and W. Voice, "Microstructures of laser-deposited Ti-6Al-4V," *Mater. Des.*, vol. 25, no. 2, pp. 137–144, 2004.
- [38] L. Bian, S. M. Thompson, and N. Shamsaei, "Mechanical Properties and Microstructural Features of Direct Laser-Deposited Ti-6Al-4V," *Jom*, vol. 67, no. 3, pp. 629–638, 2015.
- [39] I. Tabernero, a. Lamikiz, S. Martínez, E. Ukar, and J. Figueras, "Evaluation of the mechanical properties of Inconel 718 components built by laser cladding," *Int. J. Mach. Tools Manuf.*, vol. 51, no. 6, pp. 465–470, 2011.

- [40] M. Zhong and W. Liu, "Laser surface cladding: the state of the art and challenges," *Proc. Inst. Mech. Eng. Part C J. Mech. Eng. Sci.*, vol. 224, no. 5, pp. 1041–1060, 2010.
- [41] T. Vilaro, C. Colin, and J. D. Bartout, "As-fabricated and heat-treated microstructures of the Ti-6Al-4V alloy processed by selective laser melting," *Metall. Mater. Trans. A Phys. Metall. Mater. Sci.*, vol. 42, no. 10, pp. 3190–3199, 2011.
- [42] M. Ma, Z. Wang, and X. Zeng, "Effect of energy input on microstructural evolution of direct laser fabricated IN718 alloy," *Mater. Charact.*, vol. 106, pp. 420–427, 2015.
- [43] J. Lambarri, J. Leunda, V. García Navas, C. Soriano, and C. Sanz, "Microstructural and tensile characterization of Inconel 718 laser coatings for aeronautic components," *Opt. Lasers Eng.*, vol. 51, no. 7, pp. 813–821, 2013.
- [44] Q. li Zhang, J. hua Yao, and J. Mazumder, "Laser Direct Metal Deposition Technology and Microstructure and Composition Segregation of Inconel 718 Superalloy," *J. Iron Steel Res. Int.*, vol. 18, no. 4, pp. 73–78, 2011.
- [45] Y. C. Zhang, Z. G. Li, P. L. Nie, and Y. X. Wu, "Effect of ultrarapid cooling on microstructure of laser cladding IN718 coating," *Surf. Eng.*, vol. 29, no. 6, pp. 414–418, 2013.
- [46] Y. N. Zhang, X. Cao, P. Wanjara, and M. Medraj, "Fiber laser deposition of INCONEL 718 using powders," *Mater. Sci. Technol. Conf. Exhib. 2013, MS T 2013*, vol. 1, pp. 37–49, 2013.
- [47] Y. S. Lee and D. F. Farson, "Surface tension-powered build dimension control in laser additive manufacturing process," *Int. J. Adv. Manuf. Technol.*, 2015.
- [48] D. M. Goodarzi, J. Pekkarinen, and A. Salminen, "Effect of process parameters in laser cladding on substrate melted areas and the substrate melted shape," *J. Laser Appl.*, vol. 27, no. S2, p. S29201, 2015.
- [49] D. B. Hann, J. Iammi, and J. Folkes, "A simple methodology for predicting laser-weld properties from material and laser parameters," *J. Phys. D. Appl. Phys.*, vol. 44, no. 44, p. 445401, 2011.
- [50] J. J. Blecher, T. A. Palmer, and T. DebRoy, "Solidification Map of a Nickel-Base Alloy," *Metall. Mater. Trans. A*, vol. 45, no. 4, pp. 2142–2151, 2013.
- [51] K. C. Mills, *Recommended Values of Thermophysical Properties for Selected Commercial Alloys*. Woodhead Publishing, 2002.

- [52] D. J. Corbin, A. R. Nassar, E. W. Reutzel, A. M. Beese, and N. A. Kistler, "Effect of directed energy deposition processing parameters on laser deposited Inconel® 718: External morphology. Manuscript submitted for publication,," 2016.
- [53] Y. S. Lee, M. Nordin, S. S. Babu, and D. Farson, "Influence of Fluid Convection on Weld Pool Formation in Laser Cladding," *Weld. J.*, vol. 93, no. August, pp. 292–300, 2014.
- [54] W. Pitscheneder, T. DebRoy, K. Mundra, and R. Ebner, "Role of sulfur and processing variables on the temporal evolution of weld pool geometry during multikilowatt laser beam welding of steels," *Weld. J.*, vol. 75, no. March, p. 71s–80s, 1996.
- [55] a. Arora, G. G. Roy, and T. DebRoy, "Unusual wavy weld pool boundary from dimensional analysis," *Scr. Mater.*, vol. 60, no. 2, pp. 68–71, 2009.
- [56] D. Tabor, *The Hardness of Metals*. Oxford: Clarendon Press, 1951.
- [57] J. F. Radavich, "The Physical Metallurgy of Cast and Wrought Alloy 718," in *Superalloy 718, metallurgy and applications*, 1989, pp. 229–240.
- [58] R. Vilar and a. Almeida, "Repair and manufacturing of single crystal Ni-based superalloys components by laser powder deposition—A review," *J. Laser Appl.*, vol. 17004, 2015.
- [59] X. Wu, "A review of laser fabrication of metallic engineering components and of materials," *Mater. Sci. Technol.*, vol. 23, no. 6, pp. 631–640, 2007.
- [60] E. Brandl, V. Michailov, B. Viehweger, and C. Leyens, "Deposition of Ti-6Al-4V using laser and wire, part I: Microstructural properties of single beads," *Surf. Coatings Technol.*, vol. 206, no. 6, pp. 1120–1129, 2011.
- [61] E. Brandl, V. Michailov, B. Viehweger, and C. Leyens, "Deposition of Ti-6Al-4V using laser and wire, part II: Hardness and dimensions of single beads," *Surf. Coatings Technol.*, vol. 206, no. 6, pp. 1130–1141, 2011.
- [62] Y. Sun and M. Hao, "Statistical analysis and optimization of process parameters in Ti6Al4V laser cladding using Nd:YAG laser," *Opt. Lasers Eng.*, vol. 50, no. 7, pp. 985–995, 2012.
- [63] M. Megahed, H.-W. Mindt, N. N'Dri, H. Duan, and O. Desmaison, *Metal additive-manufacturing process and residual stress modeling*, vol. 5, no. 1. Integrating Materials and Manufacturing Innovation, 2016.
- [64] S. Joshi, J. Hildebrand, A. S. Aloraier, and T. Rabczuk, "Characterization of material properties and heat source parameters in welding simulation of two

- overlapping beads on a substrate plate,” *Comput. Mater. Sci.*, vol. 69, pp. 559–565, 2013.
- [65] ISO, “ISO 11146-1 Test methods for laser beam widths, divergence angles and beam propagation,” 2005.
 - [66] ASTM International, “ASTM E407-07(2015)e1 Standard Practice for Microetching Metals and Alloys,” West Conshohocken, PA, 2015.
 - [67] A.-M. El-Batahgy, A.-F. Khourshid, and T. Sharef, “Effect of Laser Beam Welding Parameters on Microstructure and Properties of Duplex Stainless Steel,” *Mater. Sci. Appl.*, vol. 02, no. 10, pp. 1443–1451, 2011.
 - [68] M. Harooni, B. Carlson, R. Kovacevic, and D. Street, “Effect of process parameters on the weld quality in laser welding of AZ31B magnesium alloy in lap joint configuration,” pp. 509–519, 2012.
 - [69] S. Minhyo and N. Kazuhiro, “Weld bead formation by a 10 kW class high power fiber laser on 16 mm thickness carbon steel plate,” *Trans. JWRI*, vol. 39, no. 1, pp. 33–38, 2010.
 - [70] G. Buvanashakaran, N. Siva Shanmugam, K. Sankaranarayananasamy, and R. Sabarikanth, “A study of laser welding modes with varying beam energy levels,” *Proc. Inst. Mech. Eng. Part C J. Mech. Eng. Sci.*, vol. 223, no. 5, pp. 1141–1156, 2009.
 - [71] F. Caiazzo, V. Alfieri, G. Corrado, F. Cardaropoli, and V. Sergi, “Investigation and Optimization of Laser Welding of Ti-6Al-4 V Titanium Alloy Plates,” *J. Manuf. Sci. Eng.*, vol. 135, no. 6, p. 061012, 2013.
 - [72] B. Shanmugarajan, J. N. Chary, G. Padmanabham, B. Arivazhagan, S. K. Albert, and A. K. Bhaduri, “Studies on autogenous laser welding of type 304B4 borated stainless steel,” *Opt. Lasers Eng.*, vol. 51, no. 11, pp. 1272–1277, 2013.
 - [73] G. Casalino, A. Olabi, N. Cipriani, and A. Rotondo, “Investigation on the residual stress of AISI 4047 low alloy steel laser welded,” *Key Eng. Mater.*, vol. 344, pp. 715–722, 2007.
 - [74] H. R. Ogden and R. I. Jaffee, “The effects of carbon, oxygen and nitrogen on the mechanical properties of titanium and titanium alloys,” 1955.
 - [75] ASTM International, “ASTM E384-16 Standard Test Method for Microindentation Hardness of Materials,” West Conshohocken, PA, 2016.
 - [76] S. Zekovic, R. Dwivedi, and R. Kovacevic, “Numerical simulation and experimental investigation of gas-powder flow from radially symmetrical nozzles

- in laser-based direct metal deposition,” *Int. J. Mach. Tools Manuf.*, vol. 47, no. 1, pp. 112–123, 2007.
- [77] G. J. Marshall, W. J. Young, S. M. Thompson, N. Shamsaei, S. R. Daniewicz, and S. Shao, “Understanding the Microstructure Formation of Ti-6Al-4V During Direct Laser Deposition via In-Situ Thermal Monitoring,” *Jom*, vol. 68, no. 3, pp. 1–13, 2016.
 - [78] P. A. Kobryn and S. L. Semiatin, “The Laser Additive Manufacture of Ti-6Al-4V,” *Jom*, no. September, pp. 40–42, 2001.
 - [79] J. Alcisto, a. Enriquez, H. Garcia, S. Hinkson, T. Steelman, E. Silverman, P. Valdovino, H. Gigerenzer, J. Foyos, J. Ogren, J. Dorey, K. Karg, T. McDonald, and O. S. Es-Said, “Tensile properties and microstructures of laser-formed Ti-6Al-4V,” *J. Mater. Eng. Perform.*, vol. 20, no. 2, pp. 203–212, 2011.
 - [80] G. P. Dinda, L. Song, and J. Mazumder, “Fabrication of Ti-6Al-4V scaffolds by direct metal deposition,” *Metall. Mater. Trans. A Phys. Metall. Mater. Sci.*, vol. 39, no. 12, pp. 2914–2922, 2008.
 - [81] X. Wu, J. Liang, J. Mei, C. Mitchell, P. S. Goodwin, and W. Voice, “Microstructures of laser-deposited Ti-6Al-4V,” *Mater. Des.*, vol. 25, no. 2, pp. 137–144, 2004.
 - [82] B. Yao, X. L. Ma, F. Lin, and W. J. Ge, “Microstructure and mechanical properties of Ti-6Al-4V components fabricated by laser micro cladding deposition,” *Rare Met.*, vol. 34, pp. 445–451, 2015.
 - [83] S. Zhang, X. Lin, J. Chen, and W. Huang, “Heat-treated microstructure and mechanical properties of laser solid forming Ti-6Al-4V alloy,” *Rare Met.*, vol. 28, no. 6, pp. 537–544, 2009.
 - [84] H. Paydas, A. Mertens, R. Carrus, J. Lecomte-Beckers, and J. Tchoufang Tchuindjang, “Laser cladding as repair technology for Ti-6Al-4V alloy: Influence of building strategy on microstructure and hardness,” *Mater. Des.*, vol. 85, pp. 497–510, 2015.
 - [85] ASTM International, “ASTM B265-15 Standard Specification for Titanium and Titanium Alloy Strip, Sheet, and Plate,” West Conshohocken, PA, 2015.
 - [86] P. . Kobryn and S. . Semiatin, “Microstructure and texture evolution during solidification processing of Ti-6Al-4V,” *J. Mater. Process. Technol.*, vol. 135, no. 2–3, pp. 330–339, 2003.
 - [87] N. A. Kistler, A. R. Nassar, E. W. Reutzel, D. J. Corbin, and A. M. Beese, “Effect of Directed Energy Deposition Processing Parameters on Laser Deposited Inconel

718: Microstructure, Fusion Zone Morphology, and Hardness. Manuscript submitted for publication,” *J. Laser Appl.*, 2016.

- [88] H. Zhao, G. Zhang, Z. Yin, and L. Wu, “A 3D dynamic analysis of thermal behavior during single-pass multi-layer weld-based rapid prototyping,” *J. Mater. Process. Technol.*, vol. 211, no. 3, pp. 488–495, 2011.
- [89] A. R. Nassar, J. S. Keist, E. W. Reutzel, and T. J. Spurgeon, “Intra-layer closed-loop control of build plan during directed energy additive manufacturing of Ti-6Al-4V,” *Addit. Manuf.*, vol. 6, pp. 39–52, 2015.